
Electronic Thesis and Dissertation Repository

12-11-2018 2:00 PM

Retrospective Motion Correction in Magnetic Resonance Imaging of the Brain

Patricia Johnson
The University of Western Ontario

Supervisor
Drangova, Maria
The University of Western Ontario

Graduate Program in Medical Biophysics
A thesis submitted in partial fulfillment of the requirements for the degree in Doctor of Philosophy
© Patricia Johnson 2018

Follow this and additional works at: <https://ir.lib.uwo.ca/etd>



Part of the [Analytical, Diagnostic and Therapeutic Techniques and Equipment Commons](#)

Recommended Citation

Johnson, Patricia, "Retrospective Motion Correction in Magnetic Resonance Imaging of the Brain" (2018).
Electronic Thesis and Dissertation Repository. 5863.
<https://ir.lib.uwo.ca/etd/5863>

This Dissertation/Thesis is brought to you for free and open access by Scholarship@Western. It has been accepted for inclusion in Electronic Thesis and Dissertation Repository by an authorized administrator of Scholarship@Western. For more information, please contact wlsadmin@uwo.ca.

Abstract

Magnetic Resonance Imaging (MRI) is a tremendously useful diagnostic imaging modality that provides outstanding soft tissue contrast. However, subject motion is a significant unsolved problem; motion during image acquisition can cause blurring and distortions in the image, limiting its diagnostic utility. Current techniques for addressing head motion include optical tracking which can be impractical in clinical settings due to challenges associated with camera cross-calibration and marker fixation. Another category of techniques is MRI navigators, which use specially acquired MRI data to track the motion of the head.

This thesis presents two techniques for motion correction in MRI: the first is spherical navigator echoes (SNAVs), which are rapidly acquired k-space navigators. The second is a deep convolutional neural network trained to predict an artefact-free image from motion-corrupted data.

Prior to this thesis, SNAVs had been demonstrated for motion measurement but not motion correction, and they required the acquisition of a 26s baseline scan during which the subject could not move. In this work, a novel baseline approach is developed where the acquisition is reduced to 2.6s. Spherical navigators were interleaved into a spoiled gradient echo sequence (SPGR) on a stand-alone MRI system and a turbo-FLASH sequence (tfl) on a hybrid PET/MRI system to enable motion measurement throughout image acquisition. The SNAV motion measurements were then used to retrospectively correct the image data.

While MRI navigator methods, particularly SNAVs that can be acquired very rapidly, are useful for motion correction, they do require pulse sequence modifications. A deep learning technique may be a more general solution. In this thesis, a conditional generative adversarial network (cGAN) is trained to perform motion correction on

image data with simulated motion artefacts. We simulate motion in previously acquired brain images and use the image pairs (corrupted + original) to train the cGAN.

MR image data was qualitatively and quantitatively improved following correction using the SNAV motion estimates. This was also true for the simultaneously acquired MR and PET data on the hybrid system. Motion corrected images were more similar than the uncorrected to the no-motion reference images. The deep learning approach was also successful for motion correction. The trained cGAN was evaluated on 5 subjects; and artefact suppression was observed in all images.

Keywords

Magnetic resonance imaging, Positron emission tomography, Motion correction, Navigator echoes, Deep learning

Co-Authorship Statement

This thesis is presented in an integrated article format, the Chapters of which are based on the following publications that are either published or under review:

Chapter 2: PM. Johnson, J. Liu, T. Wade, MA. Tavallaei, M. Drangova. “Retrospective 3D motion correction using spherical navigator echoes.” *Magnetic Resonance Imaging*. 2016 Nov; 34(9):1274-1282.

My contributions to this work included developing software for processing SNAV baseline data and retrospective motion correction. I was also responsible for all MRI scanning and data collection. Dr. Trevor Wade assisted with implementing the navigated pulse sequence. Dr. Junmin Liu is credited with the original idea for this project. His prior work with SNAVs served as a foundation for the work in this manuscript. Dr. Maria Drangova provided assistance with experiment design and manuscript preparation.

Chapter 3: PM. Johnson, R. Taylor, T. Whelan, JD. Thiessen, U. Anazodo, M. Drangova. “Rigid-body motion correction in hybrid PET/MRI using spherical navigator echoes.” Submitted to *Physics in Medicine and Biology*, 2018.

My contributions to this work include redesigning the SNAVs for the new platform, developing the software for retrospective correction of the MRI and PET data, as well as experiment design. Dr. Reggie Taylor and Tim Whelan assisted with development of the navigated pulse sequence. Dr. Udunna Anazodo provided valuable guidance and assistance in conducting the experiments. Udunna was also responsible for phantom preparation. Dr. Maria Drangova provided assistance with experiment design and manuscript preparation.

Chapter 4: PM. Johnson, M. Drangova. “Conditional generative adversarial network for three-dimensional rigid-body motion correction in MRI” submitted to Magnetic Resonance in Medicine, 2018.

My contributions to this work include defining the research questions and designing and developing the deep learning architecture. I developed all of the software for this project and conducted all experiments. Maria Drangova provided assistance with manuscript preparation.

All of the above work was performed under the guidance and supervision of Dr. Maria Drangova.

Acknowledgments

First and foremost, I would like to thank Dr. Maria Drangova. The work presented in this thesis would not have been possible without her mentorship and support. Maria provided me with guidance and direction, and the freedom to explore new ideas. Her mentorship has helped me grow as a scientist.

I would like to thank Dr. Junmin Liu for all of his advice and support. Junmin's PhD work served as the foundation for mine, and I am grateful that I was able to take over the project. I would also like to thank Dr. Trevor Wade and Dr. Reggie Taylor for their assistance with pulse sequence development, and for all of their teaching along the way.

I would also like to thank Dr. Charles McKenzie, Dr. Blaine Chronik, Dr. Terry Peters, and Dr. Rob Bartha for teaching me MRI physics. My sincere gratitude goes to Dr. Udunna Anazodo for her substantial contribution to the PET/MRI work presented in this thesis, and her eagerness to help me learn. I am grateful to all members of the Drangova lab as well as the other staff and students in Robarts Imaging who provided a warm and exciting environment that made Robarts home for the past 5 years.

Many sources of funding supported this work, including the Natural Sciences and Engineering Research Council (NSERC), the Ontario Graduate Scholarship, and the Western Graduate Research Scholarship. I would also like to acknowledge the technical support provided by Dr. Gerald Moran and Dr. David Faul from Siemens Healthcare. I would like to thank Compute Canada for access to computing resources.

My greatest appreciation goes to my parents and sister, who have always provided me with love and encouragement. Their continuous support and positive example have motivated me to work hard and confront new challenges.

Table of Contents

Abstract.....	i
Keywords.....	ii
Co-Authorship Statement	iii
Acknowledgments	v
Table of Contents.....	vi
List of Tables	xi
List of Figures.....	xii
List of Abbreviations	xviii
1 Introduction.....	1
1.1 Motion in magnetic resonance imaging.....	1
1.1.1 Subject motion in brain MRI	1
1.1.2 K space	2
1.1.3 Motion in k space	4
1.2 MRI motion measurement: current state of the art.....	5
1.2.1 MRI navigators	6
1.2.2 Optical tracking	7
1.2.3 Active markers.....	8
1.3 Motion correction: retrospective vs. prospective	8
1.4 Spherical Navigator Echoes.....	10
1.4.1 Early development.....	10
1.4.2 preRot-SNAV	13
1.5 Motion Correction in Hybrid PET/MRI	14

1.5.1	Positron Emission Tomography	14
1.5.2	Hybrid PET/MRI	14
1.5.3	Motion correction in Hybrid PET/MRI	15
1.6	Deep learning image-to-image translation	15
1.6.1	Neural networks.....	16
1.6.2	Deep learning.....	16
1.6.3	Deep convolutional neural networks	18
1.6.4	DCNN: classifier	18
1.6.5	DCNN: encoder-decoder	19
1.6.6	Conditional generative adversarial networks	20
1.7	Thesis outline.....	22
1.8	References	23
2	Retrospective 3D motion correction in MRI using SNAVs	28
2.1	Introduction	28
2.2	Methods	29
2.2.1	PreRot-SNAV overview	30
2.2.2	Hybrid baseline strategy	30
2.2.3	SNAV trajectory and acquisition.....	32
2.2.4	In vitro accuracy evaluation	32
2.2.5	Navigated pulse sequence.....	33
2.2.6	In vivo motion experiments.....	34
2.2.7	Analysis and retrospective correction.....	34
2.2.8	Partial SNAV evaluation in vivo	35

2.3	Results	36
2.3.1	Static phantom rotation and translation measurements	36
2.3.2	Dynamic compound motion measurements	37
2.3.3	Effect of SNAVs on SPGR images	39
2.3.4	Retrospective motion correction.....	39
2.3.5	Partial SNAV evaluation	42
2.4	Discussion.....	44
2.5	Conclusions	47
2.6	References	48
3	Rigid-body motion correction in hybrid PET/MRI using spherical navigator echoes .	51
3.1	Introduction	51
3.2	Methods	53
3.2.1	SNAV motion correction.....	53
3.2.2	Navigated pulse sequence implementation.....	54
3.2.3	Motion experiments.....	55
3.2.4	Motion measurement and correction	56
3.2.5	Quantitative evaluation of image quality.....	57
3.3	Results	60
3.3.1	tfl-SNAV pulse sequence	60
3.3.2	Motion measurement and correction	60
3.3.3	Quantitative evaluation of motion correction.....	63
3.4	Discussion.....	66
3.5	Conclusion	68

3.6	References	69
4	Conditional generative adversarial network for three-dimensional rigid-body motion correction in MRI	72
4.1	Introduction	72
4.2	Methods	74
4.2.1	Data preparation	74
4.2.2	Motion simulation	75
4.2.3	Network architecture	77
4.2.4	Network training	80
4.2.5	Evaluation of network performance	80
4.3	Results	81
4.3.1	Motion correction: image results	81
4.3.2	Quantitative evaluation	81
4.4	Discussion	85
4.5	Conclusion	87
4.6	References	88
5	Conclusions and Future Directions	92
5.1	Contributions	92
5.1.1	SNAVs	92
5.1.2	MoCo-cGan	92
5.2	Conclusions	93
5.3	Limitations	94
5.3.1	SNAVs	94
5.3.2	MoCo-cGAN	95

5.4 SNAVs: Suggestions for future work.....	95
5.4.1 SNAVs for a variety of pulse sequences and applications	96
5.4.2 Implement SNAVs for prospective motion correction.....	97
5.4.3 Evaluate SNAVs in a patient population.....	98
5.4.4 Cardiac fat SNAVs	98
5.5 MoCo-cGAN: suggestions for future work.....	98
5.5.1 Fine-tune MoCo-cGAN for images with real motion.	98
5.5.2 Deep learning-based motion corrected MRI reconstruction.....	99
5.5.3 Deep learning motion correction with unpaired image to image translation.	99
5.6 References	102
APPENDIX.....	103
Appendix A.....	103
Permission for reproduction of scientific articles	103
Appendix A.1: Reprint Permission: Chapter 1, Figure 1-4	104
Appendix A.2: Reprint Permission: Chapter 1, Figure 1-5	106
Appendix A.3: Reprint Permission: Chapter 1, Figure 1-9	108
Appendix A.4: Reprint Permission: Chapter 2	110
Appendix B.....	111
Ethics approval notices	111
Appendix C- Curriculum Vitae.....	114

List of Tables

Table 1. Description of the parameters used to generate the random motion profiles.	
.....	77

List of Figures

Figure 1-1 Illustration of 2D Cartesian sampling. Each line of k space is acquired sequentially.....	3
Figure 1-2 Example k space and corresponding 2D brain image.....	4
Figure 1-3 An example k space and corresponding image with motion artefacts. The k-space data collection is corrupted by rotation and translation of the head. Applying the IFFT to this k-space data results in an image with motion artefacts.	5
Figure 1-4 Rotations during k-space acquisition lead to gaps in k space (a) which can be difficult to recover retrospectively. Prospective correction on the other hand, maintains uniform sampling of k space. Figure adapted from Maclaren et al. ³¹	9
Figure 1-5 Welch <i>et al.</i> illustrated the magnitude profile of an SNAV with the sampling pattern shown in (a). The SNAVs in (b) and (c) have a relative rotation of 12°. The poles remain un-sampled due to slew rate limits of the gradient hardware. Figure from Welch <i>et al.</i> , ¹¹ reproduced with permission.....	10
Figure 1-6 The X gradient waveform (a) is shown along with the x gradient slew rate (c). The Z gradient waveform is shown in (b) and the k-space trajectory for a 0.6 cm ⁻¹ SNAV is shown in (d). Figure from Petrie <i>et al.</i> , ¹⁰ reproduced with permission.	12
Figure 1-7 A single layer perceptron (SLP) has one hidden layer, an SLP binary classifier has a single output node which classifies the set of inputs into one of two classes.	16
Figure 1-8 The simple neural network on the left has a single hidden layer (feature vector). The deep neural network has many feature vectors, which increases the model capacity and allows the model to learn more abstract and complex features from the input data. Each orange and blue node is the result of a non-linear activation function applied to the dot product of the feature vector in the previous layer and a learned weight vector.....	17

Figure 1-9 The VGG-net classifier consists of 16 trainable layers. These include convolutional layers (Conv), and fully connected (FC) layers. Max-pooling (Pool) layers are used for dimensionality reduction.19

Figure 1-10 Encoder decoder network trained with T1/T2-FLAIR image pairs synthesizes a T2-FLAIR image from a T1-weighted image.⁵³ Each layer includes convolution and a sigmoid activation function. Max- pooling is used in the encoder portion of the network, while up-sampling is used in the decoder portion of the network. Figure from Sevetlidis et. al.,⁵³ reproduced with permission from Springer Nature.....20

Figure 1-11 In this pix2pix illustration, the generator input is a black and white image and the target is the corresponding colour image. The generator predicted image (fake) along with its corresponding input, forms an image pair that is used to train the discriminator. Both fake and real image pairs are used to train the discriminator. The discriminator is trained to distinguish between target (real) images and fake images, while the generator is trained to predict images that are quantitatively similar to the target and will fool the discriminator. Figure adapted from Cho 2017.⁵⁸21

Figure 2-1 Rotation (a-c) and translation (d-f) measurements of three trial repositions of the skull phantom. Results obtained using the full 512-template baseline dataset is plotted with those obtained using the 170- and 82-hybrid baseline datasets. The error bars, representing standard deviation of 32 SNAV measurements, are smaller than the symbols in most cases (maximum 0.2°, 0.6 mm).37

Figure 2-2 Rotation (a) and translation (b) results for the compound motion experiments using 82-hybrid baselines, demonstrate the ability to follow compound motion over time (12 of the 26 acquired seconds are shown). Rotation estimates at the stationary reference position were $\theta_x = -1.5^\circ$, $\theta_y = 3.5^\circ$, $\theta_z = -11.0^\circ$. The standard deviation of the rotation measurements is lower than 0.2° and the variation is attributed to the large translation component. The motion stage was programmed to move the rotated phantom sinusoidally with a period of 3 s and amplitude of 10 mm.38

Figure 2-3 Axial and sagittal slice from the 3D image acquired with the product SPGR sequence (a) and the SPGR-SNAV sequence (b). The SPGR-SNAV image was retrospectively corrected (c) using measured SNAV rotation (d) and translation (e). The oscillations in z translation correspond to the respiratory rate of the subject. All three images have the same image entropy.40

Figure 2-4 Axial and sagittal slices acquired with a single-channel head coil: (a) no motion reference image; (b) uncorrected image acquired with intended rotation; (c) motion corrected image. The measured rotations and translations, obtained using the 82-hybrid baseline, are shown in (d) and (e).41

Figure 2-5 Axial and sagittal slices from the 3D reference image acquired with an 8-channel head coil (a) uncorrected image acquired with intended rotation (b) and motion corrected image (c). The measured rotations and translations are shown in (d) and (e).42

Figure 2-6 Effect of reducing the number of turns of the SNAV. Shown are axial and sagittal slices from a 3D reference image (a), uncorrected motion image (b), and motion-corrected images with 22 (full), 18, 14, 10, 6 and 2 SNAV helical turns in (c-h), respectively.43

Figure 2-7 Image entropy of each corrected image normalized by the entropy of the associated reference image plotted vs. number of helical turns used for SNAV motion measurements. The horizontal lines indicate the normalized image entropy of the uncorrected images.44

Figure 3-1 An example SNAV magnitude profile – displayed in arbitrary units – is illustrated in (a). The SNAV has a total of 1600 data points sampled on a spherical shell with radius 0.4 cm^{-1} . A simplified timing diagram illustrates the turbo-FLASH (tfl) and tfl-SNAV pulse sequences (b). A single TR for each sequence is shown. Both sequences have a 180° inversion pulse followed by a readout train with 80 echoes. The SNAV is inserted

in the phase encode loop, prior to the inversion pulse and during the dead time of the original tfl sequence, which is then followed by the tfl sequence readout train.....55

Figure 3-2 Flow chart of the SNAV motion correction technique from the acquisition of tfl-snav to the motion correction of the PET and MR image data.....59

Figure 3-3 Axial slices of the product tfl (a), tfl-SNAV (b) and motion corrected tfl (c). The motion profile measured during the tfl-SNAV sequence (d) was used for the motion correction.61

Figure 3-4 Rotations and translations measured by the SNAVs in trials 1 (a), 2 (b) and 3 (c). The vertical dotted lines indicate the temporal bins used for RTA reconstruction. The vertical blue line indicates the center line of k space.62

Figure 3-5 SNAV motion correction results. A single slice of the motion-corrupted, corrected and reference PET and MR images are shown for each trial. The difference images are shown in the fourth and fifth columns. The colour bars show the range of pixel intensities in the difference images (original images were scaled from 0 to 1). Motion correction was achieved in trial 1 (a), trial 2 (b) and trial 3 (c). The white lines in the reference image indicate the location of the measured line profiles displayed in Figure 3-6.64

Figure 3-6 Line profiles calculated along a horizontal line (left-right) for trials 1 (a &b), 2 (c&d) and 3 (e&f). The location of each line is shown in Figure 3-5 as white dotted lines; the line profile was measured in the same plane as the displayed images.65

Figure 3-7 Peak signal to noise ratio (top) and structural similarity index (bottom) calculated for PET and MR images from trials 1, 2 and 3.66

Figure 4-1 Illustration of pre-processing steps for a single subject. The magnitude and phase images are combined to form a complex image, which is then down-sampled to 192x156x128. The 3D Fourier transform is applied to create k space. Five different motion

profiles are applied to this k space to generate 5 motion-corrupted k-space volumes. The motion-corrupted k-space volumes are then transformed back to the image domain to yield motion corrupted images. Each motion-corrupted image is broken up into 8 patches (192x156x8) for training.75

Figure 4-2 The input to the generator network (a), which is based on U-Net, is a batch of 192x160x8 brain image patches. Each set of three grey boxes represents a hidden layer with a large number of 3D feature vectors (the actual number for each layer is indicated below the boxes). In the generator diagram, the red arrows represent 3D convolution with 3x3x3 filters, a rectified linear unit activation function and batch normalization; the back arrow is the same with added dropout; the blue arrows represent the 3D maxpooling operation, while the purple arrows represent the convolution + upsampling operations. The arrows with dotted lines represent concatenation operations. The dimensions of the feature vectors in each network level are listed on the left. The input to the discriminator (b) is a batch of image pairs. In (b), the blue arrow represents 3D convolution with 4x4x4 filters, and a Leaky ReLU activation function; the red arrows are the same with the addition of batch normalization. The feature vectors are flattened (black arrow) to a 1D vector, which is then fully connected to the output layer – a decision as to whether the input image pairs contain a target or generated image.79

Figure 4-3 Representative MoCo-cGAN motion correction results. From left to right, a single axial slice of the motion-corrupted, motion-corrected and reference images are shown for subjects 1(a), 2(b) and 3(c). The difference images are shown in the fourth (reference – motion) and fifth (reference – corrected) columns. The colour bars show the range of pixel intensities in the difference images (original images were scaled from 0 to 1). The corresponding motion profiles are plotted in (d) through (f). The arrow in the reference image for subject 2, points to a ringing motion artefact that is not present in the corrected image, suggesting that the MoCo-cGAN network corrected a real motion artefact in addition to the simulated motion artefacts.82

Figure 4-4 Sagittal and coronal views of the volumes shown in Figure 4-3. From left to right, a single sagittal (top) and coronal slice (bottom) of the motion-corrupted, motion-corrected and reference images are shown for subjects 1(a), 2(b) and 3(c).83

Figure 4-5 Mean absolute error (a), peak signal to noise ratio (b), and structural similarity index (c) calculated for all 25 image volumes. For clarity, the 25 volumes were sorted from lowest to highest mean absolute error of the motion-corrupted image.84

Figure 5-1 Illustration of cycle-GAN. A motion-corrupted image is transformed by generator G to an artefact free image. The output of G becomes the input to a discriminator which classifies the image as a real image or a generator image. An artefact free image is transformed by generator F to a motion-corrupted image and becomes the input to a second discriminator. Training generator G involves maximizing the discriminator error and minimizing the cycle-consistency loss.101

List of Abbreviations

1D	one dimensional
2D	two dimensional
3D	three dimensional
cGAN	conditional generative adversarial network
CIFAR	Canadian Institute for Advanced Research
CT	computed tomography
DCNN	deep convolutional neural network
DNN	deep neural network
FC	fully connected
FDG	fluorodeoxyglucose
FFT	fast Fourier transform
FLASH	fast low angle shot
FMRI	functional magnetic resonance imaging
GAN	generative adversarial network
GPU	graphical processing unit
IFFT	inverse fast Fourier transform
MAE	mean absolute error

MAF	multiple acquisition frames
MoCo-cGAN	motion correction generative adversarial network
MRI	magnetic resonance imaging
MSK	musculoskeletal
NAV	navigator
NuFFT	Non-uniform fast Fourier transform
PACE	prospective acquisition correction
PET	positron emission tomography
PET/MRI	hybrid positron emission tomography and magnetic resonance imaging
preRot	pre-rotated
PROMO	prospective motion correction
PSNR	peak signal to noise ratio
ReLU	rectified linear unit
RF	radiofrequency
SNAV	spherical navigator echo
SPGR	spoiled gradient recalled echo
SSIM	structural similarity index
T2-FLAIR	T2 weighted fluid attenuated inversion recovery

TE	echo time
TFL	turbo-FLASH
TR	repetition time
VSD	variable sampling density
VNAV	volume navigator

1 Introduction

Magnetic resonance imaging (MRI) is a tremendously useful clinical tool for diagnostic imaging. Its superior soft tissue contrast makes it a valuable imaging method for many diagnostic and research applications. However, subject motion is a significant unsolved problem; motion during image acquisition can cause blurring and distortions in the image. In this thesis, the development of novel techniques for motion correction in MRI, specifically spherical navigators and deep learning, are discussed.

1.1 Motion in magnetic resonance imaging

Magnetic resonance imaging technology has advanced considerably since its first use for clinical imaging in the 1980's; however, patient motion remains an unsolved problem. As MRI hardware and software development allow us to push the boundaries on image resolution and image quality, patient motion becomes a limiting factor in many applications. If a patient moves during the scan, it may cause blurring and artefacts in the image, which significantly degrades the diagnostic quality of the image. MRI is highly sensitive to patient motion, due in part, to long acquisition times.

Motion in MRI can broadly be classified into two categories: involuntary physiological motion such as breathing, and voluntary bulk motion such as the movement of the head or a limb. The focus of this thesis is motion correction in neuroimaging applications, and as such, the focus is on rigid-body motion of the head.

1.1.1 *Subject motion in brain MRI*

MRI exams can take from 10 mins to over an hour to complete, and it is challenging for many subjects to remain still throughout the scan. A study by Andre *et al.* found that approximately 20% of exams at their institution required that at least one sequence is repeated due to motion.¹ They estimated that these repeat scans cost \$115,000 per

year per scanner and resulted in delayed diagnosis for some patients. Motion is the most prevalent MRI artefact that results in non-diagnostic brain scans, especially in pediatric populations.² In current clinical practice, most young children are either sedated or anesthetized in order to have a successful imaging session. While head motion is observed across the entire population, it is an even bigger challenge for specific patient groups, including children, the elderly and people with various mental and neurodegenerative disorders.²

Motion is also a challenge in MRI research applications. MRI is often used to study the effects of disease modifying therapies as well as normal neurodevelopment in children. In these types of applications, motion can have a systematic effect, because the amount of motion in the scanner is often correlated with age and disease severity. It has been found specifically that motion reduces grey matter volume estimates³ and causes systematic errors in measurements of functional connectivity.^{4,5}

1.1.2 *K space*

The cause of motion artefacts in MRI is rooted in the nature of the raw data and its time consuming, sequential acquisition. With the application of spatial magnetic field gradients (G), the time varying signals detected from precessing magnetization follow predictable trajectories that evolve in two-dimensional (2D) or three-dimensional (3D) k space:

$$k_x = \frac{\gamma}{2\pi} \int_0^t G_x(t') dt' \quad (1.1)$$

$$k_y = \frac{\gamma}{2\pi} \int_0^t G_y(t') dt' \quad (1.2)$$

where k_x , and k_y are the 2Dk-space coordinates, γ is the Larmor precession frequency, and G_x , G_y are the applied magnetic field gradients along the x and y dimensions respectively. The gradients control the position in k space at a given time; MRI pulse sequences and acquisition strategies are designed such that k space is

sufficiently and efficiently sampled. A 2D cartesian k-space trajectory is illustrated in Figure 1-1.

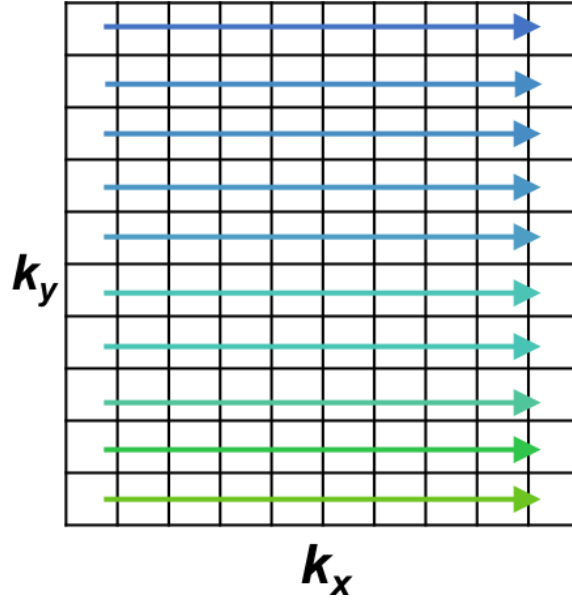


Figure 1-1 Illustration of 2D Cartesian sampling. Each line of k space is acquired sequentially.

Acquisition of k-space data is inherently slow due to sampling requirements, and the fundamental magnetic properties of biological tissue (T1). Motion during the acquisition of k space creates inconsistencies in k-space data which lead to artefacts in the reconstructed image. This will be discussed in more detail in the next section.

The discrete inverse fast Fourier transform (IFFT) is applied to k space in order to reconstruct the image. The discrete 2D IFFT for an M by N dimensional image is given by:

$$S(x, y) = \sum_{k_x=0}^{M-1} \sum_{k_y=0}^{N-1} d_{k_x k_y} e^{\frac{2\pi i k_x x}{M}} e^{\frac{2\pi i k_y y}{N}} \quad (1.3)$$

where $S(x,y)$ is the 2D image, $d_{k_x k_y}$ are the complex values of the input rectilinear k space with dimensions M by N. k_x and k_y are the k-space coordinates and x and y are the co-ordinates in image space. This operation can be performed in any number of dimensions. The 2D and 3D Fourier transforms are both common for MRI applications. An example 2D k space and its corresponding image are shown in Figure 1-2.

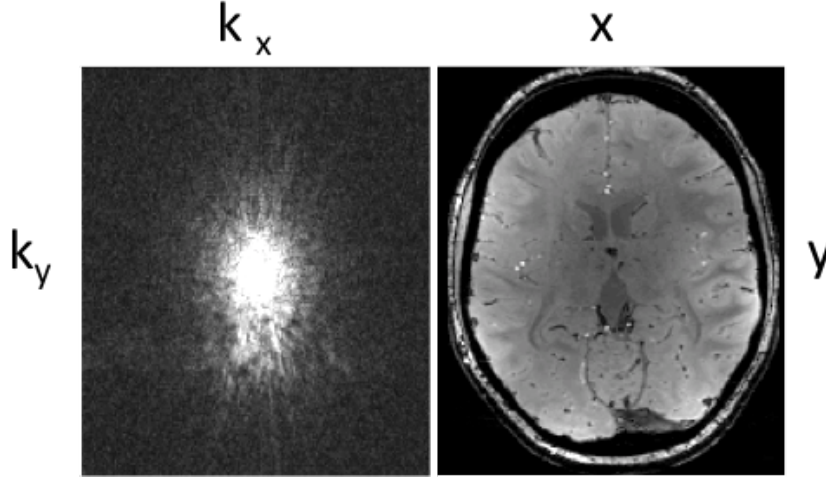


Figure 1-2 Example k space and corresponding 2D brain image.

1.1.3 Motion in k space

The effects of rigid-body motion in k space can be described in terms of two well known Fourier properties. The Fourier shift theorem tells us that a physical translation in image space (e.g. head translation) yields a linear phase ramp in k space:

$$S(x + a, y + b) = \sum_{k_x=0}^{M-1} \sum_{k_y=0}^{N-1} d_{k_x k_y} e^{\frac{2\pi i k_x (x+a)}{M}} e^{\frac{2\pi i k_y (y+b)}{N}} \quad (1.4)$$

where, a and b are translations in the x and y dimensions respectively. We also know that a rotation in image space causes an identical rotation in k space. Therefore, if a subject translates and rotates their head in the scanner, the result will be phase ramps, and rotations in the raw k-space data; it is these inconsistencies that cause motion artefacts (i.e. some k-space lines are rotated and phase shifted relative to others). When

the IFFT is applied to this translation- and rotation-corrupted k-space data, the result is an image with artefacts as illustrated in Figure 1-3.

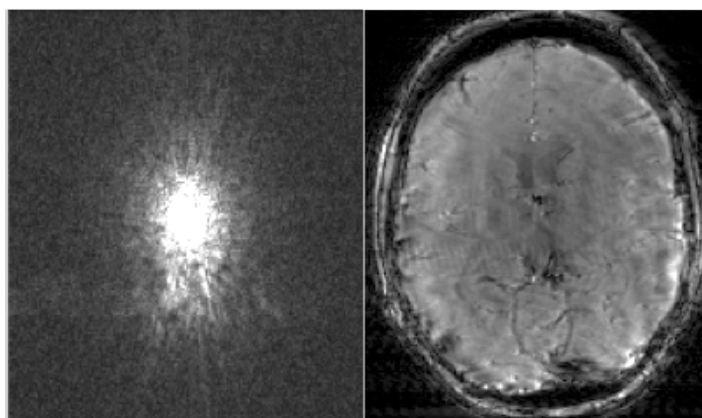


Figure 1-3 An example k space and corresponding image with motion artefacts. The k-space data collection is corrupted by rotation and translation of the head. Applying the IFFT to this k-space data results in an image with motion artefacts.

1.2 *MRI motion measurement: current state of the art*

In order to correct for motion in MRI, the motion must be measured throughout the image acquisition. Over the past three decades there have been many techniques developed for motion measurement in brain MRI. The first developments were a class of techniques called MRI navigators, followed later by optical tracking, and finally active markers. These methods differ in how motion is measured throughout an image acquisition but are similar in the way that motion is corrected. This section focuses on motion measurement, while motion correction will be discussed in section 1.3. The three main classes of techniques for rigid-body motion measurement, which are all still active areas of research, will be briefly described in this section. Each of these methods has unique advantages and disadvantages, which make them suitable for specific applications. These techniques contribute to a diverse toolbox of motion correction solutions for MR brain imaging.

1.2.1 *MRI navigators*

The term “MRI navigators” (NAVs) refers to the collection of techniques that use only MRI data – collected in addition to the data required for the image – for motion correction. This data can be either k space or image space data. Generally, a reference NAV, or set of reference NAVs, is acquired at the beginning of a scan. Measurement NAVs are interleaved in an image acquisition and are compared to the reference to calculate the relative position of the object.

The seminal work on MRI navigators was published in 1989.⁶ This technique involved one-dimensional (1D) NAVs that were interleaved in a spin-echo image sequence. The 1D navigators are Fourier transformed to create a projection in image space. The cross-correlation function was used to compare measurement NAVs with the reference NAV, in order to calculate the displacement. While this technique was only able to measure and correct for translation in one dimension, it set the stage for decades of continued development of MRI navigators.

After the seminal work by Ehman *et al.*, more advanced k-space navigator techniques were developed. Orbital NAVs⁷ as well as octant NAVs,⁸ successfully measured and corrected for two-dimensional motion (i.e. in-plane translation and rotation), while later developments including cloverleaf⁹ and spherical NAVs,^{10,11} were able to measure full 3D rigid-body motion. Spherical Navigators will be discussed in more detail in section 1.4.

Navigator techniques have also been developed using MRI data in image space. The concept is very similar to k-space navigators, but the measurement is performed by comparing low-resolution images. A reference image is acquired at the beginning of the scan, then low-resolution images are acquired throughout the main image acquisition, and finally these images are registered to the reference image to determine

the relative motion. Prospective acquisition correction (PACE),¹² prospective motion correction (PROMO),¹³ and volume navigators (vNAVs)^{14,15} are all examples of image-space NAV methods. Image-space NAVs can also be fat images – collectively known as fat-NAVs – as was shown by Gallichan *et al.*¹⁶ and Engstrom *et al.*¹⁷ in 2015. While image NAVs have been very useful for measuring head motion, they take longer to acquire (on the order of 100s of ms) than k-space navigators (on the order of 10s of ms), which can limit implementation options and/or lengthen scan time.

1.2.2 *Optical tracking*

Optical tracking, sometimes called external tracking, involves measuring motion with an external camera system. Markers are fixed to the subject's head and the camera is used to measure the motion of the markers throughout the image acquisition. The earliest publication that used optical tracking for motion measurement was a study in 2005 that used the motion estimates to retrospectively co-register functional MRI (fMRI) image volumes.¹⁸ The first study to use this technology for intra-image motion correction was published in 2006; they demonstrated prospective motion correction in phantom and brain images acquired at 3T.¹⁹ Subsequent development of optical tracking focused on reducing cross-calibration errors,^{20,21} optimizing the markers,^{22,23} implementing the technique on a 7T system,^{24,25} as well as evaluating the technique for different applications such as magnetic resonance spectroscopy,²⁶ and arterial spin labeling.²⁷

Optical tracking has been very successful at motion correction for brain imaging in research settings, but there are several factors that limit its clinical feasibility. One of these limitations is the need for an expert to perform regular cross-calibration of the camera system to ensure that the reference frames of the camera and MRI scanner are aligned. Another challenge is achieving rigid fixation of the markers to the head. For accurate motion correction, individually manufactured mouthpieces are typically

used,²⁵ which is not practical for clinical imaging. Additionally, achieving adequate line-of-sight between the camera system and the markers is not trivial due to scanner geometry and the requirement for MRI compatibility.

1.2.3 *Active markers*

Active markers were introduced for MRI motion correction by Ooi *et al.* in 2009²⁸ and have since been used for echo-planar imaging specifically²⁹ as well as for motion correction in hybrid positron emission tomography and MRI (PET/MRI).³⁰ This technique utilizes MRI visible spheres, which are fixed in tiny receive coils attached to a headband worn by the patient. Short sequences of pulses are inserted in the imaging sequence in order to track the motion of the markers throughout the image acquisition. These MRI based tracking elements are shorter than the MRI navigators discussed in Section 1.2.2. Unlike optical tracking, this technique does not require a camera or any cross-calibration, however the use of a headband and the requirement for the miniature receive coils to be connected to the scanner with wires makes effective rigid coupling of the markers even more challenging.

1.3 *Motion correction: retrospective vs. prospective*

Once the subject's head motion is known, the MR image data can be corrected either retrospectively or prospectively. Rigid-body motion causes rotations and phase shifts in k space; retrospective correction refers to the correction of these errors once the entire image has been acquired. With retrospective motion correction, the k-space lines are rotated, and phase shifted based on the measured motion. A limitation of this technique is the requirement for interpolation of the k-space data, which can lead to blurring. Additionally, large rotations cause large gaps in the k-space sampling and this data cannot easily be recovered retrospectively. This concept is illustrated in Figure 1-4 (adapted from Maclaren *et al.* 2013).³¹ Retrospective correction does have the

advantage that the original data will always be available, which is not the case for prospective correction.

Prospective motion correction is an approach where scan parameters are adjusted in real-time in order to essentially follow the object. After a motion measurement is performed, the gradients, as well as the transmit frequency and phase can be adjusted to move the image frame of reference to that of the repositioned object. This approach avoids sampling errors and therefore does not require any interpolation of image data. Using this approach means the original data will not be available which could be highly problematic in the event the prospective correction fails. Ultimately, prospective correction has the potential for better performance but having the unaltered raw data available may make retrospective correction a lower risk option for implementation in the clinic.

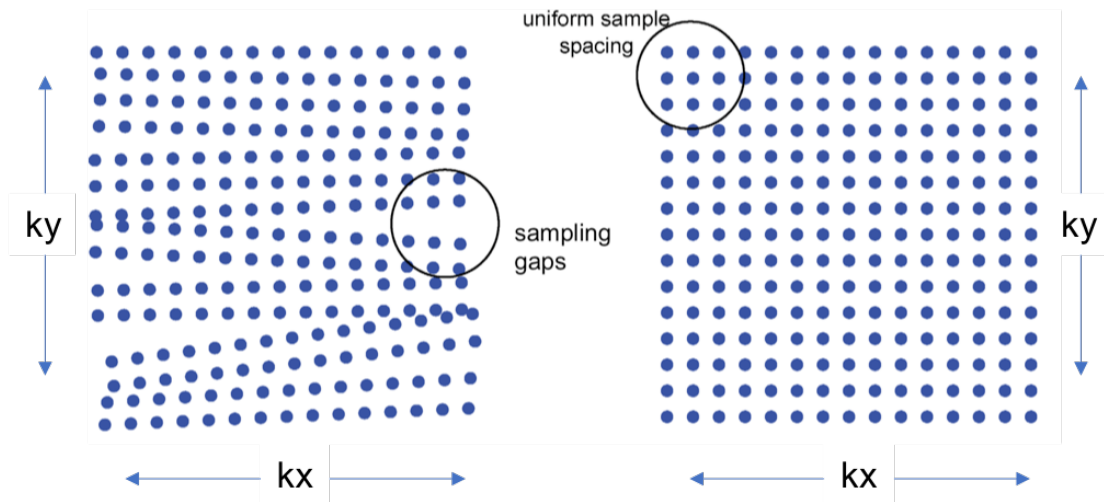


Figure 1-4 Rotations during k-space acquisition lead to gaps in k space (a) which can be difficult to recover retrospectively. Prospective correction on the other hand, maintains uniform sampling of k space. Figure adapted from Maclaren et al.³¹

1.4 Spherical Navigator Echoes

A Spherical Navigator Echo (SNAV) is a three-dimensional, k-space navigator that can measure rigid-body motion in all 6 degrees of freedom. The technique was first introduced for motion measurement in 2002 by Welch *et al.*¹¹, and there have been significant further developments since that time. This section will discuss the SNAV technique, and its development prior to the work of this thesis.

1.4.1 Early development

Welch *et al.* described a NAV that samples a spherical trajectory in k space. It is acquired in two excitations – one for each hemisphere – that spiral from the equator to the poles. Rotations of an object will cause an identical rotation of the data on the spherical shell; these rotations can be detected by simply registering the magnitude profiles before and after the rotation. Translations will add linear phase ramps to the data, which can be measured following rotation determination. A baseline SNAV is acquired at the beginning of the scan, to which subsequent SNAVs can be registered. An example magnitude profile is shown in Figure 1-5.

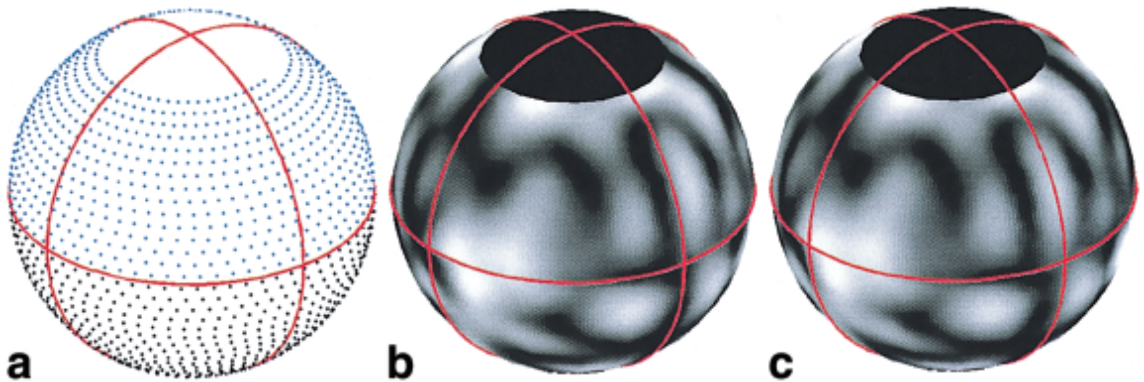


Figure 1-5 Welch *et al.* illustrated the magnitude profile of an SNAV with the sampling pattern shown in (a). The SNAVs in (b) and (c) have a relative rotation of 12° . The poles remain un-sampled due to slew rate limits of the gradient hardware. Figure from Welch *et al.*,¹¹ reproduced with permission

The relationship between a baseline SNAV signal and an SNAV signal acquired in a rotated coordinate system (k_x', k_y', k_z') with translation ($\Delta x, \Delta y, \Delta z$) is given by:

$$S'(k'_x, k'_y, k'_z) = S(k_x, k_y, k_z) e^{i2\pi(\Delta x k_x + \Delta y k_y + \Delta z k_z)} \quad (1.5)$$

The rotation is determined by minimizing the squared difference between the SNAV at the unknown position and the baseline SNAV. This is an iterative optimization procedure, which can take several seconds to perform. Once the rotation has been measured the translations can be measured by calculating the phase difference ($\Delta\phi$) between corresponding points. If there are N sample points on the sphere, this yields a system of N equations and three unknowns, where all N equations are of the form:

$$\Delta\phi = 2\pi[\Delta x k_x + \Delta y k_y + \Delta z k_z] \quad (1.6)$$

This proof of concept work demonstrated that SNAVs can measure rigid motion. A limitation of the technique is the lengthy iterative process for rotation determination. In order for the SNAVs to be used for prospective, or even timely retrospective correction, a much more rapid motion measurement technique is required. Additionally, the poles of the sphere were not sampled due to slew rate limits of the scanner.

Subsequent work focused on optimizing SNAVs for use in motion correction of brain images. Petrie *et al.* developed a variable sampling density (VSD) trajectory, which allowed sampling of the entire sphere without exceeding slew rate limits.¹⁰ The gradient waveforms and spherical trajectory of the VSD SNAV are shown in Figure 1-6. They also explored the trade-off associated with the SNAV radius (k_p); a lower k_p will have higher signal to noise ratio (SNR) but fewer magnitude features and higher k_p will have lower SNR but more magnitude features. This is an important consideration that will affect the accuracy of rotation estimates. They tested radii in the range of 0.4 - 1.8 cm^{-1} and suggested that the optimal radius is object dependent.

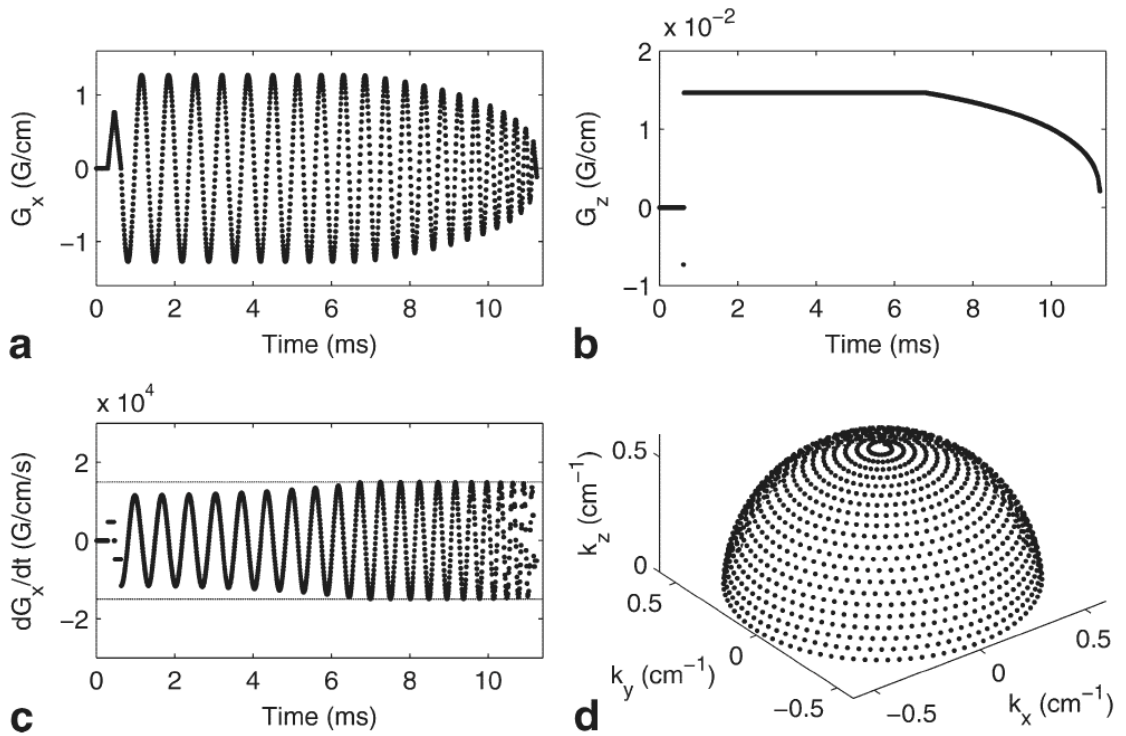


Figure 1-6 The X gradient waveform (a) is shown along with the x gradient slew rate (c). The Z gradient waveform is shown in (b) and the k-space trajectory for a 0.6 cm $^{-1}$ SNAV is shown in (d). Figure from Petrie *et al.*,¹⁰ reproduced with permission.

Later work by Liu *et al.* developed a phase unwrapping technique for SNAV translation measurements. Prior to this development the maximum translation that could be measured was $0.5/k_p$. In the case of $k_p = 0.4$ cm $^{-1}$, the maximum translation that can be measured before a phase wrap occurs is 1.25 cm. Liu *et al.* demonstrated that with the SNAV phase unwrapping method, translations up to 4 cm could be measured.³² In another study by Liu *et al.*, SNAVs were further developed for multi-channel receive coils.³³ They explored different options for combining the complex SNAV signal from multiple coils and determined that a simple complex sum resulted in the most accurate motion measurements.

1.4.2 *preRot-SNAV*

In 2011, Liu *et al.* developed the preRot SNAV method.³⁴ This technique drastically reduced the processing time for rotation determination, making it feasible for prospective motion correction. The underlying concept is that the magnitude profile of an SNAV acquired by physically rotating an object will be the same as an SNAV acquired by rotating the SNAV trajectory. The preRot-SNAV method involves acquiring a baseline of pre-rotated SNAV templates by rotating the gradients of the scanner system, effectively rotating the SNAV trajectory. A measurement SNAV that is acquired during an image acquisition can then be compared to the baseline, and a rotation can be calculated by determining the best-matched template.

The rotation range chosen for this work was $\pm 6^\circ$ about the left-right (x) axis, $\pm 6^\circ$ about the anterior-posterior (y) axis, and $\pm 20^\circ$ about the superior-inferior (z) axis. This rotation space was sampled with 512 randomly generated angles to form a baseline of 512 pre-rotated templates, which took 26 s to acquire. The rotation angle of measurement SNAVs was calculated by determining the three best matched baseline SNAVs using the sum of squared differences cost function. A weighted average of these templates was calculated for the final rotation estimate. The translation of a measurement SNAV was then measured by calculating the phase shift between the measurement SNAV and the best-match template.

The SNAVs used in this study had a radius of 0.4 cm^{-1} and a minimum TR of 25 ms. The accuracy of the SNAV technique was evaluated both *in vitro* and *in vivo* and found to have an accuracy and precision of $0.8^\circ \pm 0.4^\circ$ for rotation measurement and $0.4 \text{ mm} \pm 0.2 \text{ mm}$ for translation measurement.

The preRot-SNAV technique can measure object rotations in tens of milliseconds on a personal computer, compared with the several seconds required by the conventional

iterative SNAV registration methods which are also prone to errors related to local-minimum convergence. These improvements make the preRot-SNAV technique a valuable tool for rigid-body motion correction applications in MRI.

1.5 *Motion Correction in Hybrid PET/MRI*

1.5.1 *Positron Emission Tomography*

Positron Emission Tomography (PET) is a diagnostic nuclear medicine technique that provides functional and metabolic information. In a PET exam a radionuclide – often ^{18}F is introduced into the body on a biologically active molecule called a radiotracer or radiopharmaceutical. A very common radiotracer is fluorodeoxyglucose (FDG). The tracer emits positrons in the decay process, which then annihilate with an electron to create two 511 keV gamma rays – emitted at almost 180° from each other – that are measured by the detector. The positron emitting radionuclide can then be localized along a straight line of coincidence. Typically, this data is collected in a format called “list-mode” data where each event (detector measures gamma rays) is stored with a time stamp. After all of the data has been acquired, the list-mode data can be reconstructed into a three-dimensional image. The sequential and inherently time-consuming nature of this data collection makes it susceptible to motion. If head motion occurs during a PET exam, there will be inconsistencies in the acquired data, which causes blurring and reduced image resolution.

1.5.2 *Hybrid PET/MRI*

Hybrid PET/MRI systems integrate both PET and MRI, providing complementary functional and anatomic information. There are several exciting applications for PET/MRI in neuro-imaging, including imaging in epilepsy,³⁵ and neurodegenerative disorders.³⁶ Hybrid PET/MRI could be a useful tool for both clinical and research neuro-imaging. However, both the MR and PET images are susceptible to motion.

1.5.3 *Motion correction in Hybrid PET/MRI*

In the previous sections, rigid-body motion measurement and correction techniques were discussed in the context of stand-alone MRI systems. The advent of integrated PET and MRI systems provides the opportunity to allow MRI navigator techniques to be used not only for correction of the MRI data but also the simultaneously acquired PET data.

Previous work has demonstrated the use of MRI motion measurement techniques to correct PET data. Studies using MRI navigators³⁷⁻³⁹ and also studies using active markers^{30,40} showed successful motion correction of PET data. An SNAV method for correcting both the simultaneously acquired PET and MRI data is presented in Chapter 3.

1.6 *Deep learning image-to-image translation*

So far, this chapter has focused on motion tracking, and motion correction based on known motion. Chapter 4 will present an alternative approach which makes use of recent advances in computer vision and deep learning. In Chapter 4, a method for using a deep convolutional neural network (DCNN) to perform retrospective motion correction is discussed. In this section I will give a brief overview of neural networks and deep learning, I will describe what deep convolutional neural networks are and how they can be applied for MR image-to-image translation, which refers to the approach of training a deep neural network to predict an image in one domain from an image in another domain. Image-to-image translation is the term often used in computer vision literature; it is commonly referred to as image synthesis in medical imaging literature.

1.6.1 *Neural networks*

One of the earliest neural networks was a single layer perceptron developed by Frank Rosenblott in 1958. It was found to be useful in classifying a set of inputs into one of two classes. A single layer perceptron binary classifier is illustrated in Figure 1-7. In the 1960's, work by Marvin Minsky and Seymour Papert suggested neural networks could only learn linearly separable functions. Following this report, very little research was done on neural networks until the 1980's. Key concepts in the 1980's that revived interest and research into neural networks, were distributed representation and backpropagation. Deep neural networks, which will be discussed in the next section were enabled by the improved computing resources and data availability in the 2000's.

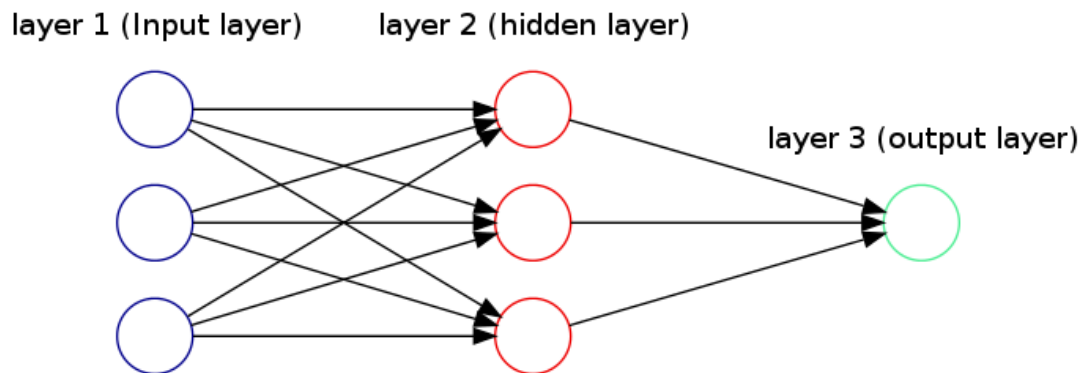


Figure 1-7 A single layer perceptron (SLP) has one hidden layer, an SLP binary classifier has a single output node which classifies the set of inputs into one of two classes.

1.6.2 *Deep learning*

Deep learning is an aspect of artificial intelligence and machine learning. Compared to traditional neural networks, deep neural networks have more layers, and increased model capacity. They can learn more abstract representations of data to perform complex tasks. This discussion is limited to supervised deep learning – a method of training a model to map some input to a desired output given many examples of

input/output pairs. A deep neural network (DNN) is an extension of a traditional neural network that has been used in supervised machine learning for decades. A diagram of a traditional neural network and deep neural network is shown in Figure 1-7. Traditional neural networks typically use handcrafted features and only one hidden layer (feature vector) to learn the mapping from input to output. DNNs have many hidden layers and can learn more abstract features from input data, which increases the complexity of the relationships they can model.⁴¹ DNN's are trained using a large number of input/output pairs. The learnable parameters are the weights; they are iteratively updated in order to minimize a loss function which quantifies the difference between the predicted and target outputs. Common loss functions are mean absolute error in applications with structured output and binary cross entropy for classification applications.⁴²

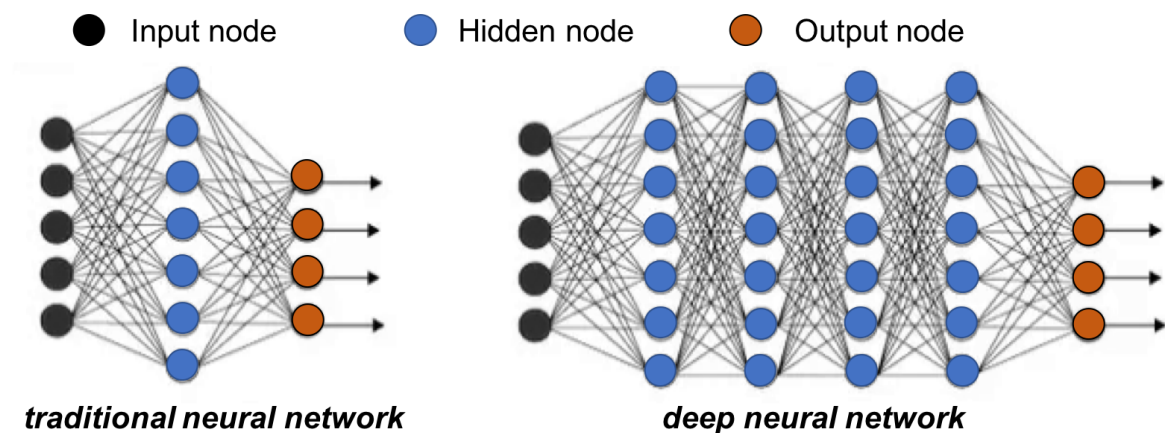


Figure 1-8 The simple neural network on the left has a single hidden layer (feature vector). The deep neural network has many feature vectors, which increases the model capacity and allows the model to learn more abstract and complex features from the input data. Each orange and blue node is the result of a non-linear activation function applied to the dot product of the feature vector in the previous layer and a learned weight vector.

1.6.3 *Deep convolutional neural networks*

A deep convolutional neural network (DCNN) is a type of DNN; it is a deep learning architecture that is often applied in the field of computer vision. It is composed of several layers, each of which learns increasingly more complex patterns and features in the data.⁴³ These features are extracted in order to perform the learning task, which may be image recognition,^{44,45} image synthesis,^{46,47} natural language processing or many other potential applications but is ultimately mapping some high dimensional input (e.g. an image) to a desired output. Diagrams of convolutional neural networks are shown in Figures 1-8 and 1-9. The two essential elements of any DCNN are convolution and non-linear activation. The convolution layers are the core building block of any DCNN; the convolution filters are made up of the learnable parameters, and the result of the convolution operation are the feature maps.⁴³ Non-linear activation allows the network to learn more complex non-linear relationships. Pooling and/or up-sampling, which reduce and increase the dimensionality of the feature maps are used in most DCNNs. Fully connected layers, in which each node is connected to each node of the previous layer, are used in some DCNNs – typically classifiers. Most modern DCNNs will also include batch normalization which normalizes the output of an activation layer and helps the network learn more quickly. Dropout, which is the practice of ignoring some percentage of nodes in each iteration of the training is also often included. Dropout regularizes the network, prevents overfitting, and improves the networks ability to generalize to new examples. The work presented in Chapter 4 makes use of two different kinds of DCNNs – a classifier network and an encoder-decoder network.

1.6.4 *DCNN: classifier*

DCNN classifiers are ubiquitous in computer vision applications. A DCNN can be trained to classify an image given a large sample of labeled examples. This is often done on natural images, for example the images of ImageNet and CIFAR, which consist

of large databases of natural images, like cars, animals, buildings etc.⁴⁸ ImageNet and CIFAR databases have served as benchmark data for the development of increasingly more sophisticated and more accurate classifiers. In recent years, these DCNN classifiers have become popular in medical imaging. VGGnet,⁴⁵ a very deep classifier originally developed for an ImageNet challenge is illustrated in Figure 1-8. Variations of this network have been used in classification of breast lesions⁴⁹ and lung tissue⁵⁰ as well as diagnosis of alzheimers.⁵¹ Image classifiers include convolution, pooling, non-linear activation and fully connected layers.



Figure 1-9 The VGG-net classifier consists of 16 trainable layers. These include convolutional layers (Conv), and fully connected (FC) layers. Max-pooling (Pool) layers are used for dimensionality reduction.

1.6.5 DCNN: encoder-decoder

DCNN encoder-decoder networks have become very popular in medical image segmentation and image synthesis. Unlike classifiers, the output of an encoder-decoder is high dimensional and structured (e.g. an image). The encoder portion of an encoder-decoder learns a high dimensional feature vector – an abstract representation of the input, and the decoder portion learns to reconstruct the desired output from this feature vector. Recently, encoder-decoder networks have been applied for image synthesis, which refers to the approach of training a deep neural network to predict an image in one domain from an image in another domain. For example, encoder-decoder networks have been used in predicting CT images from MR⁵² and generating images with different contrasts.⁵³ An illustration of a simple encoder-decoder used for this purpose is shown in Figure 1-9

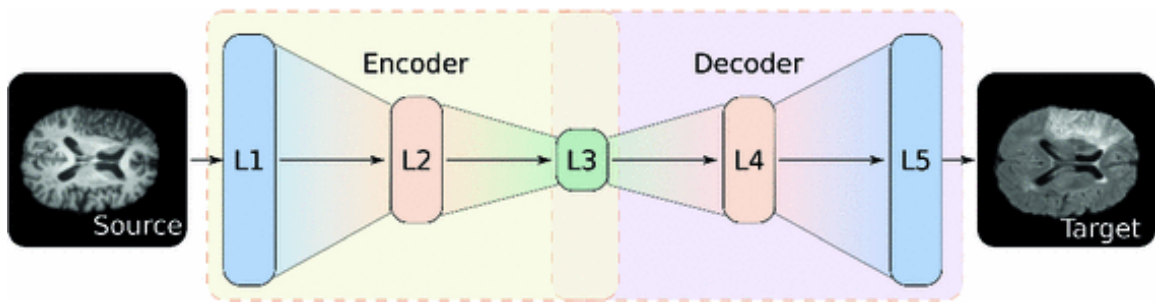


Figure 1-10 Encoder decoder network trained with T1/T2-FLAIR image pairs synthesizes a T2-FLAIR image from a T1-weighted image.⁵³ Each layer includes convolution and a sigmoid activation function. Max- pooling is used in the encoder portion of the network, while up-sampling is used in the decoder portion of the network. Figure from Sevetlidis et. al.,⁵³ reproduced with permission from Springer Nature.

1.6.6 Conditional generative adversarial networks

A conditional generative adversarial network (cGAN) is a novel deep learning technique for image synthesis.⁵⁴⁻⁵⁶ cGANs make use of an encoder-decoder network and a classifier. In a cGAN architecture, the encoder-decoder is referred to as a generator, and the classifier is referred to as a discriminator. A cGAN enforces realistic looking images in the network output. This is especially useful in enforcing sharpness in the predicted images, which have a tendency to be blurry when using a stand-alone encoder-decoder⁵⁴. The generator and discriminator are trained together; the generator is trained to minimize some image similarity metric (e.g. mean absolute error), while the discriminator is trained to classify an image as either an original target image, or a generator output. The discriminator loss is incorporated into the loss function of the generator to force the generator to predict images that look more like target images. cGANs have been recently applied for many applications in medical imaging, including estimating high quality images from low dose images in both PET⁵⁶ and CT.⁵⁷ An illustration of a popular cGAN implementation, pix2pix,⁵⁴ is shown in Figure 1-10. A cGAN method, adapted from pix2pix, for generating motion-corrected from motion-corrupted images is described in Chapter 4.

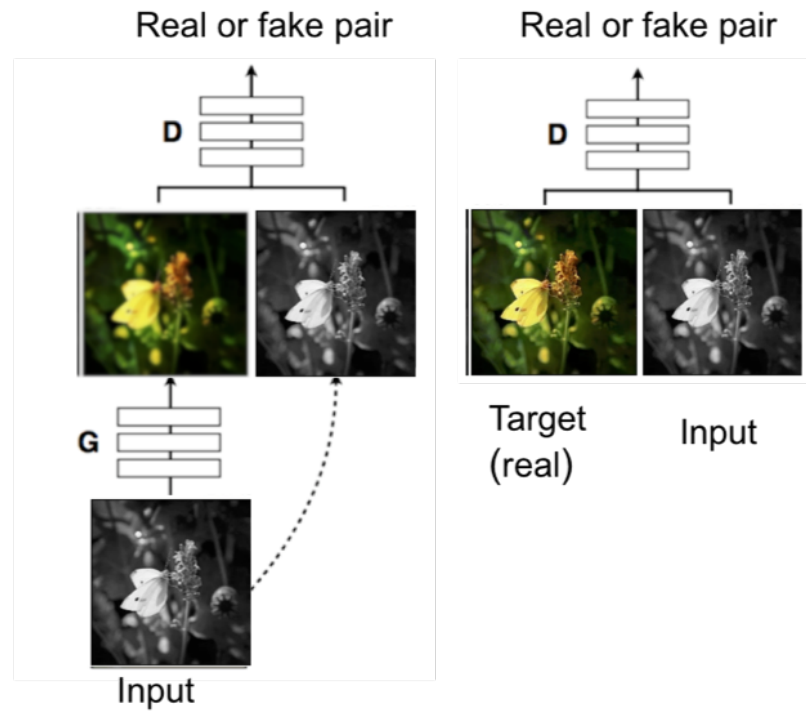


Figure 1-11 In this pix2pix illustration, the generator input is a black and white image and the target is the corresponding colour image. The generator predicted image (fake) along with its corresponding input, forms an image pair that is used to train the discriminator. Both fake and real image pairs are used to train the discriminator. The discriminator is trained to distinguish between target (real) images and fake images, while the generator is trained to predict images that are quantitatively similar to the target and will fool the discriminator. Figure adapted from Cho 2017.⁵⁸

1.7 Thesis outline

This thesis contains 5 chapters. The first chapter introduced the challenges of motion in MRI, as well as current techniques to address motion in both standalone MRI and hybrid PET/MRI. Chapter 1 also introduced deep learning and its application in image synthesis, which is relevant background information for Chapter 4.

Chapter 2 presents a novel method for retrospective rigid-body motion correction of brain images using spherical navigator echoes. A version of this Chapter entitled “Retrospective 3D motion correction using spherical navigator echoes” was published in Magnetic Resonance Imaging in 2016. The first development presented in this Chapter is an accelerated baseline technique which reduces the required baseline scan from 26 to 2.6s making SNAVs a much more practical tool for motion correction. The second development is the navigated image sequence used for *in vivo* motion correction.

Chapter 3 discusses the development and evaluation of Spherical Navigator Echoes for hybrid PET/MRI. A version of this Chapter entitled “Rigid-body motion correction in hybrid PET/MRI using spherical navigator echoes” was submitted for publication in Physics in Medicine and Biology, in July 2018.

Chapter 4 presents the development of a deep learning method for motion correction. The conditional adversarial network developed for motion correction MoCo-cGAN is trained and evaluated on images with simulated motion. A version of this Chapter entitled “Conditional generative adversarial network for three-dimensional rigid-body motion correction in MRI” was submitted for publication in Magnetic Resonance in Medicine in October 2018.

Chapter 5 summarizes the findings, contributions and limitations of this project and provides suggestions for future work.

1.8 References

- 1 Andre, J. B. *et al.* Toward Quantifying the Prevalence, Severity, and Cost Associated With Patient Motion During Clinical MR Examinations. *Journal of the American College of Radiology : JACR* **12**, 689-695,(2015).
- 2 Greene, D. J., Black, K. J. & Schlaggar, B. L. Considerations for MRI study design and implementation in pediatric and clinical populations. *Developmental Cognitive Neuroscience* **18**, 101-112,(2016).
- 3 Reuter, M. *et al.* Head motion during MRI acquisition reduces gray matter volume and thickness estimates. *NeuroImage* **107**, 107-115,(2015).
- 4 Power, J. D., Barnes, K. A., Snyder, A. Z., Schlaggar, B. L. & Petersen, S. E. Spurious but systematic correlations in functional connectivity MRI networks arise from subject motion. *NeuroImage* **59**, 2142-2154,(2012).
- 5 Satterthwaite, T. D. *et al.* Impact of in-scanner head motion on multiple measures of functional connectivity: Relevance for studies of neurodevelopment in youth. *NeuroImage* **60**, 623-632,(2012).
- 6 Ehman, R. L. & Felmlee, J. P. Adaptive technique for high-definition MR imaging of moving structures. *Radiology* **173**, 255-263,(1989).
- 7 Fu, Z. W. *et al.* Orbital navigator echoes for motion measurements in magnetic resonance imaging. *Magnetic resonance in medicine* **34**, 746-753,(1995).
- 8 van der Kouwe, A. & Dale, A. Real-time motion correction using octant navigators. *NeuroImage* **13**, 48,(2001).
- 9 van der Kouwe, A. J., Benner, T. & Dale, A. M. Real-time rigid body motion correction and shimming using cloverleaf navigators. *Magnetic resonance in medicine* **56**, 1019-1032,(2006).
- 10 Petrie, D. W., Costa, A. F., Takahashi, A., Yen, Y. F. & Drangova, M. Optimizing spherical navigator echoes for three-dimensional rigid-body motion detection. *Magnetic resonance in medicine* **53**, 1080-1087,(2005).
- 11 Welch, E. B., Manduca, A., Grimm, R. C., Ward, H. A. & Jack, C. R., Jr. Spherical navigator echoes for full 3D rigid body motion measurement in MRI. *Magnetic resonance in medicine* **47**, 32-41,(2002).
- 12 Thesen, S., Heid, O., Mueller, E. & Schad, L. R. Prospective acquisition correction for head motion with image-based tracking for real-time fMRI. *Magnetic resonance in medicine* **44**, 457-465,(2000).

- 13 White, N. *et al.* PROMO: Real-time prospective motion correction in MRI using image-based tracking. *Magnetic resonance in medicine* **63**, 91-105,(2010).
- 14 Tisdall, M. D. *et al.* Prospective motion correction with volumetric navigators (vNavs) reduces the bias and variance in brain morphometry induced by subject motion. *NeuroImage* **127**, 11-22,(2016).
- 15 Tisdall, M. D. *et al.* Volumetric navigators for prospective motion correction and selective reacquisition in neuroanatomical MRI. *Magnetic resonance in medicine* **68**, 389-399,(2012).
- 16 Gallichan, D., Marques, J. P. & Gruetter, R. Retrospective correction of involuntary microscopic head movement using highly accelerated fat image navigators (3D FatNavs) at 7T. *Magnetic resonance in medicine* **75**, 1030-1039,(2015).
- 17 Engstrom, M., Martensson, M., Avventi, E., Norbeck, O. & Skare, S. Collapsed fat navigators for brain 3D rigid body motion. *Magnetic resonance imaging* **33**, 984-991,(2015).
- 18 Tremblay, M., Tam, F. & Graham, S. J. Retrospective coregistration of functional magnetic resonance imaging data using external monitoring. *Magnetic resonance in medicine* **53**, 141-149,(2005).
- 19 Zaitsev, M., Dold, C., Sakas, G., Hennig, J. & Speck, O. Magnetic resonance imaging of freely moving objects: prospective real-time motion correction using an external optical motion tracking system. *NeuroImage* **31**, 1038-1050,(2006).
- 20 Aksoy, M. *et al.* Hybrid Prospective and Retrospective Head Motion Correction to Mitigate Cross-Calibration Errors. *Magnetic resonance in medicine* **67**, 1237-1251,(2012).
- 21 Maclaren, J., Aksoy, M., Ooi, M. B., Zahneisen, B. & Bammer, R. Prospective motion correction using coil-mounted cameras: Cross-calibration considerations. *Magnetic resonance in medicine* **79**, 1911-1921,(2018).
- 22 Singh, A. *et al.* Optical tracking with two markers for robust prospective motion correction for brain imaging. *Magma (New York, N.Y.)* **28**, 523-534,(2015).
- 23 Forman, C., Aksoy, M., Hornegger, J. & Bammer, R. Self-encoded marker for optical prospective head motion correction in MRI. *Medical image analysis* **15**, 708-719,(2011).
- 24 Schulz, J. *et al.* An embedded optical tracking system for motion-corrected magnetic resonance imaging at 7T. *Magma (New York, N.Y.)* **25**, 443-453,(2012).

- 25 Stucht, D. *et al.* Highest Resolution In Vivo Human Brain MRI Using Prospective Motion Correction. *PloS one* **10**, e0133921,(2015).
- 26 Andrews-Shigaki, B. C., Armstrong, B. S., Zaitsev, M. & Ernst, T. Prospective motion correction for magnetic resonance spectroscopy using single camera Retro-Grate reflector optical tracking. *Journal of magnetic resonance imaging : JMRI* **33**, 498-504,(2011).
- 27 Aksoy, M., Maclaren, J. & Bammer, R. Prospective motion correction for 3D pseudo-continuous arterial spin labeling using an external optical tracking system. *Magnetic resonance imaging* **39**, 44-52,(2017).
- 28 Ooi, M. B., Krueger, S., Thomas, W. J., Swaminathan, S. V. & Brown, T. R. Prospective real-time correction for arbitrary head motion using active markers. *Magnetic resonance in medicine* **62**, 943-954,(2009).
- 29 Ooi, M. B., Krueger, S., Muraskin, J., Thomas, W. J. & Brown, T. R. Echo-planar imaging with prospective slice-by-slice motion correction using active markers. *Magnetic resonance in medicine* **66**, 73-81,(2011).
- 30 Huang, C. *et al.* MR-based motion correction for PET imaging using wired active MR microcoils in simultaneous PET-MR: phantom study. *Medical Physics* **41**, 041910,(2014).
- 31 Maclaren, J., Herbst, M., Speck, O. & Zaitsev, M. Prospective motion correction in brain imaging: a review. *Magnetic resonance in medicine* **69**, 621-636,(2013).
- 32 Liu, J. & Drangova, M. Phase-unwrapping algorithm for translation extraction from spherical navigator echoes. *Magnetic resonance in medicine* **63**, 510-516,(2010).
- 33 Liu, J. & Drangova, M. Combination of multidimensional navigator echoes data from multielement RF coil. *Magnetic resonance in medicine* **64**, 1208-1214,(2010).
- 34 Liu, J. & Drangova, M. Rapid six-degree-of-freedom motion detection using prerotated baseline spherical navigator echoes. *Magnetic resonance in medicine* **65**, 506-514,(2011).
- 35 Ding, Y. S., Chen, B. B., Glielmi, C., Friedman, K. & Devinsky, O. A pilot study in epilepsy patients using simultaneous PET/MR. *American Journal of Nuclear Medicine and Molecular Imaging* **4**, 459-470,(2014).
- 36 Barthel, H., Schroeter, M. L., Hoffmann, K. T. & Sabri, O. PET/MR in dementia and other neurodegenerative diseases. *Seminars in nuclear medicine* **45**, 224-233,(2015).

- 37 Keller, S. H. *et al.* Sparsely sampled MR navigators as a practical tool for quality control and correction of head motion in simultaneous PET/MR. *EJNMMI physics* **1**, A36,(2014).
- 38 Chen, K. T. *et al.* MR-assisted PET motion correction in simultaneous PET/MRI studies of dementia subjects. *Journal of magnetic resonance imaging : JMRI*,(2018).
- 39 Bickell, M., Koesters, T., Boada, F. & Nuyts, J. PET motion correction using MR-derived motion parameters. *EJNMMI physics* **1**, A53,(2014).
- 40 Huang, C. *et al.* Motion compensation for brain PET imaging using wireless MR active markers in simultaneous PET-MR: phantom and non-human primate studies. *NeuroImage* **91**, 129-137,(2014).
- 41 Goodfellow, I., Bengio, Y. & Courville, A. Part II: Modern Practical Deep Networks in *Deep Learning* (MIT press, 2016).
- 42 Litjens, G. *et al.* A survey on deep learning in medical image analysis. *Medical image analysis* **42**, 60-88,(2017).
- 43 Goodfellow, I., Bengio, Y. & Courville, A. Part 2.9 -Convolutional Networks in *Deep Learning* (MIT press, 2016).
- 44 Pak, M. & Kim, S. A review of deep learning in image recognition in 2017 4th *International Conference on Computer Applications and Information Processing Technology (CAIPT)*. 1-3.
- 45 Simonyan, K. & Zisserman, A. Very Deep Convolutional Networks for Large-Scale Image Recognition. *arXiv:1409.1556* (2015).
- 46 Zhang, H. *et al.* StackGAN: Text to Photo - realistic Image Synthesis with Stacked Generative Adversarial Networks. *arXiv:1612.03242*,(2017).
- 47 Nie, D. *et al.* Medical Image Synthesis with Context-Aware Generative Adversarial Networks. *Medical image computing and computer-assisted intervention* **10435**, 417-425,(2017).
- 48 Krizhevsky, A., Sutskever, I. & Hinton, G. E. ImageNet Classification with Deep Convolutional Neural Networks in *Advances in Neural Information Processing Systems* 1097-1105 (Curran Associates, Inc., 2012).
- 49 Antropova, N., Abe, H. & Giger, M. L. Use of clinical MRI maximum intensity projections for improved breast lesion classification with deep convolutional neural networks. *Journal of medical imaging (Bellingham, Wash.)* **5**, 014503,(2018).

- 50 Anthimopoulos, M., Christodoulidis, S., Ebner, L., Christe, A. & Mougiakakou, S. Lung Pattern Classification for Interstitial Lung Diseases Using a Deep Convolutional Neural Network. *IEEE transactions on medical imaging* **35**, 1207-1216,(2016).
- 51 Sarraf, S., DeSouza, D. D., Anderson, J. & Tofighi, G. DeepAD: Alzheimer's Disease Classification via Deep Convolutional Neural Networks using MRI and fMRI. *bioRxiv*,(2017).
- 52 Jang, H., Liu, F., Zhao, G., Bradshaw, T. & McMillan, A. B. Technical Note: Deep learning based MRAC using rapid ultrashort echo time imaging. *Medical Physics*,(2018).
- 53 Sevetlidis, V., Giuffrida, M. V. & Tsiftaris, S. A. Whole Image Synthesis Using a Deep Encoder-Decoder Network in *Simulation and Synthesis in Medical Imaging*. (eds Sotirios A. Tsiftaris, Ali Gooya, Alejandro F. Frangi, & Jerry L. Prince) 127-137 (Springer International Publishing).
- 54 Isola, P., Zhu, J.-Y., Zhou, T. & Efros, A. Image-to-Image Translation with Conditional Adversarial Networks. *arXiv:1611.07004 [cs.CV]*,(2017).
- 55 Kim, K. H., Do, W. J. & Park, S. H. Improving resolution of MR images with an adversarial network incorporating images with different contrast. *Medical physics* **45**, 3120-3131,(2018).
- 56 Wang, Y. *et al.* 3D conditional generative adversarial networks for high-quality PET image estimation at low dose. *NeuroImage* **174**, 550-562,(2018).
- 57 Wolterink, J. M., Leiner, T., Viergever, M. A. & Isgum, I. Generative Adversarial Networks for Noise Reduction in Low-Dose CT. *IEEE transactions on medical imaging* **36**, 2536-2545,(2017).
- 58 Author. Image Translation with GAN. Slideshare: Data and Analytics (2017). <<https://www.slideshare.net/JunhoChol/image-translation-with-gan>>.

2 Retrospective 3D motion correction in MRI using SNAVs

2.1 Introduction

Despite the advent of continually faster acquisition strategies, subject motion remains a problem in MRI and numerous techniques have been proposed to correct it. One such method is the use of navigator echoes,¹ first proposed by Ehman *et al.* in 1989 to measure and correct rigid body motion. Pencil beam navigators, frequently used in cardiac imaging^{2,3} and orbital navigators⁴⁻⁶ are limited to motion measurement in one and two dimensions respectively. Three-dimensional (3D) motion can be measured using cloverleaf⁷ or spherical^{8,9} k-space navigators. The spherical navigator echo (SNAV), which samples a spherical shell in k space, can measure motion in 6 degrees of freedom⁹ by using relationships that follow from the Fourier shift and rotation theorems.⁴ First described by Welch *et al.*^{9,10} SNAVs promised simultaneous 3D motion measurements but were impractical due to long measurement and processing times. The polar SNAV approach¹¹ proposed a faster registration technique but translation estimates remained too slow for prospective correction.

These limitations with navigator echoes have led to the development of alternative motion correction strategies – primarily image based and optical-tracking based methods. Image based tracking methods¹²⁻¹⁹ and fat navigators²⁰⁻²² involve the acquisition of low-resolution images to track – and correct for – motion throughout image acquisition. While highly effective, these methods have been applied only to spin-echo based imaging because of the lengthy acquisition and processing of low-resolution images used to quantify motion. Optical tracking methods, which have been used in many studies,²³⁻²⁸ use external camera systems to measure and correct for head motion in real time. However, these techniques rely on tracking devices mounted on the subject as well as MR-compatible external hardware that require cross-calibration between the tracking system and the scanner’s frame of reference.

Therefore, while recent work in the field has largely moved away from k-space navigators, SNAVs remain a promising alternative, as they are very rapid to acquire and have been limited mainly by the processing method. A solution to the slow processing speed was proposed by Liu and Drangova,²⁹ who demonstrated that SNAV processing can be reduced from several seconds to less than 20 ms, using template matching instead of the iterative registration and minimization algorithm used previously. This technique – referred to as the preRot-SNAV technique – relies on the acquisition of a set of baseline template SNAVs with known rotated trajectories covering the entire range of anticipated motion. While accurate motion tracking was demonstrated with the preRot-SNAV technique, its clinical applicability was limited because the acquisition of the pre-rotated baseline required 26 s of “no motion” during baseline acquisition.

Building on the proposed preRot-SNAV technique, this Chapter presents the first application of SNAVs for *in vivo* motion correction. Retrospective motion correction of 3D gradient echo images was achieved by implementing a modification of the preRot technique, which acquires a subset of pre-rotated baseline templates followed by offline simulation of axial rotation to each of the acquired SNAV templates. This “hybrid baseline” preRot-SNAV technique is advantageous as it reduces the likelihood of subject motion during template acquisition; it is first evaluated in phantom studies then retrospective motion correction is demonstrated in multiple volunteers with single and multi-channel RF coils.

2.2 Methods

We first describe the SNAV acquisition with an overview of the proposed hybrid preRot-SNAV approach and follow with a description of phantom experiments that evaluate the hybrid preRot-SNAV motion measurement accuracy, before demonstrating retrospective *in vivo* motion correction of 3D spoiled gradient echo

(SPGR) images. All experiments were performed on a 3.0 T whole-body MRI scanner (GE 750, GE Medical Systems, Milwaukee, WI). Phantom experiments were performed using a birdcage RF head coil and *in vivo* experiments were performed using both the single-channel and eight-channel RF head coils. The Research Ethics Board at our institution approved this human-subject study and informed consent was obtained from the volunteers.

2.2.1 *PreRot-SNAV overview*

Briefly, the original preRot-SNAV method²⁹ requires the acquisition of 512 baseline SNAV templates, pre-rotated by a uniform distribution of random Euler angles that sample a 3D rotation space. The pre-rotated templates are acquired by rotating the gradient co-ordinate system to yield angles that cover the range of expected rotations, e.g. for head motion a range of $\pm 6^\circ$ about the right-left (X) and the anterior-posterior axis (Y) axes, and $\pm 20^\circ$ about the superior-inferior (Z) axis was shown to be sufficient.²⁹ Rotation angles between an unknown physically transformed position and the reference (baseline) position are determined by identifying the template with the lowest sum of squared differences between the baseline templates and SNAVs acquired at the transformed position. Following rotation determination, translations are calculated from the phase difference between the best-matched template and the SNAV acquired at the transformed position. For large translations, SNAV phase unwrapping is performed.³⁰

2.2.2 *Hybrid baseline strategy*

In this study, the acquisition of the baseline SNAV template data set is accelerated by utilizing a hybrid approach: baseline templates pre-rotated only about two axes are acquired, and SNAV templates corresponding to rotations about the third axis are simulated. First, baseline SNAV templates are acquired by rotating the gradients to

yield rotations θ_x and θ_y . Each acquired SNAV is then rotated by a set of predetermined θ_z to cover the range of anticipated rotations in the axial direction. For each rotated SNAV a simulated SNAV profile is generated using interpolation.

The set of Euler angles covering the predefined rotation range can be sampled using numerous strategies; previously a random distribution of sampling was used, here we investigate two different strategies – one that acquires 170 SNAVs and the other – 82 SNAVs. For a predefined rotation range of $\pm 6^\circ$ in θ_x and θ_y , the 170-hybrid strategy acquires 169 SNAVs that cover the range in steps of 1° , plus an additional non-rotated SNAV acquired at the end to verify that the object has not moved during baseline acquisition (resulting in a total of 170 SNAV templates). For the 82-hybrid strategy, the step size between Euler angles in θ_x and θ_y is 2° , with additional angles generated at $\pm 1^\circ$ to increase sensitivity to low magnitude rotations. In each case, hybrid baseline datasets are generated by simulating SNAV templates that mimic θ_z rotations with 1° increment, within a predetermined rotation range ($\pm 20^\circ$ in this study).

SNAV template simulation is performed using interpolation, following techniques described earlier.^{8,9} Briefly, the 3D simulated SNAV coordinates are converted to polar coordinates (latitude and longitude) then the SNAVs, at the locations of the rotated coordinates, are linearly interpolated. The simulated and acquired baseline SNAV template datasets are combined to form a hybrid SNAV baseline dataset. Following the simulation of additional templates, the 170-hybrid and 82-hybrid baselines have 6970 (41×170) and 3362 (41×82) templates respectively.

Finally, using the acquired and simulated baseline templates, rotations are determined by identifying the best match templates from this hybrid baseline. Specifically, this was achieved by first calculating a cost function equal to the sum of squared differences between the acquired template and the baseline templates. Subsequently a weighted

average²⁹ rotation angle was calculated from the templates with a cost function value falling within 10% of the lowest calculated cost.

2.2.3 *SNAV trajectory and acquisition*

SNAVs were acquired in 2 shots (2 hemispheres), with a variable sampling density, as described by Petrie *et al.*⁸ The SNAV sequence is a modified gradient echo sequence with 22 helical turns and 1254 sample points per hemisphere. Processing of all navigators, including the simulation of the hybrid baseline (described below), was performed off-line on a 2.8-GHz Intel Core i5 processor using MATLAB (Math Works, Natick, MA). For all SNAVs acquired in this study a bandwidth of 125 kHz, and a SNAV radius $k_\rho = 0.4 \text{ cm}^{-1}$ were used. An SNAV radius of 0.4 cm^{-1} was shown to be optimal for head imaging in prior work^{8,29}. the readout time of a single SNAV hemisphere was 10 ms.

2.2.4 *In vitro accuracy evaluation*

Prior to *in vivo* evaluation, the accuracy of the hybrid SNAV baseline strategies were tested in phantom experiments using an agar filled plastic skull with dimensions corresponding to about 75% of the size of an adult skull. To evaluate the accuracy of rotation estimation using the two proposed hybrid baseline strategies, three sets of baseline template SNAVs were acquired at a reference position (prior to moving the phantom) – one each with 512, 170, and 82 templates, as described above. The 512-template baseline dataset²⁹ was used to determine the true phantom rotation. Subsequently, the phantom was manually placed at three arbitrary orientations (trials) and SNAVs were acquired at each position. 32 SNAVs were acquired in order to determine measurement precision. Phantom rotation at each trial position was estimated using the preRot method using the 512, 170-hybrid, and 82-hybrid baseline

datasets. Residual translations that occurred when rotating the phantom were also measured.

To further assess the hybrid baseline SNAV's accuracy in translation measurements, we measured phantom translation with and without rotation from a reference position. The phantom was placed on a linear motion stage³¹ (MR_1A_XRV2, Vital Biomedical, London, Canada) oriented along the bore's Z-axis and 82-hybrid baseline SNAVs were acquired at a reference position. 32 SNAVs were then acquired at the reference position and at each of four translated positions: 2 mm, 5 mm, 10 mm and 15 mm. The phantom was subsequently returned to the reference position, rotated arbitrarily then translated to the same positions; SNAVs were acquired at each position.

Finally, to demonstrate the hybrid baseline SNAVs ability to accurately measure dynamic compound motion, the phantom was rotated and the linear motion stage was set to undergo sinusoidal motion with amplitude of 10 mm and a period of 3 s. While the phantom was moving, SNAVs were acquired continuously for 26 s. The rotation and translations were extracted from each SNAV and the dynamic motion profile was reconstructed. The rotation and translation measurements were determined using the 82-hybrid baseline template dataset and compared to the known translations.

2.2.5 *Navigated pulse sequence*

Prior to *in vivo* evaluation, a navigated image sequence was developed based on a modified spoiled gradient echo sequence (SPGR-SNAV). SNAVs were interleaved into the product 3D SPGR pulse sequence to follow the acquisition of every four Cartesian lines of k-space data. Because the full SNAV acquisition requires 2 shots, a full navigator is acquired for every six RF pulses, thereby resulting in an increase of scan time by 33%. By keeping the repetition time (TR) and the RF pulses are identical for the image acquisition and navigator, the steady state is not disturbed.³² The sequence

parameters used were as follows: matrix size = 256x160x124, TE/TR = 3.9/15 ms; image bandwidth = 62.5 kHz, SNAV bandwidth = 125kHz, flip angle = 8°; slice thickness = 1.5mm; field of view = 24x24x18.6 cm, readout direction was right/left. Following zero filling of the unacquired k-space lines, the reconstructed matrix size was 256x256x196. The duration of the scan was 7.5 mins.

2.2.6 *In vivo motion experiments*

First, to demonstrate that the insertion of SNAVs does not affect image quality, both the product SPGR sequence and the SPGR-SNAV sequence were executed while a volunteer remained stationary. Next, three volunteers were each scanned twice using the SPGR-SNAV sequence: once using the single-channel head coil and once with the 8-channel head coil. The volunteers performed step-wise motion; they were instructed to move approximately every 50 s of the 7.5 min scan.

2.2.7 *Analysis and retrospective correction*

The motion parameters were extracted from each of the interleaved SNAVs as described above. To correct the images, phase shifts were first applied in order to correct for the measured translations; next, the 3D coordinates of the phase-corrected data were rotated based on the measured rotation. K-space data were then interpolated at the transformed coordinates using spline interpolation. The NuFFT gridding algorithm³³ and MATLAB's spline interpolation were compared for this interpolation step; minimal differences were observed, therefore spline interpolation, the least computationally demanding, was chosen for this study. The transformed k-space data were then Fourier transformed into the final motion corrected images, which were compared to both the reference, and original motion-degraded images. For the multi-channel acquisitions, before extracting motion estimates, the SNAVs were summed

across channels to form a combined navigator.³⁴ The k-space data from each channel was corrected before Fourier transformation and sum of squares coil recombination.

2.2.8 *Partial SNAV evaluation in vivo*

Additional analyses were performed to assess whether further reduction in SNAV acquisition time can be achieved by reducing the number of SNAV readout points, while retaining the accuracy of motion measurements. The SNAV trajectory used in this study consists of 22 helical turns per hemisphere; all *in vivo* data acquired above were also processed with truncated SNAVs using only a limited number of helical turns (between 2 and 22) that sampled the lowest equatorial portion of each hemisphere (belt around the equator), corresponding to SNAV readout lengths between 1.4 and 10 ms per hemisphere. For this experiment the 82-template baseline was used. Motion corrected images were generated for each number of turns. Retrospectively corrected images were compared qualitatively as well as quantitatively using the image entropy (E) as the metric:

$$E = -\sum_{p=1}^{n_p} \frac{I_p}{I_{total}} \ln \left(\frac{I_p}{I_{total}} \right), \quad (2.1)$$

where p is the pixel index, n_p is the total number of image pixels, and I_p is the pixel intensity.³⁵ I_{total} is the total image energy given by:

$$I_{total} = \sqrt{\sum_{\rho=1}^{n_\rho} I_\rho^2}. \quad (2.2)$$

Image entropy has been used as a quality metric in prior retrospective motion correction applications.^{35,36} It describes the probability distribution of pixel intensities in the image. For an image with more blurring, a higher entropy value is expected.

2.3 Results

2.3.1 Static phantom rotation and translation measurements

Simulated templates were generated for both the 170- and 82- template hybrid baselines. The computation time required to simulate all templates was 31 s and 15 s for the 170-hybrid and 82-template hybrid baselines, respectively. Measured phantom rotations for the three trial orientations of the phantom are shown in Figure 2-1. The “gold standard” rotations $[\theta_x, \theta_y, \theta_z]$, as determined by the 512-baseline, were $[-4.7^\circ, -1.3^\circ, -8.8^\circ]$, $[-0.1^\circ, 1.7^\circ, 11.0^\circ]$, and $[0.0^\circ, 1.3^\circ, -10.3^\circ]$ for trials 1, 2, and 3 respectively. Compared to the measurements made using the 512-template baseline dataset, the measurements performed using both the 82-hybrid and 170-template hybrid baselines for θ_x , θ_y and θ_z were within 0.9° , 0.9° and 0.4° , respectively. In each case, the standard deviation of the 32 repeated measurements was 0.2° or less and the bounds of the 95% confidence interval is within 0.08° of the mean. When the phantom was repositioned for the rotation trials, translations also occurred. These translations, also shown in Figure 2-1, range between -8.4 mm and 5.6 mm. Measurements performed using the 82-hybrid and 170-hybrid baselines for X, Y and Z were within 1.0 mm, 0.4 mm, and 0.7 mm of the 512-template standard, respectively.

The accuracy of measuring static translations for a rotated and non-rotated phantom, using the linear stage, showed excellent accuracy ($r^2 > 0.99$ for both the non-rotated and rotated cases). The standard deviations from the 32 SNAVs at each position ranged from 0.03 mm to 0.07 mm and the bounds of the 95% confidence intervals were all within 0.03 mm of the mean values. All of the measured mean translations, both with and without rotation, were within 0.3 mm of the known stage translations.

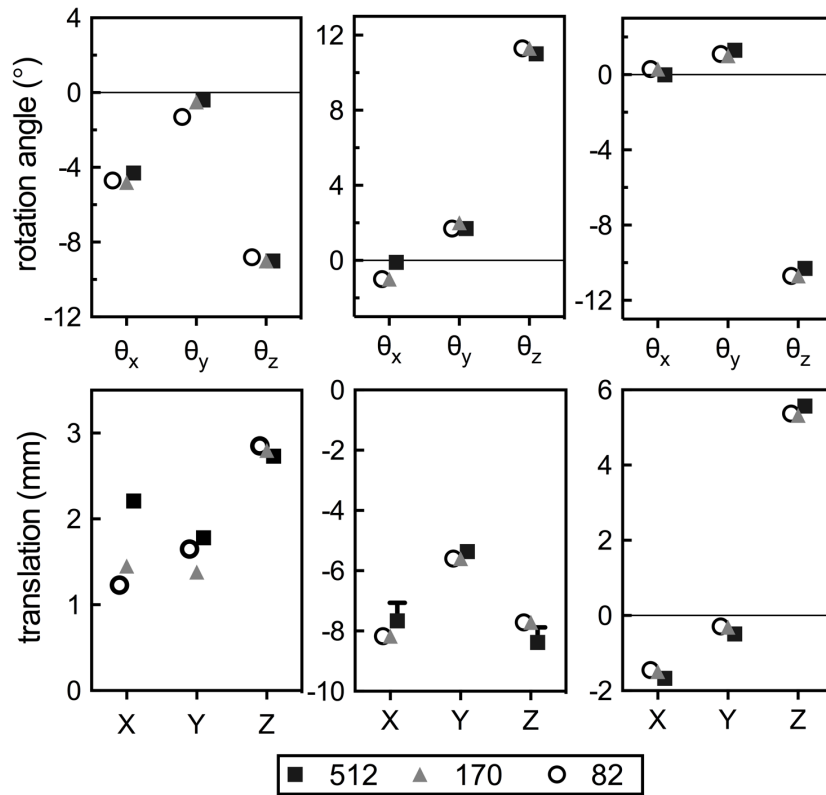


Figure 2-1 Rotation (a-c) and translation (d-f) measurements of three trial repositions of the skull phantom. Results obtained using the full 512-template baseline dataset is plotted with those obtained using the 170- and 82-hybrid baseline datasets. The error bars, representing standard deviation of 32 SNAV measurements, are smaller than the symbols in most cases (maximum 0.2° , 0.6 mm).

2.3.2 *Dynamic compound motion measurements*

The results of the dynamic motion experiments are shown in Figure. 2-2a (rotation) and 2-2b (translation). As expected, the rotation values were constant over the duration of the experiment, with small fluctuations observed at the extremes of the sinusoidal translation. The average rotation measured throughout the 26 s of motion was $\theta_x = -1.3^\circ \pm 0.16^\circ$ (95% CI: -1.37, -1.34), $\theta_y = 3.7^\circ \pm 0.2^\circ$ (95% CI: 3.71, 3.75) and $\theta_z = -11.0 \pm 0.04^\circ$ (95% CI: -10.99, -10.98). These rotation estimates also agreed (maximum difference 0.2°) with those measured when the phantom was stationary at the reference

position ($\theta_x = -1.5^\circ$, $\theta_y = 3.5^\circ$, $\theta_z = -11.0^\circ$). Translation measurements in the Z-direction agree with the known (prescribed) translations (Figure 2-2c). Small translations (< 0.4 mm) were measured in the X and Y directions, suggesting a slight misalignment of the linear stage with the scanner's Z-axis.

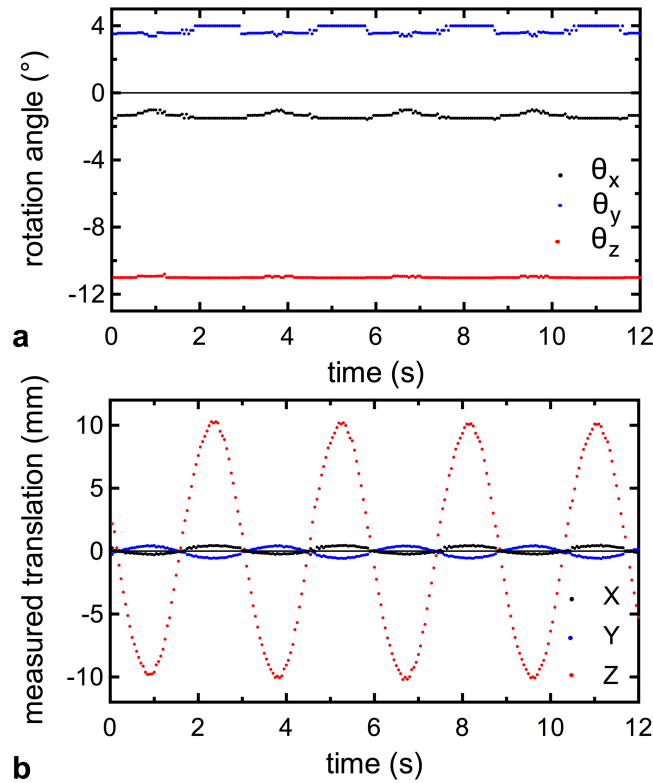


Figure 2-2 Rotation (a) and translation (b) results for the compound motion experiments using 82-hybrid baselines, demonstrate the ability to follow compound motion over time (12 of the 26 acquired seconds are shown). Rotation estimates at the stationary reference position were $\theta_x = -1.5^\circ$, $\theta_y = 3.5^\circ$, $\theta_z = -11.0^\circ$. The standard deviation of the rotation measurements is lower than 0.2° and the variation is attributed to the large translation component. The motion stage was programmed to move the rotated phantom sinusoidally with a period of 3 s and amplitude of 10 mm.

2.3.3 *Effect of SNAVs on SPGR images*

To evaluate whether the SNAVs affect the image intensity or contrast we compared the images acquired using the SPGR sequence with the images acquired with the SPGR-SNAV sequence. Figure 2-3 shows both of these images for a single volunteer, demonstrating that incorporation of the SNAVs did not affect the appearance of the image. While the volunteer was not moving intentionally, rotations up to 0.8° (Figure 2-3d) and translations less than 0.4 mm were recorded, with a single larger translation in Z (Figure 2-3e). Retrospective motion correction was applied to the SPGR-SNAV image (Figure 2-3c) to demonstrate that the process of retrospective correction – for this negligible amount of motion – did not introduce additional artefacts. Similar results were achieved in all volunteers.

2.3.4 *Retrospective motion correction*

In a comparison of the 170-hybrid and 82-hybrid baseline methods *in vivo*, the quantitative motion profiles generated using both methods were almost identical and the motion-corrected images appeared very similar. The 82-hybrid baseline can be acquired faster and therefore this method was used for retrospective motion correction in this study. Representative results of retrospective motion correction using a single channel birdcage coil are shown in Figure 2-4, which compares a reference (no motion) image (Figure 2-4a) to a motion-corrupted image (Figure 2-4b) and retrospectively motion-corrected image obtained using the 82-hybrid (Figure 2-4c) baseline strategy. For this experiment the volunteer was asked to rotate their head in both the θ_x and θ_z directions (nodding and axial rotation). The measured motion agrees well with the intended motion; we see step-like rotations about X and Z with accompanying Z and X translations at the time-points of directed motion. The uncorrected image acquired during motion has distortions, as expected. Excellent correction of these artefacts is

observed in the corrected image (Figure 2-4c). The measured rotations and translations are shown Figure 2-4d and 2-4e respectively.

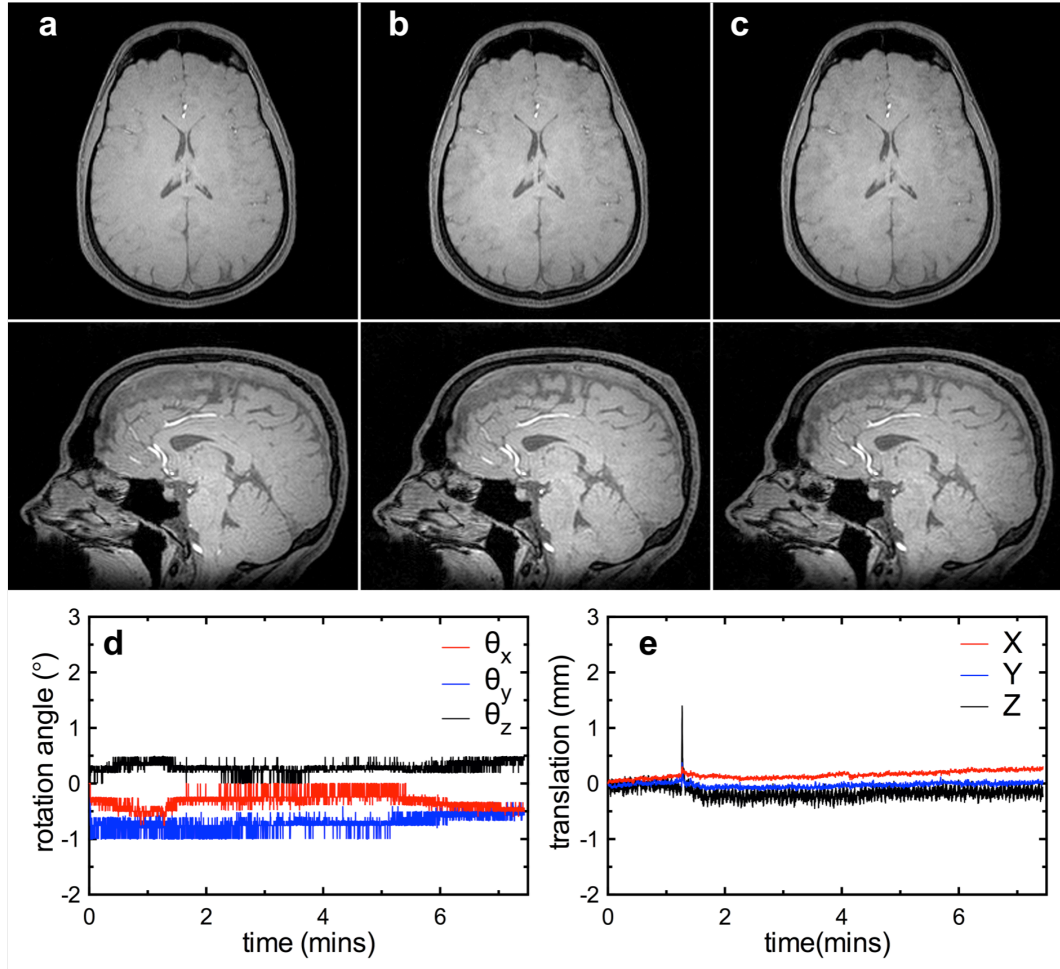


Figure 2-3 Axial and sagittal slice from the 3D image acquired with the product SPGR sequence (a) and the SPGR-SNAV sequence (b). The SPGR-SNAV image was retrospectively corrected (c) using measured SNAV rotation (d) and translation (e). The oscillations in z translation correspond to the respiratory rate of the subject. All three images have the same image entropy.

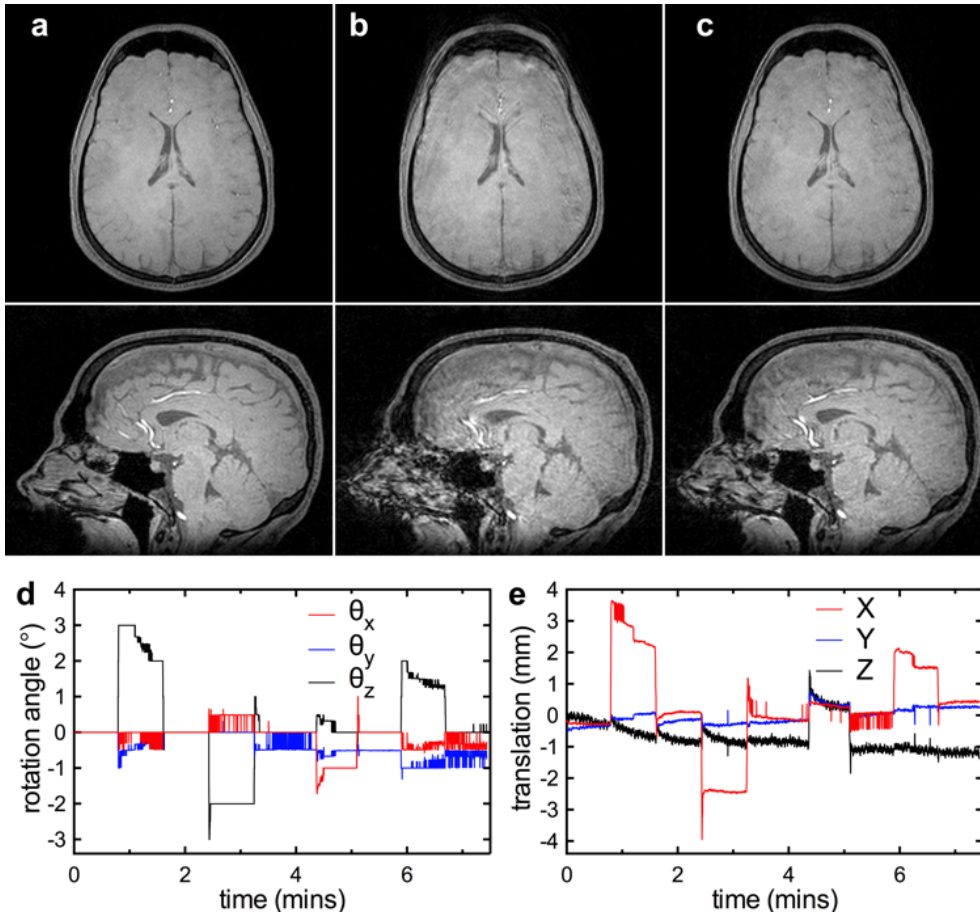


Figure 2-4 Axial and sagittal slices acquired with a single-channel head coil: (a) no motion reference image; (b) uncorrected image acquired with intended rotation; (c) motion corrected image. The measured rotations and translations, obtained using the 82-hybrid baseline, are shown in (d) and (e).

Representative results of motion correction, with a different volunteer, using an 8-channel head coil are shown in Figure 2-5. Once again retrospective motion correction was achieved, with the corrected images shown in panel (c) demonstrating fewer motion-related artefacts when compared to the uncorrected images in (b). Substantial correction of *in vivo* head motion up to 4° and 4 mm was observed in six acquired data sets with 3 volunteers and 2 RF coils.

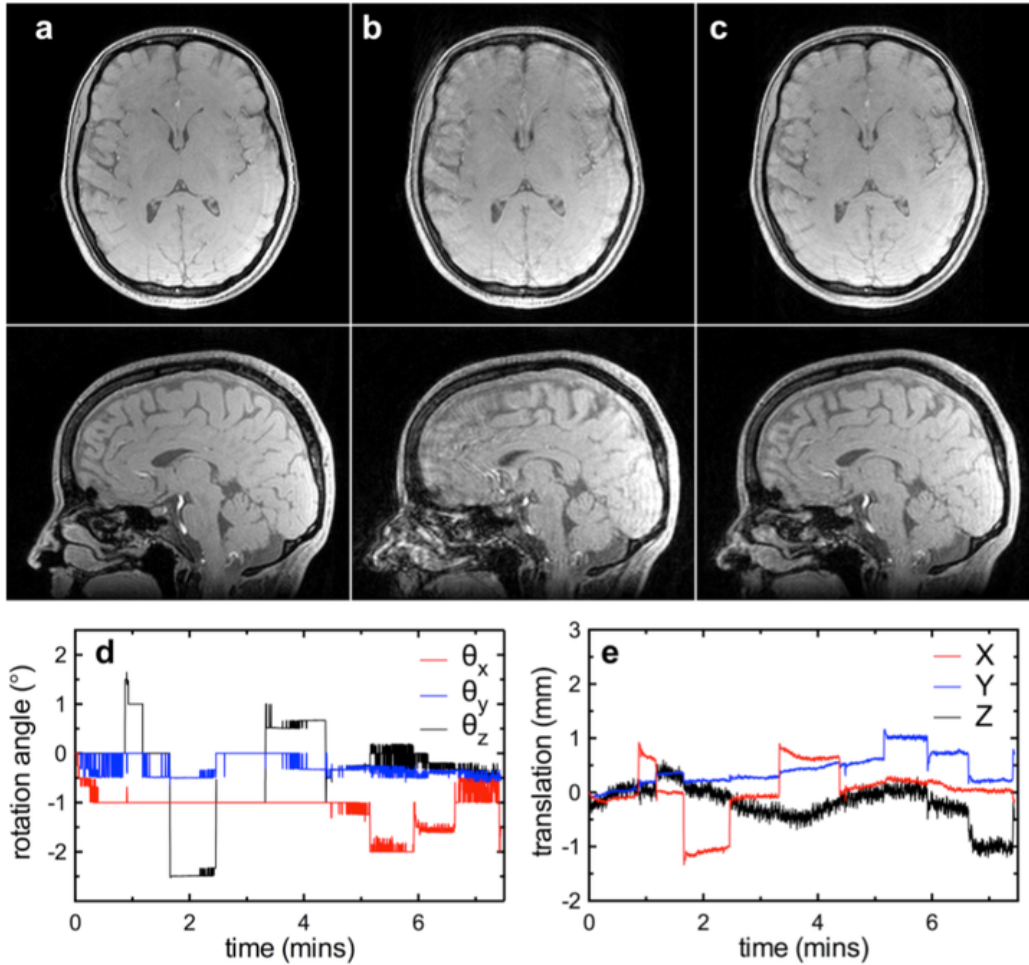


Figure 2-5 Axial and sagittal slices from the 3D reference image acquired with an 8-channel head coil (a) uncorrected image acquired with intended rotation (b) and motion corrected image (c). The measured rotations and translations are shown in (d) and (e).

2.3.5 *Partial SNAV evaluation*

In vivo motion correction was also successfully performed using only an equatorial strip of the SNAV data. Images retrospectively corrected using between 22 (full) and 2 SNAV helical turns are shown in Figure 2-6, along with the reference and uncorrected images. Qualitative evaluation of the images demonstrates excellent correction with partial SNAVs; with a degradation of image quality observed only when fewer than 3 turns (i.e. equatorial strip that reaches up to 0.15 of the SNAV radius) were used. Quantitative assessment, presented as normalized entropy of the 3D images, is

presented in Figure 2-7 for all 6 experiments – three volunteers, two coils – along with the normalized entropy of the uncorrected images. The Figure clearly indicates that for all motions, image quality is improved with increasing number of turns and that the quality does not significantly improve when the number of turns is increased past approximately 8 (corresponding to 0.55 of the SNAV radius).

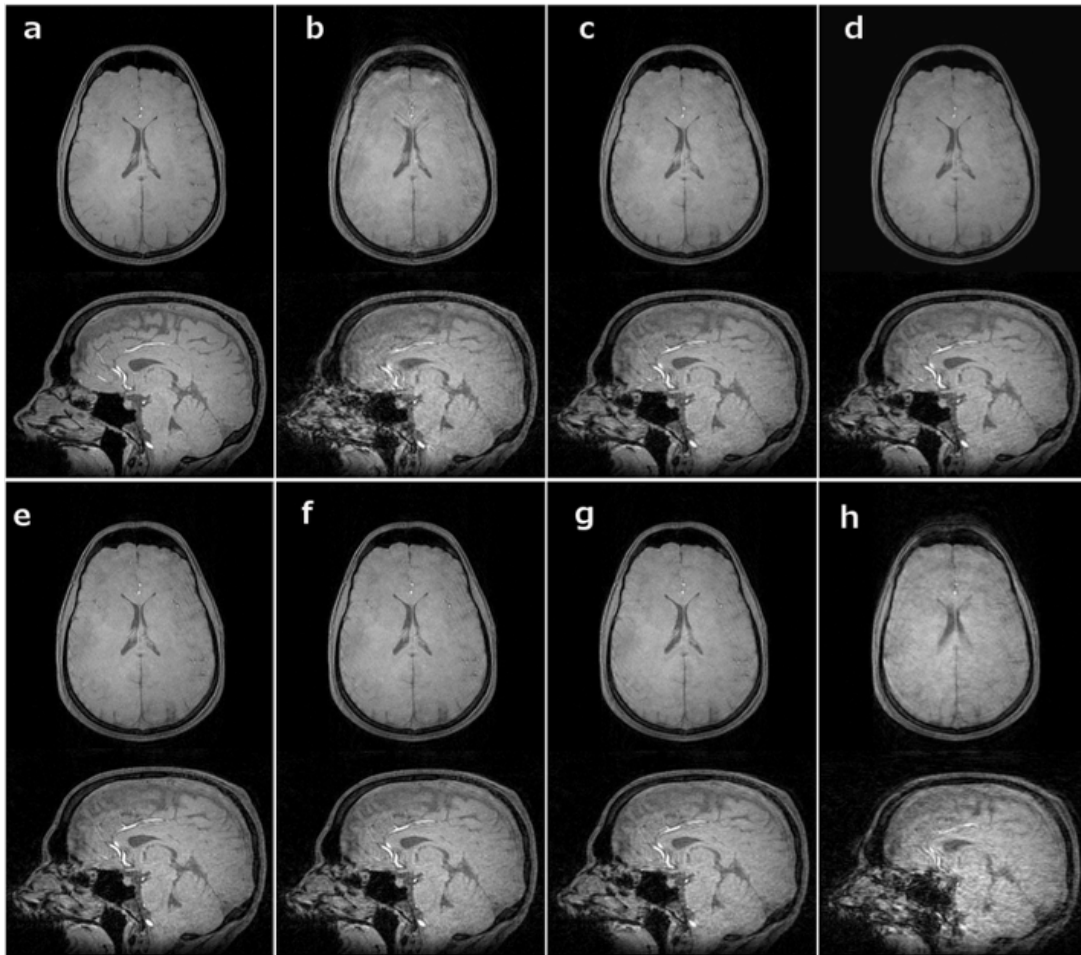


Figure 2-6 Effect of reducing the number of turns of the SNAV. Shown are axial and sagittal slices from a 3D reference image (a), uncorrected motion image (b), and motion-corrected images with 22 (full), 18, 14, 10, 6 and 2 SNAV helical turns in (c-h), respectively.

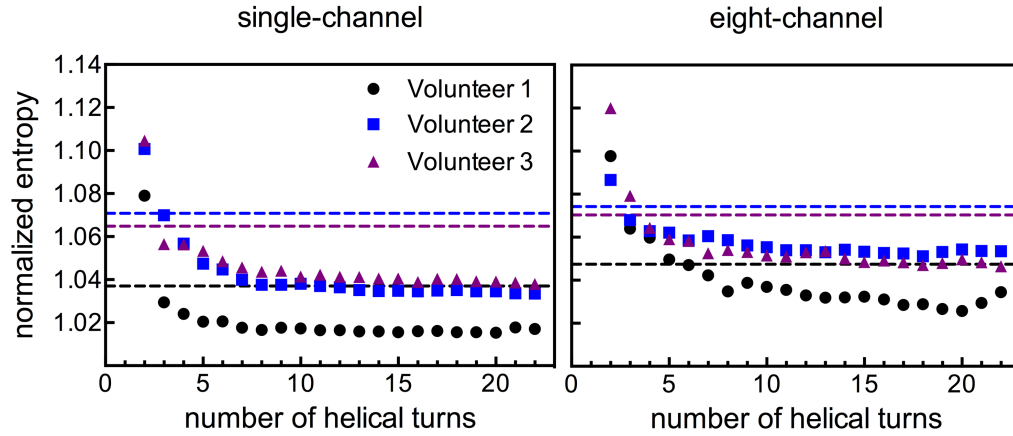


Figure 2-7 Image entropy of each corrected image normalized by the entropy of the associated reference image plotted vs. number of helical turns used for SNAV motion measurements. The horizontal lines indicate the normalized image entropy of the uncorrected images.

2.4 Discussion

This work represents the first application of SNAVs for retrospective motion correction *in vivo*. Retrospective correction was enabled by the combination of two developments – the earlier introduction of the preRot-SNAV template matching technique²⁹ and the current introduction of an accelerated method for acquiring the baseline templates. An assessment of the required number of SNAV helical turns was also performed. Baseline acceleration is achieved by acquiring a limited subset of pre-rotated baseline templates followed by the simulation of templates corresponding to rotation in the Z direction to generate the hybrid baseline. Simulating the third rotation angle reduces the baseline sampling from a 3D- to a 2D- sampling task, which significantly reduces the number of templates acquired without reducing the sampling density of the rotation space. Accurate rotation and translation results were achieved in phantom experiments with as few as 82 acquired templates, corresponding to an acquisition time for the entire baseline template dataset of 2.5 s. Retrospective correction of head motion *in vivo* was

also successful, suppressing motion artefacts in images acquired during head rotations of several degrees and corresponding translations of up to 4 mm.

For a practical implementation of the preRot-SNAV technique we have to limit the rotation range of the acquired baselines so that the templates can be acquired in a reasonable length of time. In this work we used a range of anticipated motion that is sufficient for head imaging ($\pm 6^\circ$ about the X and Y axes). Rotations about the Z axis were simulated, thereby providing latitude for simulating over any range; in the current work a range of $\pm 20^\circ$ was used for consistency with prior work.²⁹ We simulate rotations only about the Z axis because the interpolation of SNAV profiles following rotations along the threads of the spiral SNAV trajectory are far more accurate than interpolations of rotations across the threads, likely due to the T_2^* decay that occurs throughout the SNAV readout. As the phantom (Figure 2-1) results show, the 170-hybrid and 82-hybrid strategies performed comparably. The distribution of angular positions sampled in the baseline can be modified easily and could be optimized for specific applications or a further increase in acquisition speed.

Earlier work²⁹ showed that reduction of the SNAV acquisition time is achieved by acquiring only the equatorial portion of each SNAV. The current study demonstrates that even when using the hybrid template baseline approach, reducing the number of helical turns had little effect on motion measurements. The results suggest there is little benefit to acquiring the entire SNAV and in fact as few as 8 turns are required for consistently successful retrospective correction (Figure 2-7). The benefit of reducing the acquired number of SNAV turns is the reduction in SNAV acquisition time, with a full 22 turn navigator requiring 10 ms per hemisphere to acquire, compared to 5.3 ms for an 8-turn acquisition.

The *in vivo* motion correction results (Figures 2-5) are promising. In all cases, the profiles derived from the SNAV motion measurements agree with the intended motion.

Occasional jitter, of up to 0.4 mm and 0.5 degrees, is seen in the motion profiles. This jitter is likely related to small errors in identification of the minimum of the template-matching cost function and can likely be reduced with further optimization of the matching method. However, jitter of this magnitude did not appear to affect the ability of the hybrid preRot-SNAV to perform retrospective motion correction. Smoothing the motion profiles prior to correction may lead to additional improvement and can be implemented prospectively using Kalman filtering, which has been demonstrated with prior navigator techniques.¹⁷

This proof-of concept work has a few limitations. First, we only demonstrated the insertion of SNAVs into a 3D SPGR sequence. Future work will incorporate SNAV motion correction into other image sequences (e.g. IR-SPGR & EPI). Implementation of SNAVs into 2D sequences is possible but may be more challenging due to a mismatch in image and SNAV excitation volumes; a fat selective SNAV excitation may be required for this task. Second, the current choice of navigator frequency (every 4 image lines) was somewhat arbitrary and further investigation is necessary to determine an optimal frequency given the trade-off between motion detection latency and scan-time; this optimization will likely be application dependent. Third, only retrospective correction has been demonstrated so far.

Prospective motion correction keeps the image coordinate system fixed relative to the object and thus unlike retrospective motion correction avoids gaps in k space that occur due to object rotation. These gaps in k space following rotations are an inherent limitation in retrospective rotation correction. A small rotation range was used for this study in order to minimize these gaps. Prospective correction also preserves the noise statistics, which in retrospective correction A benefit of retrospective correction, however, is that it ensures that the original image is always available. Both methods have advantages and disadvantages; it is likely that the more suitable method will be application dependent. SNAVs are practical for both retrospective and prospective

motion correction if practical issues regarding computation times for motion estimates are resolved.

In order to implement prospective motion correction, further optimization of the SNAV processing code is required to provide additional speedup of the motion measurements. This will be achieved through implementation in C++ (instead of MATLAB) and, if necessary, acceleration using graphical processing units. With an SNAV readout time of ~ 5.3 ms per hemisphere (8 turn SNAV), our goal processing time of 10 ms, and additional time for feedback of motion parameters, the gradient orientation can be updated within 35 ms of the start of SNAV acquisition. This is faster than the current image-based approaches,¹⁵⁻¹⁷ which require, at minimum, 100s of ms for navigator acquisition and processing. It is important to note that, unlike image-based approaches, which have relatively long acquisition times, the presented SNAV approach can be implemented, both prospectively and retrospectively, with rapid gradient echo sequences.

2.5 Conclusions

The presented hybrid baseline SNAV template approach enables the acquisition of a pre-rotated baseline template set in only 2.5 s, followed by template simulation. The 170-hybrid and 82-hybrid sampling strategies performed comparably as did a truncated SNAV with as few as 8 helical turns. This method results in accurate measurements of phantom rotations and translations. *In vivo* motion was measured, and retrospective motion correction was successfully performed.

2.6 References

- 1 Ehman, R. L. & Felmlee, J. P. Adaptive technique for high-definition MR imaging of moving structures. *Radiology* **173**, 255-263,(1989).
- 2 Kramer, M., Herrmann, K. H., Biermann, J. & Reichenbach, J. R. Retrospective reconstruction of cardiac cine images from golden-ratio radial MRI using one-dimensional navigators. *Journal of magnetic resonance imaging : JMRI* **40**, 413-422,(2014).
- 3 Wang, Y., Rossman, P. J., Grimm, R. C., Riederer, S. J. & Ehman, R. L. Navigator-echo-based real-time respiratory gating and triggering for reduction of respiration effects in three-dimensional coronary MR angiography. *Radiology* **198**, 55-60,(1996).
- 4 Fu, Z. W. *et al.* Orbital navigator echoes for motion measurements in magnetic resonance imaging. *Magnetic resonance in medicine* **34**, 746-753,(1995).
- 5 Lin, W. *et al.* Real-time motion correction in two-dimensional multislice imaging with through-plane navigator. *Magnetic resonance in medicine* **71**, 1995-2005,(2014).
- 6 Ward, H. A. *et al.* Prospective multiaxial motion correction for fMRI. *Magnetic resonance in medicine* **43**, 459-469,(2000).
- 7 van der Kouwe, A. J., Benner, T. & Dale, A. M. Real-time rigid body motion correction and shimming using cloverleaf navigators. *Magnetic resonance in medicine* **56**, 1019-1032,(2006).
- 8 Petrie, D. W., Costa, A. F., Takahashi, A., Yen, Y. F. & Drangova, M. Optimizing spherical navigator echoes for three-dimensional rigid-body motion detection. *Magnetic resonance in medicine* **53**, 1080-1087,(2005).
- 9 Welch, E. B., Manduca, A., Grimm, R. C., Ward, H. A. & Jack, C. R., Jr. Spherical navigator echoes for full 3D rigid body motion measurement in MRI. *Magnetic resonance in medicine* **47**, 32-41,(2002).
- 10 Welch, E. B., Manduca, A., Grimm, R. C. & Jack, C. R., Jr. Interscan registration using navigator echoes. *Magnetic resonance in medicine* **52**, 1448-1452,(2004).
- 11 Costa, A. F., Petrie, D. W., Yen, Y. F. & Drangova, M. Using the axis of rotation of polar navigator echoes to rapidly measure 3D rigid-body motion. *Magnetic resonance in medicine* **53**, 150-158,(2005).
- 12 Bonel, H. *et al.* Prospective navigator-echo-based real-time triggering of fetal head movement for the reduction of artifacts. *European radiology* **18**, 822-829,(2008).

- 13 Hirokawa, Y. *et al.* MRI artifact reduction and quality improvement in the upper abdomen with PROPELLER and prospective acquisition correction (PACE) technique. *AJR. American journal of roentgenology* **191**, 1154-1158,(2008).
- 14 Kuperman, J. M. *et al.* Prospective motion correction improves diagnostic utility of pediatric MRI scans. *Pediatric radiology* **41**, 1578-1582,(2011).
- 15 Thesen, S., Heid, O., Mueller, E. & Schad, L. R. Prospective acquisition correction for head motion with image-based tracking for real-time fMRI. *Magnetic resonance in medicine* **44**, 457-465,(2000).
- 16 Tisdall, M. D. *et al.* Volumetric navigators for prospective motion correction and selective reacquisition in neuroanatomical MRI. *Magnetic resonance in medicine* **68**, 389-399,(2012).
- 17 White, N. *et al.* PROMO: Real-time prospective motion correction in MRI using image-based tracking. *Magnetic resonance in medicine* **63**, 91-105,(2010).
- 18 Alhamud, A., Taylor, P. A., van der Kouwe, A. J. & Meintjes, E. M. Real-time measurement and correction of both B0 changes and subject motion in diffusion tensor imaging using a double volumetric navigated (DvNav) sequence. *NeuroImage* **126**, 60-71,(2015).
- 19 Dylan Tisdall, M. *et al.* Prospective motion correction with volumetric navigators (vNavs) reduces the bias and variance in brain morphometry induced by subject motion. *NeuroImage*,(2015).
- 20 Engstrom, M., Martensson, M., Avventi, E., Norbeck, O. & Skare, S. Collapsed fat navigators for brain 3D rigid body motion. *Magnetic resonance imaging* **33**, 984-991,(2015).
- 21 Gallichan, D., Marques, J. P. & Gruetter, R. Retrospective correction of involuntary microscopic head movement using highly accelerated fat image navigators (3D FatNavs) at 7T. *Magnetic resonance in medicine* **75**, 1030-1039,(2015).
- 22 Skare, S., Hartwig, A., Martensson, M., Avventi, E. & Engstrom, M. Properties of a 2D fat navigator for prospective image domain correction of nodding motion in brain MRI. *Magnetic resonance in medicine* **73**, 1110-1119,(2015).
- 23 Callaghan, M. F. *et al.* An evaluation of prospective motion correction (PMC) for high resolution quantitative MRI. *Frontiers in neuroscience* **9**, 97,(2015).
- 24 Qin, L. *et al.* Prospective head-movement correction for high-resolution MRI using an in-bore optical tracking system. *Magnetic resonance in medicine* **62**, 924-934,(2009).

- 25 Schulz, J. *et al.* An embedded optical tracking system for motion-corrected magnetic resonance imaging at 7T. *Magma (New York, N.Y.)* **25**, 443-453,(2012).
- 26 Zaitsev, M., Dold, C., Sakas, G., Hennig, J. & Speck, O. Magnetic resonance imaging of freely moving objects: prospective real-time motion correction using an external optical motion tracking system. *NeuroImage* **31**, 1038-1050,(2006).
- 27 Todd, N., Josephs, O., Callaghan, M. F., Lutti, A. & Weiskopf, N. Prospective motion correction of 3D echo-planar imaging data for functional MRI using optical tracking. *NeuroImage* **113**, 1-12,(2015).
- 28 Stucht, D. *et al.* Highest Resolution In Vivo Human Brain MRI Using Prospective Motion Correction. *PloS one* **10**, e0133921,(2015).
- 29 Liu, J. & Drangova, M. Rapid six-degree-of-freedom motion detection using prerotated baseline spherical navigator echoes. *Magnetic resonance in medicine* **65**, 506-514,(2011).
- 30 Liu, J. & Drangova, M. Phase-unwrapping algorithm for translation extraction from spherical navigator echoes. *Magnetic resonance in medicine* **63**, 510-516,(2010).
- 31 Tavallaei, M. A., Johnson, P. M., Liu, J. & Drangova, M. Design and evaluation of an MRI-compatible linear motion stage. *Medical Physics* **43**, 62,(2016).
- 32 Tisdall, M. D. Prospective head motion correction in 3D FLASH using EPI-based volumetric navigators. *Proc Intl Soc Mag Reson Med* **22:0882**.
- 33 Fessler, J. A. & Sutton, B. P. Nonuniform Fast Fourier Transforms Using Min-Max Interpolation. *IEEE Transactions on signal processing* **51**, 560-574,(2003).
- 34 Liu, J. & Drangova, M. Combination of multidimensional navigator echoes data from multielement RF coil. *Magnetic resonance in medicine* **64**, 1208-1214,(2010).
- 35 Aksoy, M. *et al.* Hybrid prospective and retrospective head motion correction to mitigate cross-calibration errors. *Magnetic resonance in medicine* **67**, 1237-1251,(2012).
- 36 Loktyushin, A., Nickisch, H., Pohmann, R. & Scholkopf, B. Blind retrospective motion correction of MR images. *Magnetic resonance in medicine* **70**, 1608-1618,(2013).

3 Rigid-body motion correction in hybrid PET/MRI using spherical navigator echoes

3.1 *Introduction*

Integrated positron emission tomography and magnetic resonance imaging (PET/MRI) is a promising hybrid imaging modality that can provide simultaneous functional and anatomic information. For neuroimaging, PET/MRI is especially promising for imaging in oncology,¹ focal epilepsy² and neurodegenerative disorders.³ However, both PET and MRI are highly susceptible to patient motion due to long acquisition times.

In PET exams, blurring and artefacts from motion can hinder the detection and delineation of lesions and the accurate quantification of radiotracer uptake. If a PET image is deemed non-diagnostic, it may be reacquired, however this results in an image with lower count statistics if reacquired right away, or increased radiation exposure if reacquired at a later date following additional administration of tracer. Motion during MRI acquisition also causes substantial blurring and artefacts that can severely degrade the diagnostic quality of the images. A study by Andre *et al.*, found that in their institution, nearly 20% of MRI exams required at least one sequence be repeated due to motion; they estimated that these repeated scans are associated with a cost of \$115,000 per scanner per year, as well as delayed diagnosis for some patients.⁴

While head restraints are effective at reducing head movement during PET and MRI exams, they do not completely eliminate it. A simple motion correction technique for PET, consists of dividing the acquisition into multiple acquisition frames (MAF).⁵ These image frames are then spatially registered and summed to create a single volume. When this technique is applied, without knowledge of the motion, a trade off exists between high-temporal-resolution motion correction, which yields low count statistics resulting in high noise propagation⁶ and potential bias in the final image,^{7,8} and low-temporal-resolution motion correction with potentially high intra-frame motion.

Knowledge of motion parameters during a scan greatly improves the MAF method by informing the binning of the data.

External tracking of head motion – typically using an external camera and markers attached to the head – has been successful for motion measurement in both PET⁹ and MRI.¹⁰⁻¹² A limitation of this technology is the tradeoff between effective rigid coupling of the marker to the head, and patient comfort. Additionally, achieving sufficient line-of-sight between the camera system and the markers is non-trivial due to scanner geometry, and is further confounded by the requirement for MRI compatibility. Over the past two decades, significant advances have been made in MRI based techniques for motion correction in MR brain imaging. Active markers^{13,14} and MRI navigators in both image space¹⁵⁻¹⁷ and k space^{18,19} have all proved to be successful tools for rigid-body motion correction. Simultaneous acquisition of PET and MR images with a hybrid PET/MRI scanner allows for these MRI motion correction techniques to be applied to both the MRI and PET acquisitions.

Development of MRI based motion correction tools in PET/MRI has largely focused on cardiac imaging where the quasi-periodic and predictable motion of the heart and chest wall allows the use of gating and motion models.²⁰⁻²² While successful at respiratory motion correction, these techniques are not suitable for the spontaneous and unpredictable motion that can occur during head imaging. Previous studies which have successfully developed MRI based motion correction techniques for brain PET using navigators,²³ image registration^{24,25} and active markers^{26,27} used the MRI solely for motion correction and did not acquire diagnostic MRI images simultaneously with the PET.

In this work spherical navigator echoes (SNAVs) – 3D k-space navigators capable of tracking motion in six degrees of freedom²⁸⁻³⁰ – are interleaved within a three dimensional turbo FLASH (tfl) pulse sequence to enable simultaneous motion

corrected PET and MRI. The SNAV technique can measure brain rotations and translations with sub-millimeter and sub-degree accuracy and has previously been applied successfully for retrospective correction of MR brain images.¹⁹ In this work we demonstrate successful retrospective motion correction of simultaneously acquired PET and MR images of an anthropomorphic brain phantom.³¹

3.2 *Methods*

We first describe the SNAV motion correction approach and follow with a description of the navigated pulse sequence, before demonstrating retrospective motion correction of simultaneously acquired PET and MR images. All experiments were performed on a Siemens Biograph mMR – a 3T hybrid PET/MRI scanner – with a 12-channel receive head coil. The Research Ethics Board at our institution approved the human-subject study and informed consent was obtained from the volunteer.

3.2.1 *SNAV motion correction*

Spherical navigators which were described in detail in chapter 2, are 3D navigators that sample a spherical shell in k space. They are acquired with two RF excitations – one for each hemisphere – that spiral from the equator to opposite poles. For each hemisphere, 800 points were acquired with a sampling time of 10 μ s. The flip angle was 8°, the TR was 20 ms and the radius of the SNAV was 0.4 cm⁻¹. An example SNAV magnitude profile is shown in Figure 3-1a.

For rapid motion correction, the SNAV method begins by acquiring a baseline scan of 170 pre-rotated SNAV templates to be used as a look-up table. Baseline templates, pre-rotated about the left-right and anterior-posterior axes are acquired, and templates corresponding to rotations about the superior-inferior axis are simulated. Rotation angles between an unknown physically transformed position and the baseline position are determined by identifying the pre-rotated SNAV templates with the lowest sum of

squared differences relative to the SNAVs acquired at the transformed position. Translations are then calculated from the phase difference between the best-matched template and the SNAV acquired at the transformed position. A detailed description of this method can be found in chapter 2 and Johnson *et al.* 2016.¹⁹

3.2.2 *Navigated pulse sequence implementation*

For retrospective motion correction, SNAVs were incorporated into the Siemens turbo FLASH (tfl) sequence – a fast gradient echo sequence with inversion recovery (IR) magnetization preparation; we will refer to this as the tfl-SNAV pulse sequence. The 170 pre-rotated baseline SNAVs are acquired in 6.8 s at the beginning of the tfl-SNAV scan. Subsequently, interleaved SNAVs are acquired during the dead time immediately prior to each IR preparation pulse and are preceded by eight steady state pulses to ensure consistency with the pre-rotated SNAVs. The SNAVs are inserted in the phase encode loop of the sequence; they are acquired once per TR and prior to the acquisition of a single line of k space for each of 80 slices. A simplified timing diagram of the sequence is shown in Figure 3-1b.

In order to verify that the insertion of the navigators does not have a detrimental effect on image quality when compared to the original tfl sequence, we acquired and compared two brain images from a healthy volunteer instructed to remain still: the first was acquired with the product tfl sequence and the second with the tfl-SNAV sequence. The image acquisition parameters for both scans were as follows: TE/TR = 2.4 ms/2.2 s, inversion time = 800 ms, image bandwidth = 240 Hz/pixel, flip angle = 8°. The images were acquired with an asymmetric echo, matrix size = 152x192x80 (192x192x80 reconstructed), resolution = 1 mm in plane, slice thickness = 2 mm. The scan plane was axial and the readout direction was anterior-posterior. The motion measured during the tfl-SNAV scan was then used to correct the tfl-SNAV image in

order to demonstrate that the retrospective correction procedure does not introduce artefacts.

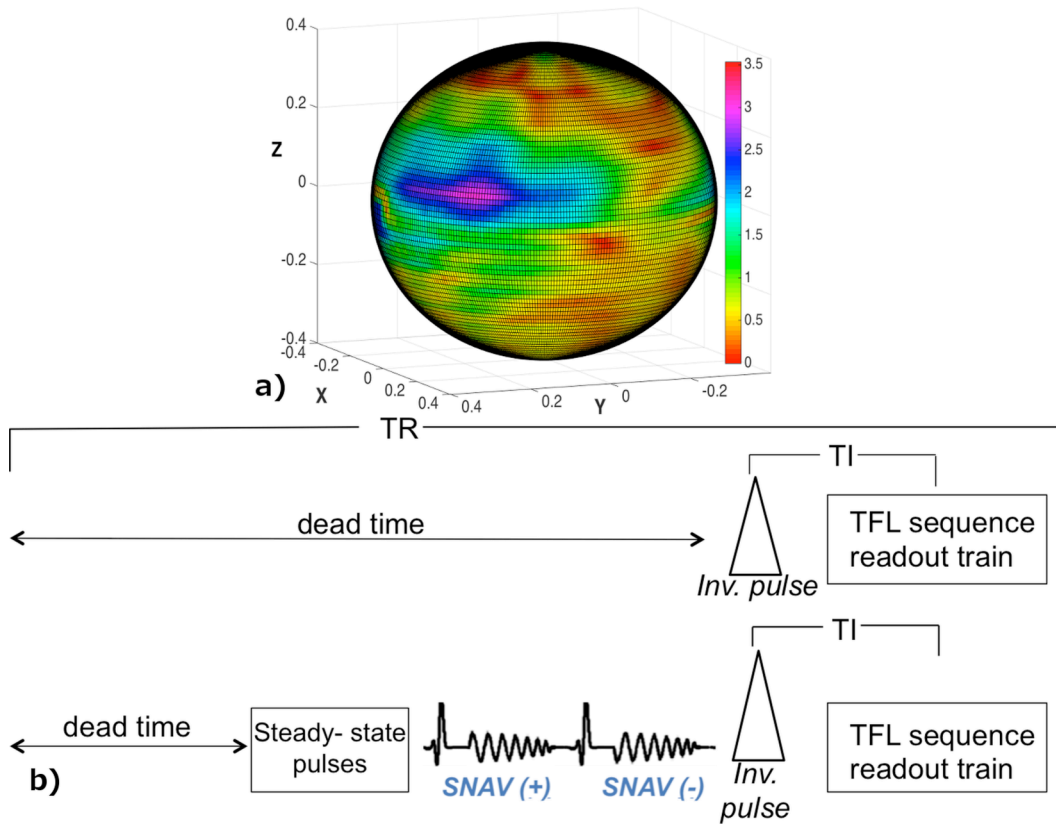


Figure 3-1 An example SNAV magnitude profile – displayed in arbitrary units – is illustrated in (a). The SNAV has a total of 1600 data points sampled on a spherical shell with radius 0.4 cm^{-1} . A simplified timing diagram illustrates the turbo-FLASH (tfl) and tfl-SNAV pulse sequences (b). A single TR for each sequence is shown. Both sequences have a 180° inversion pulse followed by a readout train with 80 echoes. The SNAV is inserted in the phase encode loop, prior to the inversion pulse and during the dead time of the original tfl sequence, which is then followed by the tfl sequence readout train.

3.2.3 Motion experiments

The phantom used in this experiment was an anthropomorphic brain phantom developed by Iida *et al.*³¹ The phantom was developed as a tool to evaluate image reconstruction techniques for PET and SPECT imaging. The 3D printed phantom, which has dimensions $23.7 \text{ cm} \times 15.2 \text{ cm} \times 19.3 \text{ cm}$, was designed with two

compartments: bone and grey matter. The bone compartment was filled with 323 mL of a bone equivalent solution (K_2HPO_4) that has been demonstrated to mimic bone in PET images.³¹ The grey matter compartment was filled with 564 mL of an FDG doped solution; the activity of the solution was approximately 40 MBq. A plastic rod and plate were affixed to the neck of the head phantom using mounting tape; this allowed for manual repositioning of the phantom during the scan. The tfl-SNAV acquisition was repeated four times; the first acquisition was a stationary 7-minute reference image, this was followed by three 7-minute scans where the phantom was manually repositioned several times throughout each scan. The acquisition parameters for all phantom MRI scans were identical to the parameters used for the *in vivo* scan described in the previous section, with the exception of the IR prep time which was reduced to 300 ms, as it was empirically determined to give superior image quality for the phantom. Each MRI acquisition was accompanied by a simultaneous FDG PET list-mode acquisition.

3.2.4 *Motion measurement and correction*

SNAVs were processed in MATLAB (Math Works, Natick, MA); the rotations and translations were determined by comparing SNAVs acquired during the PET/MRI scan to those acquired in the baseline scan. A weighted average rotation angle was calculated from the templates with a cost function value falling within 10% of the lowest calculated cost. Translations are calculated from the phase difference between the best-matched template and the measurement SNAVs. The SNAV motion estimates were then used to correct the MRI data by rotating and phase shifting the data back to the baseline reference frame. A detailed description of this method can be found in Johnson *et al.* 2016.

The measured motion profile was then used to sort the list-mode data into multiple acquisition frames defined by the individual motion states. The reconstruct, transform, add (RTA) reconstruction⁵ was then performed in which each bin was reconstructed

with a matrix size of 344x344x127 and pixel dimension 2.09 mm x 2.09 mm x 2.03 mm. The iterative three-dimensional reconstruction algorithm: *Ordinary poisson-ordered subset expectation maximization* (OP-OSEM) (3 iterations, 24 subsets, 5 mm FWHM Gaussian filter) was used with MRI Dixon-based attenuation correction. The attenuation correction data was aligned to each motion state prior to reconstruction and attenuation correction. The reconstruction of each bin was performed using e7-tools – the Siemens reconstruction toolbox. Finally, the PET images corresponding to each bin were transformed based on the measured motion and summed to form the motion-corrected PET image. A flowchart of the entire procedure, from the acquisition of image and SNAV data, to motion correction of PET and MR images is illustrated in Figure 3-2.

Prior to qualitative and quantitative analysis, the motion-corrupted and corrected images were registered to the reference images. For qualitative analysis, difference images were calculated for both the PET and MR images for each trial, where the motion corrupted and corrected images were subtracted from the corresponding stationary reference image. All images were scaled from 0 to 1 prior to the calculation of the difference images.

3.2.5 *Quantitative evaluation of image quality*

In order to evaluate the effect of motion and subsequent correction on the quantitative values of the image, line profiles were measured through the motion-corrupted, corrected and reference images. To quantify the improvement in PET and MR image quality for the entire volume, the motion-corrupted and corrected volumes were compared to the reference image using two image quality measures commonly used in image analysis: peak signal-to-noise ratio (PSNR) and structural similarity index (SSIM).³² PSNR, which approaches infinity as the numerical difference between the

images approaches zero, is very sensitive to numerical differences between images and is considered to be an objective measure of image quality.³³ PSNR was calculated as:

$$PSNR = 10 \cdot \log_{10} \left(\frac{MAX_I}{MSE} \right), \quad (3.1)$$

where MAX_I is the maximum possible value of the image and MSE is the mean squared error between the two images. SSIM approaches one as the difference between the images approaches zero, and is considered to be correlated with perceptual image quality of the human visual system.³³ SSIM was calculated with the following equation.³⁴

$$SSIM(x, y) = \frac{(2\mu_x\mu_y + C_1)(2\sigma_x\sigma_y + C_2)}{(\mu_x^2 + \mu_y^2 + C_1)(\sigma_x^2 + \sigma_y^2 + C_2)}, \quad (3.2)$$

where μ_x and μ_y are the mean intensities of images x (distorted) and y (reference) and σ_x and σ_y are the standard deviations of images x and y. C_1 and C_2 are constants given by:

$$C_1 = (K_1 L)^2, \quad (3.3)$$

where L is the dynamic range of the images and K_1 and K_2 are small non-zero values that stabilize the division of the denominator. These values were set to $C_1=0.01$ and $C_2=0.03$.³⁴ For the three motion trials, both the motion-corrupted and corrected images were registered to the reference image before PSNR and SSIM were calculated.

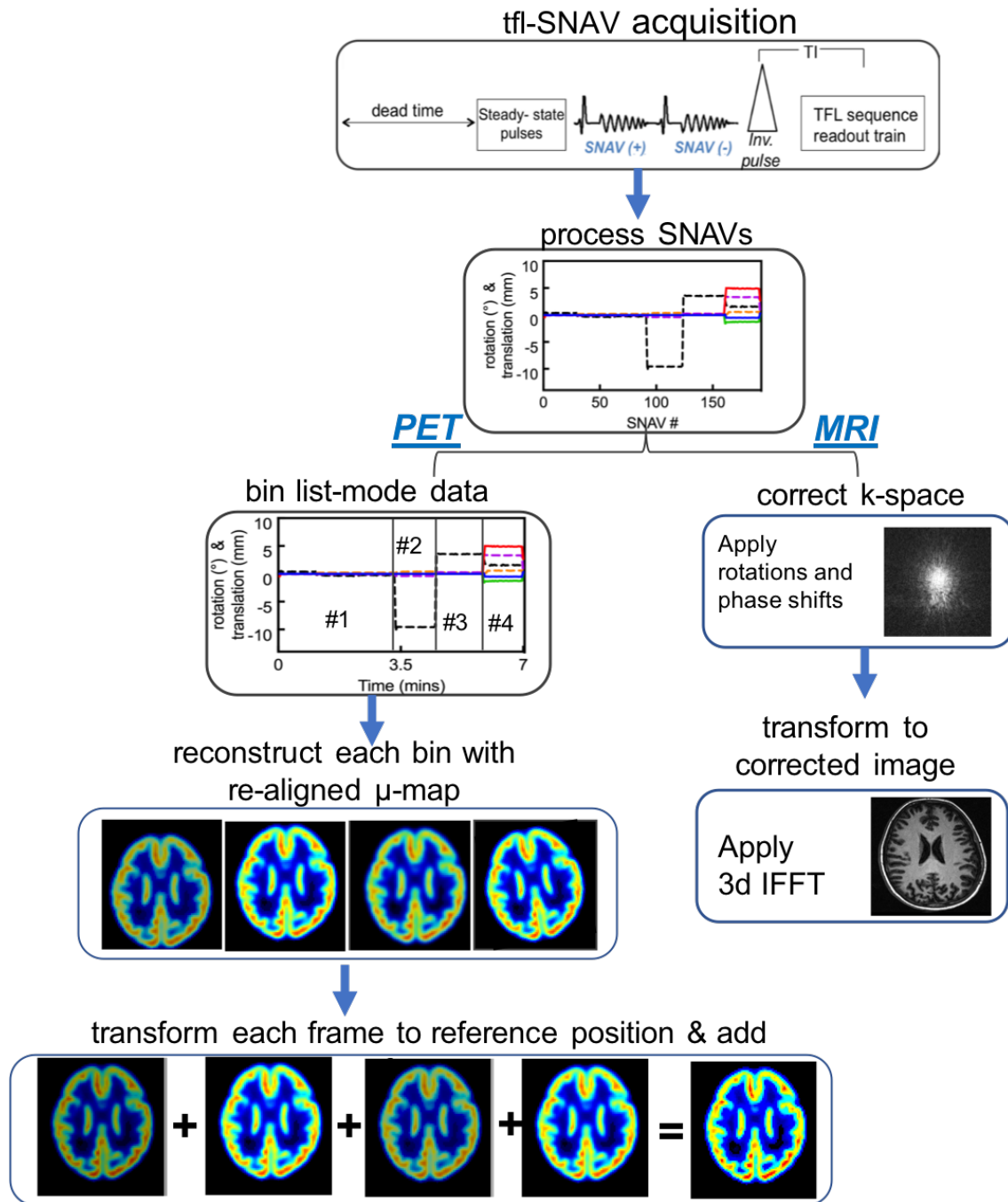


Figure 3-2 Flow chart of the SNAV motion correction technique from the acquisition of tfl-snav to the motion correction of the PET and MR image data

3.3 Results

3.3.1 *tfl-SNAV pulse sequence*

Four axial slices of the *in vivo* images acquired using the product tfl and tfl-SNAV sequences are shown in Figure 3-3a and 3-3b respectively. The same four slices of the motion corrected tfl-SNAV image are shown in Figure 3-3c. The motion profile, measured by the SNAVs, and used to correct the tfl-SNAV image data is shown in Figure 3-3d. The slow drift in Z translation is a common occurrence in *in vivo* brain imaging and is attributed to involuntary relaxation of neck muscles. As expected, there are no apparent differences in the image quality caused by the addition of the SNAVs or motion correction.

3.3.2 *Motion measurement and correction*

The three measured motion profiles along with the motion frames defined for the PET reconstruction are shown in Figure 3-4. The maximum rotations were 5°, 11°, and 5° and the maximum translations were 11 mm, 8 mm and 14 mm for the first, second and third motion trials respectively. The PET list-mode data, for motion trials 1, 2 and 3, were binned into 4, 5 and 5 motion frames respectively. The duration of these frames ranged from 45 seconds to 3.5 minutes. The motion frames were defined based on the measured motion profiles (Figure 3-4). If motion greater than 1 degree or 2 mm was measured then a new frame was started. We chose to apply motion such that the motion frames would have highly variable lengths in order to reflect the sporadic and unpredictable nature of *in vivo* head motion.

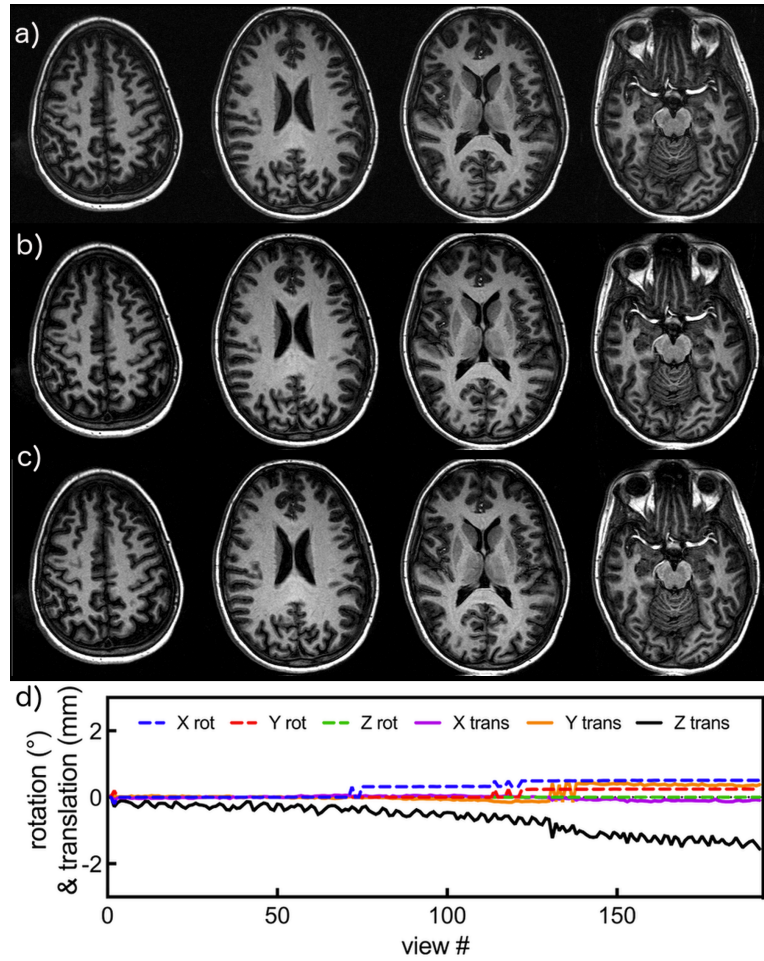


Figure 3-3 Axial slices of the product tfl (a), tfl-SNAV (b) and motion corrected tfl (c). The motion profile measured during the tfl-SNAV sequence (d) was used for the motion correction.

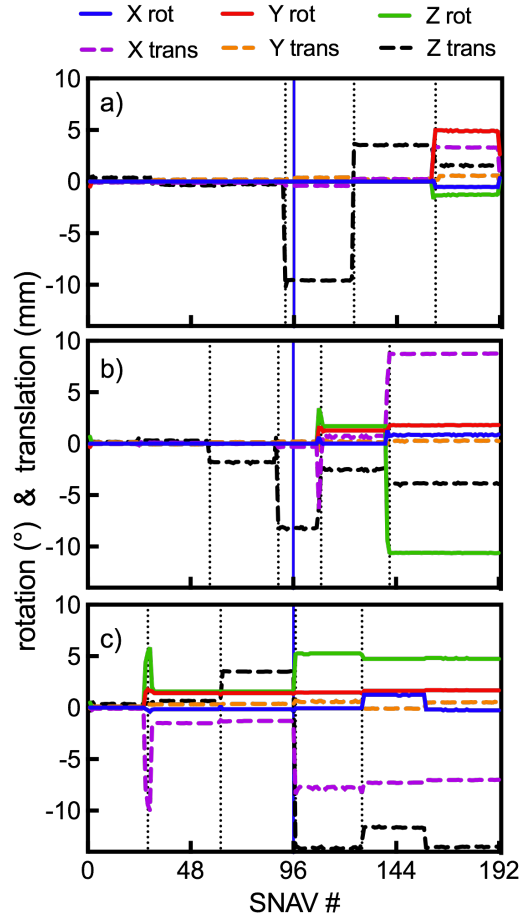


Figure 3-4 Rotations and translations measured by the SNAVs in trials 1 (a), 2 (b) and 3 (c). The vertical dotted lines indicate the temporal bins used for RTA reconstruction. The vertical blue line indicates the center line of k space.

Motion correction was achieved for both the PET and MR images. Motion correction of the PET images successfully reduced motion blurring and motion correction of the MR images resulted in significant artefact suppression and reduced blurring. Motion correction results for both the PET and MR images from all three motion trials are shown in Figure 3-5; single representative slices of the motion-corrupted, corrected, and reference images are shown, along with the calculated difference images. In trial 1 (Figure 3-5a), which had the least motion, the three PET images are qualitatively quite similar. However, the motion artefacts, and motion correction in the MR images for this example are substantial. In trial 2 (Figure 3-5b), both the PET and MRI motion

correction resulted in significant image quality improvement. In trial 3 (Figure 3-5c), which had the most motion, motion correction of the PET and MR images resulted in improved image quality; however, some blurring remained in the motion-corrected MR image.

3.3.3 *Quantitative evaluation of motion correction*

Line profiles measured through the horizontal line indicated in Figure 3-5 by the white lines are plotted in Figure 3-6. For all 6 images sets larger quantitative errors in the motion-corrupted images than in the corrected images are observed. Additionally, the agreement between the corrected and motion-corrupted images and the reference image is quantified using PSNR and SSIM (Figure 3-7). For each motion trial, PSNR and SSIM are higher for the corrected images than the motion-corrupted images, indicating that the corrected images are in better agreement with the reference image.

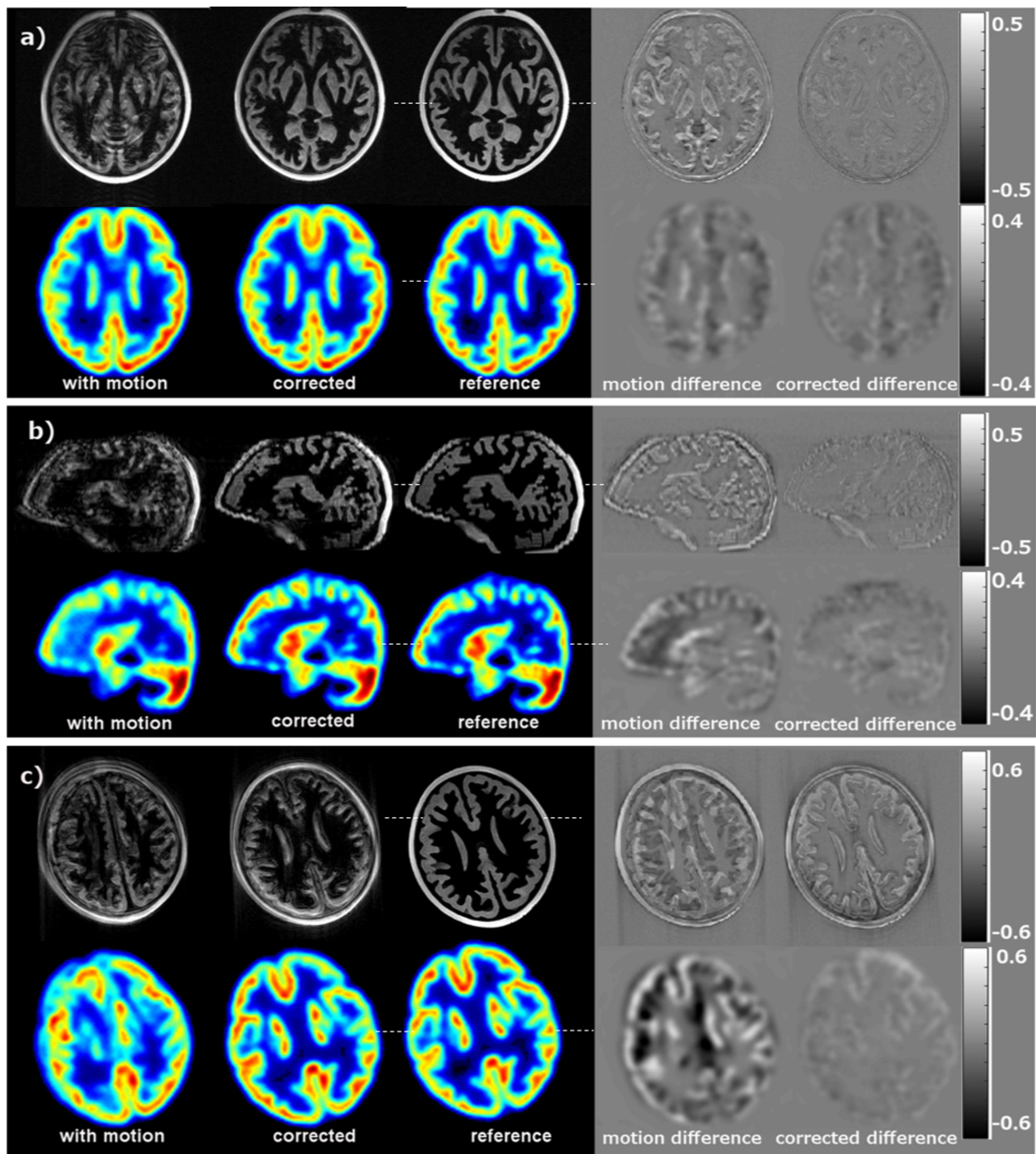


Figure 3-5 SNAV motion correction results. A single slice of the motion-corrupted, corrected and reference PET and MR images are shown for each trial. The difference images are shown in the fourth and fifth columns. The colour bars show the range of pixel intensities in the difference images (original images were scaled from 0 to 1). Motion correction was achieved in trial 1 (a), trial 2 (b) and trial 3 (c). The white lines in the reference image indicate the location of the measured line profiles displayed in Figure 3-6.

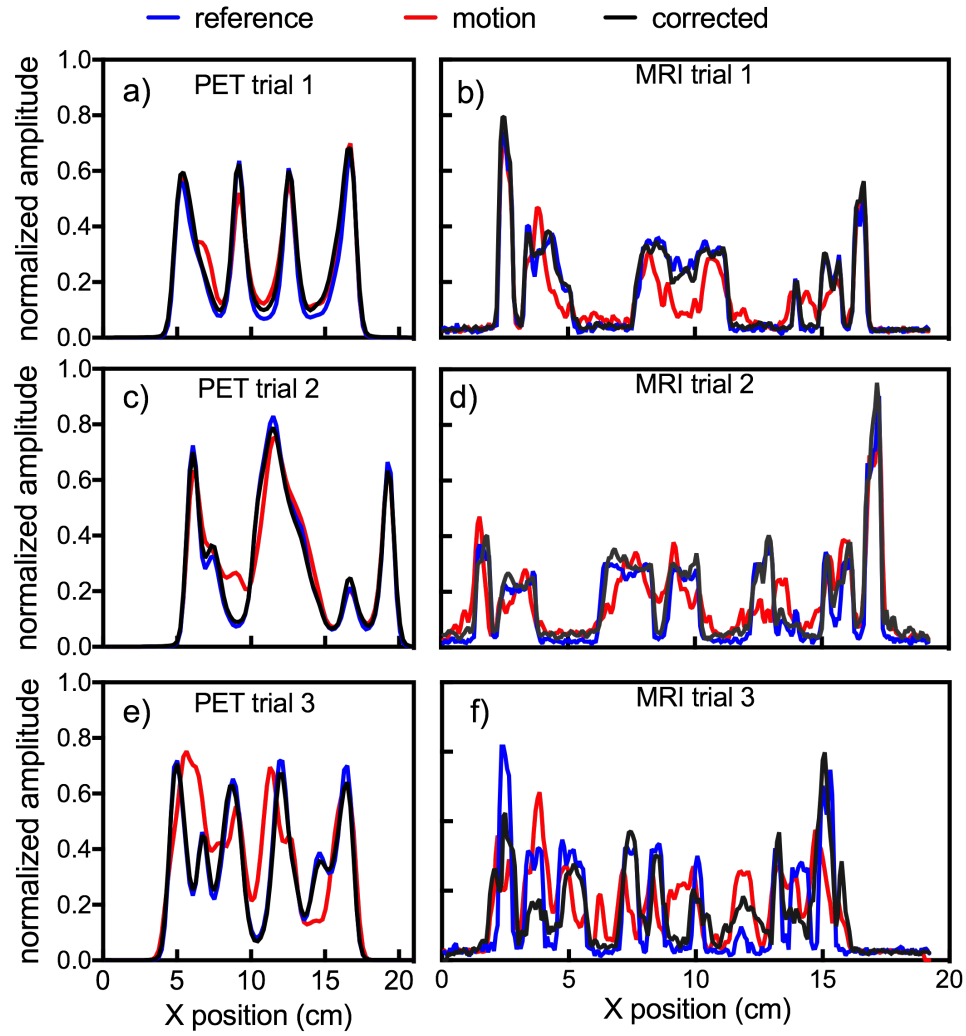


Figure 3-6 Line profiles calculated along a horizontal line (left-right) for trials 1 (a & b), 2 (c & d) and 3 (e & f). The location of each line is shown in Figure 3-5 as white dotted lines; the line profile was measured in the same plane as the displayed images.

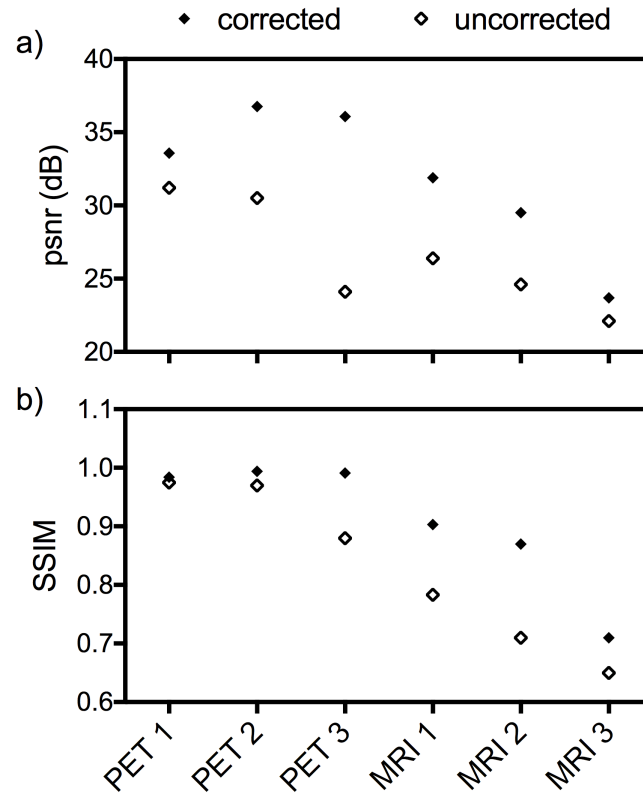


Figure 3-7 Peak signal to noise ratio (top) and structural similarity index (bottom) calculated for PET and MR images from trials 1, 2 and 3.

3.4 Discussion

This work represents the first application of MRI navigators for three-dimensional motion correction of simultaneously acquired PET and MR brain images. Rotations up to 11° and translations up to 14 mm, relative to baseline, were measured by the SNAVs and retrospective motion correction based on these measurements successfully removed motion artefacts from both the MR and PET images of an anthropomorphic brain phantom. The motion corrected PET images were in better agreement with the reference, as measured by PSNR and SSIM. Similarly, artefact suppression and reduction in motion blurring were observed in all MR images as well.

The results suggest that the SNAVs are able to accurately measure head motion, and their insertion into the product image sequence does not have a negative impact on the image quality. This makes SNAVs a promising tool for a range of pulse sequences and applications. While they have only been incorporated into the tfl sequence in this work (and SPGR in prior work), the modular implementation as a sequence building block will allow SNAVs to be added to other sequences with only minor modifications to the host sequence source code. Additionally, as the SNAVs can be acquired very rapidly (15 ms minimum TR) incorporating them seamlessly into pulse sequences may be less challenging than incorporating image-space navigators, which take hundreds of milliseconds to acquire. The motion corrected PET reconstruction would take very little additional time compared to the standard reconstruction, provided that the frames are reconstructed in parallel. In this work, SNAVs have been used to correct for sudden motion, because it is more challenging, and is more detrimental to MR image quality than slow continuous motion. Slow continuous motion does often occur *in vivo* (Figure 2), and can be corrected using the same technique. Motion bins could be defined to limit the intra-bin continuous motion to be below some chosen threshold.

Previous studies that have used MRI based approaches for motion correction in hybrid PET/MRI of the brain were also successful in correcting the PET data.^{23-25,27} These applications however used the MRI solely for the purposes of motion correction and did not acquire any diagnostic MR images. By interleaving the SNAVs into a diagnostic image sequence we were able to acquire motion data along with both MR and PET images, thereby fully exploiting the potential of the hybrid imaging modality.

In the third motion trial, some blurring remained in the motion corrected MR image, however this was an example of extreme motion, as there was a very large translation (14 mm), which occurred during the acquisition of the center k-space lines. Additionally, in this study, the MRI motion correction was applied retrospectively rather than prospectively. Prospective motion correction, which has been demonstrated

in many other studies,^{13,15,35} eliminates the need to interpolate MRI data that falls off the Cartesian grid due to rotations. As such, retrospective correction may be less effective at correcting large rotations. It does however have the benefit of retaining the original uncorrected data, which is not possible with prospective motion correction. We are currently working towards a prospective implementation, which will allow us to compare the efficacy of the two approaches.

A limitation of the SNAV implementation used for this work is the low temporal resolution of the motion estimates, which is equivalent to the image TR (2.2s). Motion that occurs within a TR cannot be corrected and may be a source of residual artefacts in the MR images. Additionally, the MRI data collected for the attenuation correction was not motion corrected; if a patient moves during this 19s sequence, it may cause errors in attenuation correction of the PET data. Motion correction was demonstrated with a phantom, and although the phantom is modeled from a human brain, it cannot model all of the complexities of *in vivo* imaging. It does however allow us to evaluate motion correction in a controlled environment and avoid giving unnecessary radiation dose to human subjects.

PET/MRI is an exciting tool for exploring neurological diseases. Hybrid PET/MRI imaging is exploited for numerous neurological diseases, including epilepsy, neuropsychiatry and chronic pain. These exams are often lengthy, and patient motion is a common problem. With effective motion correction strategies, the utility of this exciting modality can be greatly improved thereby furthering our understanding of brain function, perfusion and metabolism.

3.5 Conclusion

The presented SNAV motion correction for hybrid PET/MRI approach enables the retrospective correction of simultaneously acquired PET and MR images. This method consistently results in reduced motion artefacts and motion blurring.

3.6 References

- 1 Oehlke, O. & Grosu, A.-L. PET/MRI and brain tumors: focus on radiation oncology treatment planning. *Clinical and Translational Imaging* **5**, 159-167,(2017).
- 2 Paldino, M. J. *et al.* Comparison of the diagnostic accuracy of PET/MRI to PET/CT-acquired FDG brain exams for seizure focus detection: a prospective study. *Pediatric radiology* **47**, 1500-1507,(2017).
- 3 Barthel, H., Schroeter, M. L., Hoffmann, K. T. & Sabri, O. PET/MR in dementia and other neurodegenerative diseases. *Seminars in nuclear medicine* **45**, 224-233,(2015).
- 4 Andre, J. B. *et al.* Toward Quantifying the Prevalence, Severity, and Cost Associated With Patient Motion During Clinical MR Examinations. *Journal of the American College of Radiology : JACR* **12**, 689-695,(2015).
- 5 Picard, Y. & Thompson, C. J. Motion correction of PET images using multiple acquisition frames. *IEEE transactions on medical imaging* **16**, 137-144,(1997).
- 6 Karakatsanis, N. A., Tsoumpas, C. & Zaidi, H. Quantitative PET image reconstruction employing nested expectation-maximization deconvolution for motion compensation. *Computerized medical imaging and graphics : the official journal of the Computerized Medical Imaging Society* **60**, 11-21,(2017).
- 7 Polycarpou, I., Tsoumpas, C. & Marsden, P. K. Analysis and comparison of two methods for motion correction in PET imaging. *Medical Physics* **39**, 6474-6483,(2012).
- 8 Reilhac, A. *et al.* Simulation-based evaluation of OSEM iterative reconstruction methods in dynamic brain PET studies. *NeuroImage* **39**, 359-368,(2008).
- 9 Bloomfield, P. M. *et al.* The design and implementation of a motion correction scheme for neurological PET. *Physics in medicine and biology* **48**, 959-978,(2003).
- 10 Maclaren, J., Aksoy, M., Ooi, M. B., Zahneisen, B. & Bammer, R. Prospective motion correction using coil-mounted cameras: Cross-calibration considerations. *Magnetic resonance in medicine* **79**, 1911-1921,(2018).
- 11 Mattern, H. *et al.* Prospective motion correction enables highest resolution time-of-flight angiography at 7T. *Magnetic resonance in medicine* **80**, 248-258,(2018).
- 12 Stucht, D. *et al.* Highest Resolution In Vivo Human Brain MRI Using Prospective Motion Correction. *PloS one* **10**, e0133921,(2015).

- 13 Ooi, M. B., Krueger, S., Thomas, W. J., Swaminathan, S. V. & Brown, T. R. Prospective Real-Time Correction for Arbitrary Head Motion Using Active Markers. *Magnetic resonance in medicine* **62**, 943-954,(2009).
- 14 Ooi, M. B., Krueger, S., Muraskin, J., Thomas, W. J. & Brown, T. R. “Echo-Planar Imaging with Prospective Slice-by-Slice Motion Correction using Active Markers”. *Magnetic resonance in medicine* **66**, 73-81,(2011).
- 15 Tisdall, M. D. *et al.* Volumetric navigators for prospective motion correction and selective reacquisition in neuroanatomical MRI. *Magnetic resonance in medicine* **68**, 389-399,(2012).
- 16 White, N. *et al.* PROMO: Real-time prospective motion correction in MRI using image-based tracking. *Magnetic resonance in medicine* **63**, 91-105,(2010).
- 17 Waszak, M. *et al.* Prospective head motion correction using FID-guided on-demand image navigators. *Magnetic resonance in medicine* **78**, 193-203,(2016).
- 18 van der Kouwe, A. J., Benner, T. & Dale, A. M. Real-time rigid body motion correction and shimming using cloverleaf navigators. *Magnetic resonance in medicine* **56**, 1019-1032,(2006).
- 19 Johnson, P. M., Liu, J., Wade, T., Tavallaei, M. A. & Drangova, M. Retrospective 3D motion correction using spherical navigator echoes. *Magnetic Resonance Imaging* **34**, 1274-1282,(2016).
- 20 Wurslin, C. *et al.* Respiratory motion correction in oncologic PET using T1-weighted MR imaging on a simultaneous whole-body PET/MR system. *Journal of nuclear medicine* **54**, 464-471,(2013).
- 21 Fayad, H. *et al.* Respiratory and cardiac motion correction in dual gated PET/MR imaging. *EJNMMI physics* **2**, A43,(2015).
- 22 Manber, R. *et al.* Clinical Impact of Respiratory Motion Correction in Simultaneous PET/MR with a Joint PET/MR Predictive Motion Model. *Journal of nuclear medicine*,(2018).
- 23 Catana, C. *et al.* MRI-assisted PET motion correction for neurologic studies in an integrated MR-PET scanner. *Journal of nuclear medicine* **52**, 154-161,(2011).
- 24 Bickell, M., Koesters, T., Boada, F. & Nuyts, J. PET motion correction using MR-derived motion parameters. *EJNMMI physics* **1**, A53,(2014).
- 25 Chen, K. T. *et al.* MR-assisted PET motion correction in simultaneous PET/MRI studies of dementia subjects. *Journal of magnetic resonance imaging : JMRI*,(2018).

- 26 Huang, C. *et al.* MR-based motion correction for PET imaging using wired active MR microcoils in simultaneous PET-MR: phantom study. *Medical Physics* **41**, 041910,(2014).
- 27 Huang, C. *et al.* Motion compensation for brain PET imaging using wireless MR active markers in simultaneous PET-MR: phantom and non-human primate studies. *NeuroImage* **91**, 129-137,(2014).
- 28 Welch, E. B., Manduca, A., Grimm, R. C., Ward, H. A. & Jack, C. R., Jr. Spherical navigator echoes for full 3D rigid body motion measurement in MRI. *Magnetic resonance in medicine* **47**, 32-41,(2002).
- 29 Petrie, D. W., Costa, A. F., Takahashi, A., Yen, Y. F. & Drangova, M. Optimizing spherical navigator echoes for three-dimensional rigid-body motion detection. *Magnetic resonance in medicine* **53**, 1080-1087,(2005).
- 30 Liu, J. & Drangova, M. Rapid six-degree-of-freedom motion detection using prerotated baseline spherical navigator echoes. *Magnetic resonance in medicine* **65**, 506-514,(2011).
- 31 Iida, H. *et al.* Three-dimensional brain phantom containing bone and grey matter structures with a realistic head contour. *Annals of nuclear medicine* **27**, 25-36,(2013).
- 32 Pedersen, M. & Hardeberg, J. Y. Full-Reference Image Quality Metrics: Classification and Evaluation. *Foundations and Trends in Computer Graphics and Vision* **7**, 1-80,(2012).
- 33 Hore, A. & Ziou, D. Is there a relationship between peak-signal-to-noise ratio and structural similarity index measure? *IET Image Processing* **7**, 12-24,(2013).
- 34 Zhou, W., Bovik, A. C., Sheikh, H. R. & Simoncelli, E. P. Image quality assessment: from error visibility to structural similarity. *IEEE Transactions on Image Processing* **13**, 600-612,(2004).
- 35 Thesen, S., Heid, O., Mueller, E. & Schad, L. R. Prospective acquisition correction for head motion with image-based tracking for real-time fMRI. *Magnetic resonance in medicine* **44**, 457-465,(2000).

4 Conditional generative adversarial network for three-dimensional rigid-body motion correction in MRI

4.1 *Introduction*

Patient motion is a major source of artefacts in magnetic resonance imaging (MRI); blurring and artefacts caused by patient motion often lead to non-diagnostic image quality. A recent study found that approximately 20% of MRI exams require a repeat scan due to motion.¹ These repeat scans are costly, they increase wait times, and may lead to delayed diagnosis for some patients. As advances in MRI hardware and software allow us to push the limits of image resolution and image quality, patient head motion has become a limiting factor in MR neuro-imaging applications.

Over the past two decades, many techniques have been developed to address head motion in MRI. In general, these techniques measure head motion throughout the image acquisition, and then correct the image data to compensate for this motion, which can be performed either retrospectively or prospectively. The motion can be measured using optical tracking techniques that use a camera system to track markers fixed to the head.²⁻⁴ Another category of motion measurement techniques is MRI navigators, which acquire a set of MRI data, either in image space⁵⁻⁷ or k space,⁸⁻¹⁰ that is processed to measure head motion. While these tools are able to effectively correct for head motion for certain applications, they are often limited to specific pulse sequences and scanner hardware, and as such, they are not always available for routine clinical and research use. A more general tool for motion correction that does not require pulse-sequence or hardware modifications would be very valuable.

Recently, significant advancements have been made in the use of deep learning for medical imaging applications. In particular, supervised learning with deep convolutional neural networks (DCNNs) is being utilized to solve many problems in

MRI. Given training pairs of MR images, DCNNs have been trained to perform many challenging and clinically useful tasks including image reconstruction of under sampled data,¹¹⁻¹³ segmentation of structures,¹⁴⁻¹⁷ and synthesis of images with higher resolution^{18,19} or images from a different modality.²⁰ Many training pairs – examples of the input and target images – are required to train the network, which effectively learns the mapping relationship between the input and target domains. Supervised learning with DCNNs may also be well suited for the problem of motion correction, as it is common for images with motion artefacts to be reacquired – providing a source of training pairs where the input image is the motion corrupted-image and the target image is the high quality re-scans.

Deep learning for artefact removal in MRI has previously been demonstrated for the removal of ghosting artefacts in magnetic resonance spectroscopy.²¹ It has also been demonstrated for removal of Gibbs ringing²² as well as the removal of streaking artefacts in under sampled radial MRI acquisitions.¹¹ All of these successful methods are examples of image-to-image translation, which refers to the approach of training a deep neural network to predict an image in one domain from an image in another domain. Image-to-image translation problems typically use an encoder-decoder style network architecture. The encoder portion of an encoder-decoder learns a high dimensional feature vector – an abstract representation of the input, and the decoder portion learns to reconstruct the desired output from this feature vector. While highly successful in many MRI applications, DCNNs have a tendency to produce slightly blurry images. A technique that addresses this issue is a conditional generative adversarial network (cGAN).^{23,24} A cGAN combines a generator network (a DCNN) with a discriminator network (a classifier). The discriminator is trained with the generator to determine whether an image is a DCNN network output or a target image. The discriminator error contributes to the loss function of the generator, forcing the generator to produce images, which are indistinguishable from those

of the target domain. This network structure enforces sharpness and realistic looking images in the output of the DCNN.²⁴

In this work, we introduce a formulation for three-dimensional (3D) motion correction of brain images. Motion is simulated in previously acquired brain images; the image pairs (corrupted + original) are used to train a cGAN. The network has an encoder-decoder architecture for the DCNN and is paired with a discriminator. The network, MoCo-cGAN, is trained to predict artefact free brain images from motion-corrupted data.

4.2 *Methods*

4.2.1 *Data preparation*

Image data for this study were obtained from an open source MRI data repository.²⁵ The data set consists of T2* weighted multi-echo FLASH scans, from 53 participants acquired on a 7T scanner; both magnitude and phase are available. The dimensions of the FLASH volumes are 384x312x128, the TR is 41ms and the echo times are 11.22 ms, 20.39 ms. and 29.57 ms. Additional details about the scan protocol can be found in Forstmann *et al.* 2014.²⁵

For our study, we used a slab of 64 slices, from the second echo. Slices were down sampled by a factor of two, resulting in images with 1 mm in-plane resolution (192x156). The magnitude and phase were combined to form complex images, then the 3D Fast Fourier Transform was applied to yield simulated k-space data. Motion was simulated in the k-space data, as detailed in the following section. The motion-corrupted k space was transformed back into the image domain yielding a motion-corrupted image volume. A total of 5 different motion profiles were applied to each volume, and each volume was broken up into 8 patches of 192x156x8 for training. These preprocessing steps are illustrated in Figure 4-1.

The 53 image volumes were divided into training, validation and test data sets: 43 volumes (1720 patches) were used for training while the remaining 10 volumes were used for validation (5 volumes, 200 patches) and testing (5 volumes, 200 patches). All of the applied motion profiles were unique, thus each test case represents both a subject and a motion profile not previously seen in training.

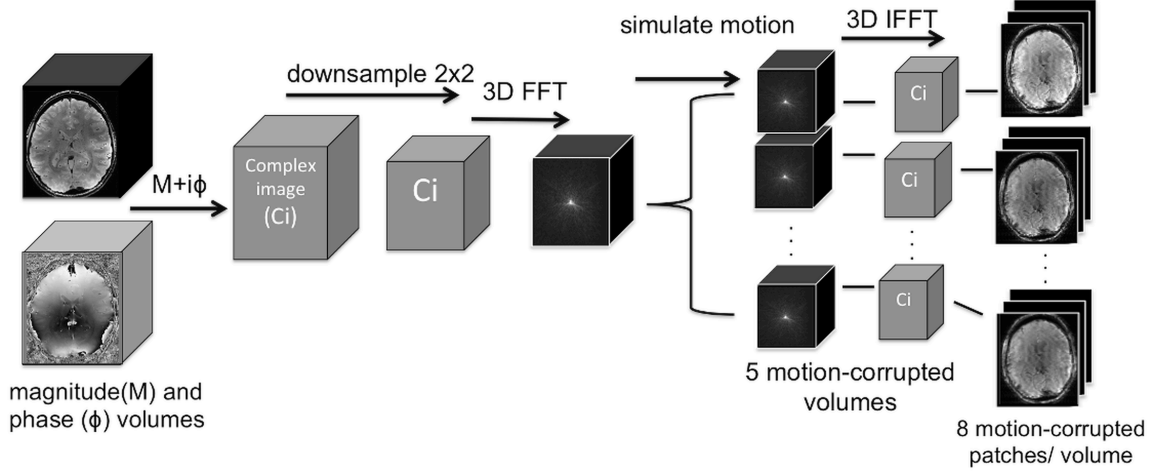


Figure 4-1 Illustration of pre-processing steps for a single subject. The magnitude and phase images are combined to form a complex image, which is then down-sampled to $192 \times 156 \times 128$. The 3D Fourier transform is applied to create k space. Five different motion profiles are applied to this k space to generate 5 motion-corrupted k-space volumes. The motion-corrupted k-space volumes are then transformed back to the image domain to yield motion corrupted images. Each motion-corrupted image is broken up into 8 patches ($192 \times 156 \times 8$) for training.

4.2.2 Motion simulation

Inter-shot motion was simulated for a Cartesian trajectory; motion profiles were generated randomly in MATLAB (MathWorks, Natick, MA) with constraints to keep the motion in the realm of realistic head motion. Motion profiles were parameterized by the number of motion events (2 or 3), and for each motion event, the time of onset and the magnitude of each motion parameter. The parameters that define the motion profiles, along with their corresponding ranges and distributions are summarized in Table 1. Axial rotation (θ_z) and head nodding

(θ_x) are common types of rotations observed during MR brain imaging. As translations typically occur with head rotation, and typically have a magnitude (in mm) that is approximately the same to the magnitude of the rotation (in degrees), the translation parameters were randomly selected from distributions with mean values determined by the random rotation. To ensure that all of the images were corrupted by motion, a score – introduced by Tisdall *et al.*²⁶ – was calculated and a threshold was established. Briefly, the motion score was calculated as follows. First, the maximum displacement (ΔR) of any point on a 64-mm radius sphere was calculated:

$$\Delta R = 64\sqrt{(1 - \cos(\theta))^2 + \sin(\theta)^2}, \quad (4.1)$$

where

$$|\theta| = \left| \arccos \left\{ \frac{1}{2} \left[-1 + \cos(\theta_x) \cos(\theta_y) + \cos(\theta_x) \cos(\theta_z) + \cos(\theta_y) \cos(\theta_z) + \sin(\theta_x) \sin(\theta_y) \sin(\theta_z) \right] \right\} \right| \quad (4.2)$$

and θ_x , θ_y , and θ_z are the applied rotations about the X, Y and Z axes respectively. Combining ΔR with the applied translations gives the motion score for a single motion event:

$$Score = \Delta R + (\Delta x^2 + \Delta y^2 + \Delta z^2). \quad (4.3)$$

For a given motion event, this score is the maximum displacement of any point on the sphere (in mm). A total motion score for each randomly generated motion profile was calculated by combining the scores from each of n motion events:

$$Score_{total} = \sqrt{\sum_i^n Score_i^2}. \quad (4.4)$$

Only randomly generated motion profiles with $Score_{total}$ greater than 5 mm were used. To simulate the effect of generated motion profiles on the k-space data, k-space lines were phase shifted based on the generated translations, then rotated and interpolated based on the generated rotation values. This procedure for motion simulation is similar to retrospective motion correction, where a measured motion profile is used to correct k-space data, however, in this case motion is applied to motion-free k-space data in order to perturb it. Finally, each motion-corrupted image was registered to its corresponding reference image in MATLAB (MathWorks, Natick, MA) using intensity-based image registration with mattes mutual information as the similarity metric. Registration was necessary to ensure that the loss function of the network generator (described below) is not dominated by image misalignment.

Table 1. Description of the parameters used to generate the random motion profiles.

Parameter	Sampling/Distribution	Min, max or mean, sd
# of motion events	simple random sampling	min = 2 max = 3
k-space line index	simple random sampling	min = 1 max = 19000
θ_x	normal distribution	mean = 0° sd = 2°
θ_y	normal distribution	mean = 0° sd = 0.1°
θ_z	normal distribution	mean = 0° sd = 2°
Δx	normal distribution	mean = θ_z mm sd = 0.1 mm
Δy	normal distribution	mean = 0 mm sd = 0.1 mm
Δz	normal distribution	mean = θ_x mm sd = 0.1 mm

4.2.3 Network architecture

The three-dimensional cGAN network architecture, illustrated in Figure 4-2, is adapted from the 2D pix2pix architecture²⁴ and includes a generator (Figure 4-2a), which is a fully-convolutional three dimensional encoder-decoder based on the U-Net architecture,²⁷ and a discriminator (Figure 4-2b). The MoCo-cGAN network was developed and trained using

the Keras library²⁸ with a TensorFlow²⁹ backend. The input to the generator network is a batch of 192x160x8 image patches; the patches were zero-padded from the original 192x156x8 in order to be compatible with the max-pooling operations of the encoder-decoder. The encoder consists of 8 convolutional layers, each of which has between 64 and 512 3x3x3 filters; batch normalization and the rectified linear unit (ReLU) activation function are applied for each convolutional layer. Dropout is applied in the final convolutional layer of the encoder. The encoder also has three max-pooling layers, each of which reduces the size of the feature vectors by a factor of 2 in each dimension.

The decoder comprises a set of eight convolutional layers mirroring the encoder, again followed by batch normalization. The activation function used for the discriminator is Leaky ReLU ($\alpha = 0.2$).³⁰ There are 3 convolution + up sampling layers that increase the size of the feature vectors by a factor of 2 in each dimension. The network has three skip connections, referring to the concatenation of feature vectors from the encoder directly to the mirroring block in the decoder.²⁷ This architecture is useful when there is significant correlation between the input and output of the network, as it allows some of the very similar low-level information to bypass further processing. Further to this concept, is the concatenation of the input to the output within each individual block of the network: the input information and the learned feature vectors are passed to the next layer in the network. The output of the generator is also a batch of 192x160x8 image patches. The discriminator (Fig 4-2b) is a convolutional neural network classifier with an input of image pairs. Some of these pairs will be an input + target image pair while others will be an input + generated image pair. This network has six convolutional layers with 4x4x4 filters; dimensionality reduction is achieved with strided convolution (stride = 2) rather than a pooling operation. A fully connected layer with a softmax activation function³¹ follows the convolutional layers.

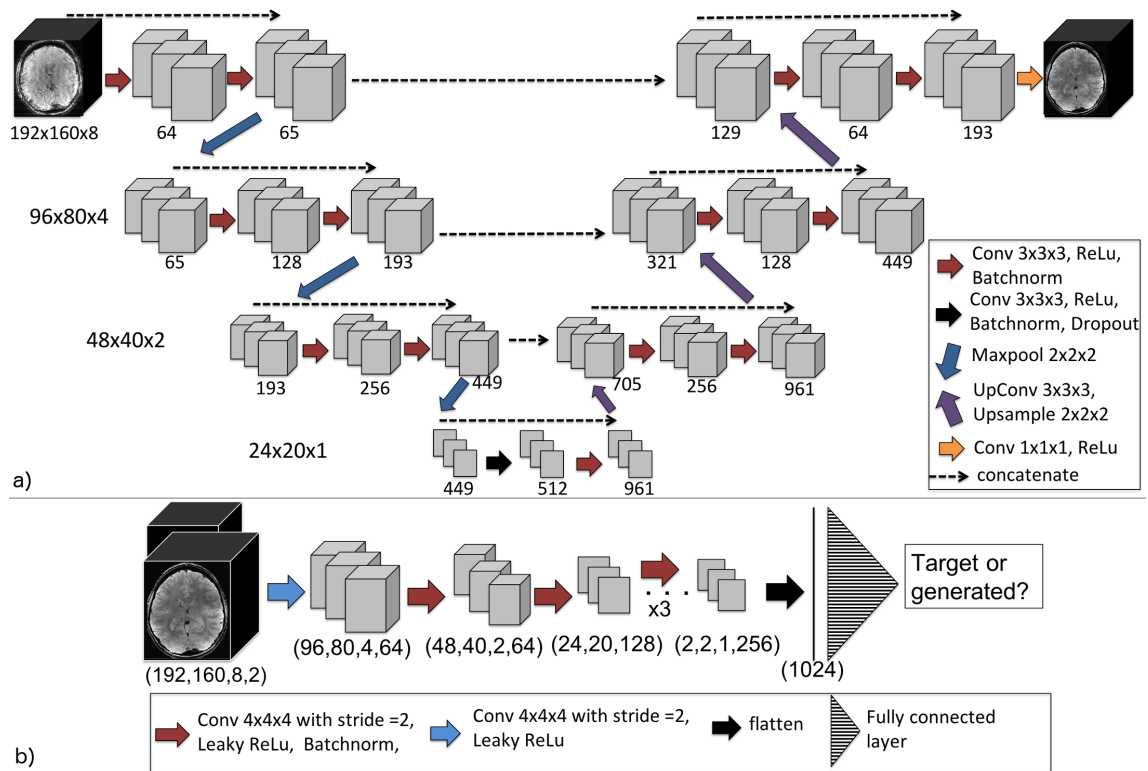


Figure 4-2 The input to the generator network (a), which is based on U-Net, is a batch of 192x160x8 brain image patches. Each set of three grey boxes represents a hidden layer with a large number of 3D feature vectors (the actual number for each layer is indicated below the boxes). In the generator diagram, the red arrows represent 3D convolution with 3x3x3 filters, a rectified linear unit activation function and batch normalization; the back arrow is the same with added dropout; the blue arrows represent the 3D maxpooling operation, while the purple arrows represent the convolution + upsampling operations. The arrows with dotted lines represent concatenation operations. The dimensions of the feature vectors in each network level are listed on the left. The input to the discriminator (b) is a batch of image pairs. In (b), the blue arrow represents 3D convolution with 4x4x4 filters, and a Leaky ReLU activation function; the red arrows are the same with the addition of batch normalization. The feature vectors are flattened (black arrow) to a 1D vector, which is then fully connected to the output layer – a decision as to whether the input image pairs contain a target or generated image.

4.2.4 *Network training*

Training a cGAN requires the generator and discriminator to be trained simultaneously. The first task of the generator (G) is to minimize the quantitative error between the input and target images, so for the first term in the generator loss function we use mean absolute error (MAE, also referred to as L1 loss). The discriminator (D) loss function is the cross entropy loss:

$$L(G, D) = -\alpha \log(D(x, y)) + (\alpha - 1) \log(1 - D(x, G(x))), \quad (4.5)$$

where x is the input image, y is the target image, α is a binary label and $G(x)$ is the generator output. If the input image is a true target image then $\alpha = 1$; if it is a generator output then $\alpha = 0$. The generator is tasked with maximizing $L(G, D)$ while the discriminator tries to minimize it. This means that the generator aims to maximize the $-\log(1 - D(x, G(x)))$ term in addition to minimizing the $L1$ loss. Ultimately, D is trained to minimize $L(G, D)$ and G is trained to minimize $L1 - \log(D(x, G(x)))$.

For both the generator and discriminator, the batch size used for training was 8, and the optimizer was the Adam optimizer³² with a learning rate of 5×10^{-5} . For the generator layer in which dropout was used, the dropout fraction was 0.5. The training images were flipped left to right to double the number of training examples. The network was trained for 40 epochs using 2 NVIDIA Tesla P100 GPUs on a supercomputer cluster. Training took approximately 18 hrs.

4.2.5 *Evaluation of network performance*

The network was evaluated on the 5 subjects (200 patches) reserved for the test set. For qualitative analysis, difference images were calculated where the motion corrupted and corrected images were subtracted from the corresponding stationary reference image. All images were scaled from 0 to 1 prior to the calculation of the difference images and

image quality metrics. To quantify the improvement in MR image quality, motion-corrupted and DCNN-corrected volumes (192x156x64) were compared to the reference image using MAE (generator loss function), peak signal-to-noise ratio (PSNR), and structural similarity index (SSIM).³³ PSNR approaches infinity and SSIM approaches one as the numerical difference between the images approaches zero. PSNR is considered to be an objective measure of image quality while PSNR is considered to be correlated with perceptual image quality of the human visual system.³⁴ More details about these metrics can be found in section 3.2.

4.3 Results

4.3.1 Motion correction: image results

The trained MoCO-cGAN successfully achieved qualitative image improvement for all of the motion-corrupted test-set volumes (rotations up to 3.5° and translations up to 4.1 mm). Representative correction results for three subjects, along with the corresponding motion profiles, are shown in Figure 4-3. Representative axial slices of the motion-corrupted, corrected, and reference images are shown, along with the calculated difference images. Using the trained MoCO-cGAN resulted in significant artefact suppression and reduced blurring, which is further demonstrated in the sagittal and coronal images (of the same subjects) shown in Figure 4-4. For the second subject, there was an apparent motion artefact in the axial reference image, which is not present in the corrected image.

4.3.2 Quantitative evaluation

Quantitatively, all motion corrected images improved compared to the motion-corrupted images. For all 25-image volumes in the test set (5 subjects with 5 motion profiles each), MoCO-cGAN motion correction resulted in a decreased MAE and an increased SSIM and PSNR, as shown in Figure 4-5. The average MAE for the

uncorrected images was 0.0215– or 20.1% of the image mean; this was reduced to 0.0147 or 13.7% of the image mean value in the corrected images.

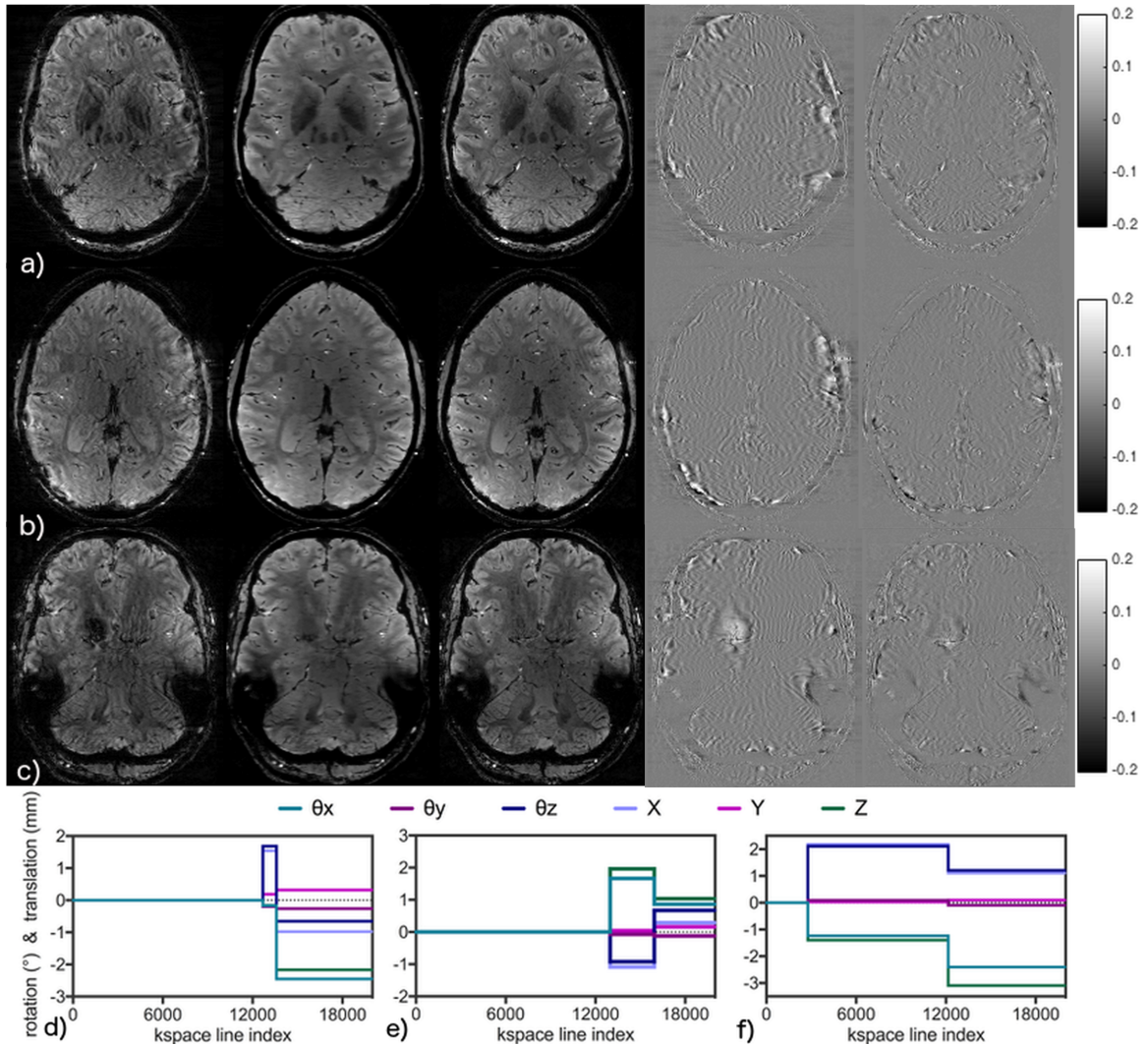


Figure 4-3 Representative MoCo-cGAN motion correction results. From left to right, a single axial slice of the motion-corrupted, motion-corrected and reference images are shown for subjects 1(a), 2(b) and 3(c). The difference images are shown in the fourth (reference – motion) and fifth (reference – corrected) columns. The colour bars show the range of pixel intensities in the difference images (original images were scaled from 0 to 1). The corresponding motion profiles are plotted in (d) through (f). The arrow in the reference image for subject 2, points to a ringing motion artefact that is not present in the corrected image, suggesting that the MoCo-cGAN network corrected a real motion artefact in addition to the simulated motion artefacts.

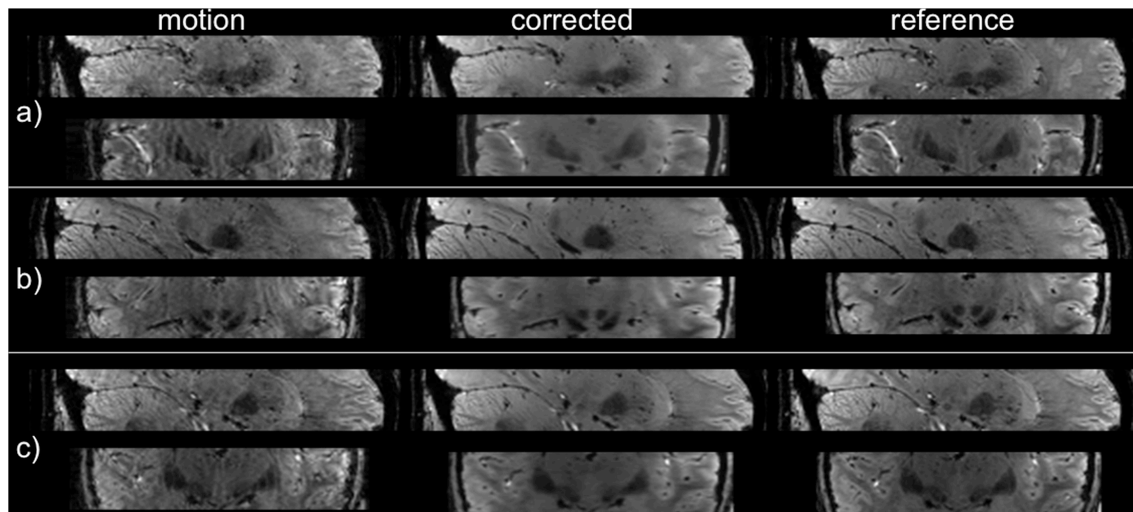


Figure 4-4 Sagittal and coronal views of the volumes shown in Figure 4-3. From left to right, a single sagittal (top) and coronal slice (bottom) of the motion-corrupted, motion-corrected and reference images are shown for subjects 1(a), 2(b) and 3(c).

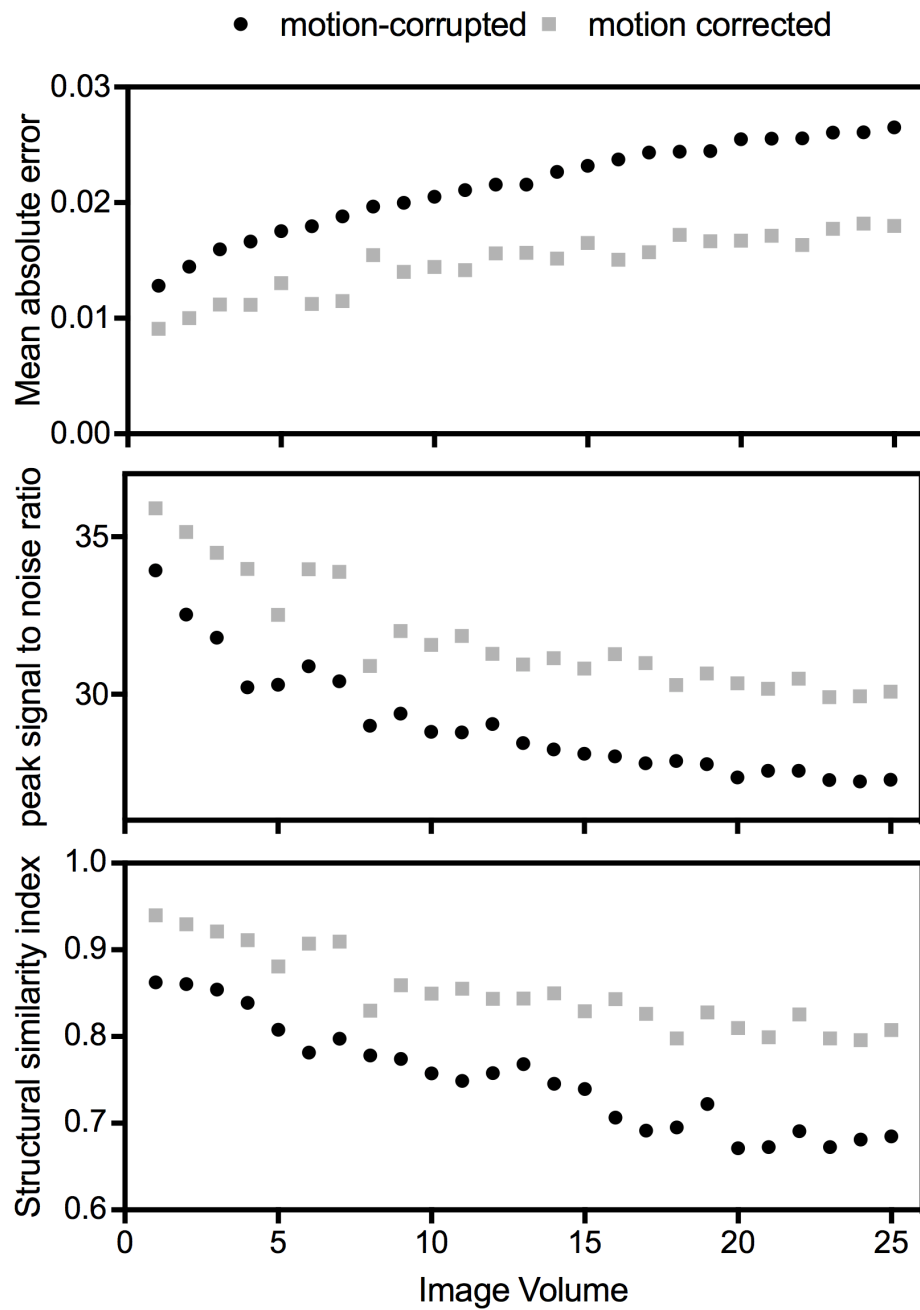


Figure 4-5 Mean absolute error (a), peak signal to noise ratio (b), and structural similarity index (c) calculated for all 25 image volumes. For clarity, the 25 volumes were sorted from lowest to highest mean absolute error of the motion-corrupted image.

4.4 Discussion

This work represents a novel solution to three-dimensional motion correction in brain MRI; the trained conditional generative adversarial network – MoCo-cGAN – successfully performed motion correction on brain images with simulated motion. For all 5 subjects in the test group, and applied motion profiles, the motion corrected images are qualitatively improved; artefact suppression and reduced blurring is observed in the corrected images. The calculated difference images also highlight the artefact suppression and demonstrate that the corrected images are more similar to the reference images. All predicted images quantitatively demonstrated improved quality, with an over 30% decrease in MAE, and corresponding increases in PSNR, and SSIM, demonstrating that the MoCO-cGAN network can consistently correct for motion.

Current motion correction techniques, including navigators and optical tracking, require that the motion is measured in order to correct the MRI data. While these techniques have been successful for motion correction, they are generally appropriate only for specific applications. A deep learning technique for motion correction could be more generally applicable as it is an exclusively post-processing method and does not require any measurement of the motion throughout the scan. Deep learning techniques, and in particular cGANs, have been demonstrated for MRI reconstruction and improving MR image resolution in prior work.^{35,36} The motivation for using a cGAN for motion correction comes from the success and generalizability of pix2pix, which has been applied to many diverse tasks. To our knowledge, this is the first time a cGAN has been used for motion correction.

Motion correction was demonstrated on images with simulated motion, and although the motion profiles were randomly generated and constrained to resemble typical head motion, simulated motion cannot model all of the complexities of *in vivo* head motion and its effect on the image data. In particular, the field distortions that typically occur

in real head motion are not incorporated into the motion simulation. Using simulated motion however allowed us to evaluate motion correction in a controlled environment with a large dataset and true reference images. Importantly, a real motion artefact in the reference image of the second subject was corrected along with the simulated motion artefacts; this demonstrates that the network can correct for real *in vivo* motion. Insights gained from the development and training of this network are expected to be directly transferable to different image acquisitions and datasets with real motion. The trained MoCo-cGAN could potentially serve as a pre-trained network for future training with real motion and for images with different contrast, resolution and SNR. It has been previously demonstrated that this type of transfer learning is very effective and reduces the amount of training data needed.³⁷ It is common for images with motion artefacts to be reacquired in a clinical setting; these image pairs could be used to fine-tune a network pre-trained with simulated motion.

In this work, motion correction of MR images was treated as a supervised image-to-image translation problem. Unsupervised image-to-image translation could be another potential solution to this problem and would eliminate the need for image pairs. The cycle-GAN implementation is an example of image-to-image translation with unpaired images. The network simply requires a set of images belonging to the input and target domains. Another solution might be a supervised convolutional neural network that operates directly on k space,³⁸ to translate corrupted k space to a motion-corrected k space. MRI motion correction can also be approached as an image reconstruction problem. Several techniques have been developed to reconstruct images from under-sampled data and similar techniques could potentially be applied to data that is incorrectly sampled due to head motion. For example, AutoMap¹³ can be applied to motion corrected reconstruction directly from raw k-space data.³⁹ However, our initial experience with this network for motion correction suggests that it is more prone to over fitting than MoCo-cGAN, and memory requirements are a concern. MoCo-cGAN

effectively reduces artefacts and blurring due to simulated motion. It is a technique that requires no pulse sequence modifications or interactions with scanner hardware, and as such could be a promising general solution to rigid-body motion correction in brain MRI.

4.5 *Conclusion*

The MoCO-cGAN deep learning approach enables retrospective correction of MR images with simulated motion, consistently resulting in reduced motion artefacts and motion blurring.

4.6 References

- 1 Andre, J. B. *et al.* Toward Quantifying the Prevalence, Severity, and Cost Associated With Patient Motion During Clinical MR Examinations. *Journal of the American College of Radiology : JACR* **12**, 689-695,(2015).
- 2 Stucht, D. *et al.* Highest Resolution In Vivo Human Brain MRI Using Prospective Motion Correction. *PloS one* **10**, e0133921,(2015).
- 3 Mattern, H. *et al.* Prospective motion correction enables highest resolution time-of-flight angiography at 7T. *Magnetic resonance in medicine* **80**, 248-258,(2018).
- 4 Maclaren, J., Aksoy, M., Ooi, M. B., Zahneisen, B. & Bammer, R. Prospective motion correction using coil-mounted cameras: Cross-calibration considerations. *Magnetic resonance in medicine* **79**, 1911-1921,(2018).
- 5 Waszak, M. *et al.* Prospective head motion correction using FID-guided on-demand image navigators. *Magnetic resonance in medicine* **78**, 193-203,(2016).
- 6 Tisdall, M. D. *et al.* Prospective motion correction with volumetric navigators (vNavs) reduces the bias and variance in brain morphometry induced by subject motion. *NeuroImage* **127**, 11-22,(2016).
- 7 Gallichan, D., Marques, J. P. & Gruetter, R. Retrospective correction of involuntary microscopic head movement using highly accelerated fat image navigators (3D FatNavs) at 7T. *Magnetic resonance in medicine* **75**, 1030-1039,(2015).
- 8 van der Kouwe, A. J., Benner, T. & Dale, A. M. Real-time rigid body motion correction and shimming using cloverleaf navigators. *Magnetic resonance in medicine* **56**, 1019-1032,(2006).
- 9 Johnson, P. M., Liu, J., Wade, T., Tavallaei, M. A. & Drangova, M. Retrospective 3D motion correction using spherical navigator echoes. *Magnetic resonance imaging* **34**, 1274-1282,(2016).
- 10 Wallace, T. E., Afacan, O., Waszak, M., Kober, T. & Warfield, S. K. Head motion measurement and correction using FID navigators. *Magnetic resonance in medicine* **doi: 10.1002/mrm.27381**,(2018).
- 11 Han, Y. *et al.* Deep learning with domain adaptation for accelerated projection-reconstruction MR. *Magnetic resonance in medicine* **80**, 1189-1205,(2018).
- 12 Hammernik, K. *et al.* Learning a variational network for reconstruction of accelerated MRI data. *Magnetic resonance in medicine* **79**, 3055-3071,(2018).

- 13 Zhu, B., Liu, J. Z., Cauley, S. F., Rosen, B. R. & Rosen, M. S. Image reconstruction by domain-transform manifold learning. *Nature* **555**, 487,(2018).
- 14 Wang, G. *et al.* Interactive Medical Image Segmentation Using Deep Learning With Image-Specific Fine Tuning. *IEEE transactions on medical imaging* **37**, 1562-1573,(2018).
- 15 Laukamp, K. R. *et al.* Fully automated detection and segmentation of meningiomas using deep learning on routine multiparametric MRI. *European radiology* **doi: 10.1007/s00330-018-5595-8**,(2018).
- 16 Bernard, O. *et al.* Deep Learning Techniques for Automatic MRI Cardiac Multi-structures Segmentation and Diagnosis: Is the Problem Solved? *IEEE transactions on medical imaging*,(2018).
- 17 Praveen, G. B., Agrawal, A., Sundaram, P. & Sardesai, S. Ischemic stroke lesion segmentation using stacked sparse autoencoder. *Computers in biology and medicine* **99**, 38-52,(2018).
- 18 Shi, J. *et al.* MR Image Super-Resolution Via Wide Residual Networks With Fixed Skip Connection. *IEEE journal of biomedical and health informatics*,(2018).
- 19 Shi, J. *et al.* Super-resolution reconstruction of MR image with a novel residual learning network algorithm. *Physics in medicine and biology* **63**, 085011,(2018).
- 20 Nie, D. *et al.* Medical Image Synthesis with Context-Aware Generative Adversarial Networks. *Medical image computing and computer-assisted intervention* **10435**, 417-425,(2017).
- 21 Kyathanahally, S. P., Doring, A. & Kreis, R. Deep learning approaches for detection and removal of ghosting artifacts in MR spectroscopy. *Magnetic resonance in medicine* **80**, 851-863,(2018).
- 22 Wang, Y. *et al.* Reduction of Gibbs artifacts in magnetic resonance imaging based on Convolutional Neural Network *2017 10th International Congress on Image and Signal Processing, BioMedical Engineering and Informatics (CISP-BMEI)*,(2017).
- 23 Mirza, M. & Osindero, S. Conditional Generative Adversarial Nets. *arXiv:1411.1784* (2014).
- 24 Isola, P., Zhu, J.-Y., Zhou, T. & Efros, A. Image-to-Image Translation with Conditional Adversarial Networks. *arXiv:1611.07004 [cs.CV]*,(2017).
- 25 Forstmann, B. U. *et al.* Multi-modal ultra-high resolution structural 7-Tesla MRI data repository. *Scientific Data* **1**, 140050,(2014).

- 26 Tisdall, M. D. *et al.* Volumetric navigators for prospective motion correction and selective reacquisition in neuroanatomical MRI. *Magnetic resonance in medicine* **68**, 389-399,(2012).
- 27 Ronneberger, O., Fischer, P. & Brox, T. U-Net: Convolutional Networks for Biomedical Image Segmentation in *Medical Image Computing and Computer-Assisted Intervention – MICCAI 2015*. (eds Nassir Navab, Joachim Hornegger, William M. Wells, & Alejandro F. Frangi) 234-241 (Springer International Publishing).
- 28 Chollet, F. keras, GitHub. <https://github.com/fchollet/keras>. *GitHub repository*,(2015).
- 29 Abadi, N. *et al.* TensorFlow: Large-scale machine learning on heterogeneous systems. <https://static.googleusercontent.com/media/research.google.com/en//pubs/archive/45166.pdf>. (2015).
- 30 Chollet, F. keras advanced activations, GitHub. <https://github.com/fchollet/keras>.(2015).
- 31 Chollet, F. Keras activations, GitHub. <https://github.com/fchollet/keras>.(2015).
- 32 Kingma, D. P. & Ba, J. Adam: A Method for Stochastic Optimization. *arXiv:1412.6980*
- 33 Pedersen, M. & Hardeberg, J. Y. Full-Reference Image Quality Metrics: Classification and Evaluation. *Foundations and Trends in Computer Graphics and Vision* **7**, 1-80,(2012).
- 34 Hore, A. & Ziou, D. Is there a relationship between peak-signal-to-noise ratio and structural similarity index measure? *IET Image Processing* **7**, 12-24,(2013).
- 35 Quan, T. M., Nguyen-Duc, T. & Jeong, W. K. Compressed Sensing MRI Reconstruction Using a Generative Adversarial Network With a Cyclic Loss. *IEEE transactions on medical imaging* **37**, 1488-1497,(2018).
- 36 Kim, K. H., Do, W. J. & Park, S. H. Improving resolution of MR images with an adversarial network incorporating images with different contrast. *Medical physics* **45**, 3120-3131,(2018).
- 37 Knoll, F. *et al.* Assessment of the generalization of learned image reconstruction and the potential for transfer learning. *Magnetic resonance in medicine* **doi: 10.1002/mrm.27355**,(2018).

- 38 Han, Y. & Ye, J. C. k-Space Deep Learning for Accelerated MRI. *arXiv:1805.03779 [cs.CV]*,(2018).
- 39 Johnson, P. M. & Drangova, M. Motion correction in MRI using deep learning *Proceedings of the annual meeting of the International Society of Magnetic Resonance in Medicine #4098 4098*,(2018).

5 Conclusions and Future Directions

5.1 *Contributions*

5.1.1 *SNAVs*

Prior to the development of the hybrid baseline approach described in this work, the baseline scan required 26s to acquire. If the subject moved during this 26s the accuracy of motion measurements would be significantly affected. In Chapter 2, I described the hybrid baseline method, which reduces the acquisition time by simulating many of the pre-rotated templates offline. The acquisition time for the baseline scan was reduced to 2.6 s, making it far more practical for motion correction in clinical applications.

This work presents the first time SNAVs have been demonstrated for intra-image motion correction. Earlier work had focused on optimizing the SNAVs for motion measurement, but not correction. The implementation of SNAVs in an SPGR image sequence allowed for motion correction of a clinically relevant sequence for structural neuroimaging.

Chapter 3 presents the first use of navigators for the correction of simultaneously acquired PET and MRI data. Previous work in the field had used MRI motion tracking to correct the PET data, but the MRI was used exclusively for the purpose of motion tracking and no diagnostic MR images were acquired. Embedding SNAVs into a turbo FLASH sequence enables the retrospective correction of both modalities and allows us to fully exploit the hybrid imaging modality.

5.1.2 *MoCo-cGan*

MRI motion correction has been an active area of research for almost 30 years. The vast majority of the methods developed in this time involved measuring the motion – with MRI navigators, optical tracking, or active markers – followed by correction of

the k-space data either retrospectively or prospectively. The work presented in Chapter 4 uses deep learning for motion correction and does not require explicit motion measurement. It is a potentially more general tool for motion correction than current methods. MoCo-cGAN is the first time a cGAN was used for motion correction of MR images. I expect this work will serve as a building block for further development of deep learning methods for motion correction in MRI. The insights gained from the development and training of this network will be transferable to different types of images as well as images with real motion.

5.2 Conclusions

The presented hybrid baseline SNAV template approach enables the acquisition of a pre-rotated baseline template set in only 2.6 s, followed by template simulation. A truncated SNAV with as few as 8 helical turns performed comparably to full SNAV acquisitions. This method results in accurate measurements of phantom rotations and translations. *In vivo* motion was measured and retrospective motion correction was successfully performed.

The presented SNAV motion correction for hybrid PET/MRI approach enables the retrospective correction of simultaneously acquired PET and MR images. This method consistently results in reduced motion artefacts and motion blurring.

The MoCO-cGAN deep learning approach enables retrospective correction of MR images with simulated motion, consistently resulting in reduced motion artefacts and motion blurring.

5.3 Limitations

5.3.1 SNAVs

In my thesis I presented retrospective SNAV motion correction for both standalone MRI and hybrid PET/MRI. Prospective motion correction keeps the image coordinate system fixed relative to the object and unlike retrospective motion correction avoids gaps in k space that occur due to object rotation. These gaps in k space following rotations are an inherent limitation in retrospective rotation correction. A direct comparison between retrospective and prospective motion correction has never been performed. This would be a valuable future study and is described in section 5.4.2.

The SNAV implementation described in Chapter 2 for MRI motion correction incorporates the SNAVs into an SPGR sequence. A limitation of this specific implantation is the lengthened scan time. The SNAV implementation for the PET/MRI, described in Chapter 3, does not increase the scan time, but the temporal resolution of motion estimates is low (2.2 s). SNAVs require a 3D excitation, this would make SNAVs challenging for 2D acquisitions due to the mismatch in excitation volumes.

In general, a limitation of MRI navigators is the significant time and expertise needed to include them in each specific pulse sequence. We described the incorporation of SNAVs into two sequences, but much more work would need to be done in order to have SNAVs available for a wide range of applications, and across all vendors.

A 19s Dixon MRI scan – required for attenuation correction of PET data – is acquired prior to the simultaneous PET/MRI acquisition. This scan is not motion corrected. If motion occurs during this time, errors could be introduced in the attenuation correction maps required for the PET images. Additionally, the motion correction for hybrid PET/MRI was demonstrated only in phantoms which cannot model all of the complexities of *in vivo* imaging.

5.3.2 MoCo-cGAN

In Chapter 4, motion correction was demonstrated on images with simulated motion, which cannot model all of the complexities of *in vivo* head motion and its effect on the image data. In particular, the field distortions that typically occur in real head motion are not incorporated into the motion simulation. Additionally, we have demonstrated motion correction only on a single type of image. Images with different contrast, resolution and k-space trajectories will have motion artefacts that appear different. The network will likely need to be fine-tuned using a small number of training pairs for different types of images. For some applications, these training pairs may be difficult to obtain.

It has been shown that generative adversarial models can hallucinate features in medical image synthesis.¹ These networks are trained to match the target distribution in the training set which can be problematic when certain features are over or under-represented in the training set. For example, a network can inadvertently be trained to remove pathology from an image if there is no pathology in the training set.¹ A better understanding of this limitation and how to avoid adding or removing features is necessary before this technology can be considered reliable for diagnostic imaging.

5.4 SNAVs: Suggestions for future work

In this thesis I have demonstrated that SNAVs are effective for retrospective motion correction in MRI. There are many possible future directions for this promising technique including implementing SNAVs for prospective motion correction, in different pulse sequences, and potentially for respiratory motion correction in cardiac MRI. It would also be valuable to evaluate SNAVs in a patient population.

5.4.1 *SNAVs for a variety of pulse sequences and applications*

In this thesis, the SNAVs were incorporated into SPGR on the GE scanner and TFL on the Siemens scanner; both sequences are T1 weighted. SNAVs have an even greater potential impact in sequences with long repetition times and substantial dead time. Specifically, T2 weighted fluid attenuated inversion recovery (T2-FLAIR) would significantly benefit from SNAV motion correction. T2-FLAIR is a promising application because there is sufficient dead time to accommodate the navigators and it is a standard protocol in routine clinical brain imaging.² A FLAIR acquisition can take up to 15 mins, making motion a common problem. Another promising application is diffusion tensor imaging, which could benefit from the incorporation of SNAVs between diffusion volumes.

Sampling the free induction decay (FID) prior to the application of the SNAV gradient waveforms (FID-SNAV) enables the measurement and correction of zeroth order field shifts that occur due to motion and field drifts in the main magnetic field. Our initial experience with FID-SNAVs suggest that there are improvements to image quality when zeroth order field shift correction is applied in addition to motion correction. FID-SNAVs could be particularly useful in long, gradient intensive scans where the field drift may be substantial.

While this thesis focused on SNAVs for brain imaging applications, they may also be useful in muscular-skeletal (MSK) imaging. Specifically, patient motion of the foot during foot and ankle imaging is likely to meet the rigid-body requirement. MRI of the foot and ankle is commonly used to assess the peripheral nerves,³ soft tissue injuries⁴ and arthritis.⁵ As both the SPGR and turbo flash sequences described in this thesis are popular sequences for MSK imaging,⁶ SPGR-SNAV and tfl-SNAV promise to be useful tools for motion correction in foot and ankle imaging.

5.4.2 *Implement SNAVs for prospective motion correction*

As discussed earlier in this thesis, rotational motion results in regions of k space devoid of data and this under sampling is difficult to recover from retrospectively. A prospective correction technique will not require the interpolation of missing data and is therefore thought to be a superior method of motion correction. Additionally, prospective correction will eliminate the need for post-processing which will be beneficial for clinical workflow. To implement prospective motion correction, SNAV data needs to be sent from the scanner to the host computer immediately after acquisition. Rotations and translations can then be measured, and the rotation measurements can be fed back to the scanner in order to update the gradient rotation matrix. Translation correction can be applied just prior to image reconstruction. This pipeline is already implemented on the Siemens platform for PACE. To use SNAVs instead of the EPI volume navigators, the reconstruction software that calculates motion parameters by registering the EPI volumes would have to be replaced by our software for processing SNAVs. The rest of the PACE pipeline would likely only require minor modifications.

It would be valuable to compare a prospective motion correction approach with retrospective motion correction. Subjects could be instructed to remain still for a reference image and then perform similar movements in two acquisitions – one of which would be prospectively motion corrected and the other retrospectively. The motion parameters for the two acquisitions could be compared to verify that the motion profiles are comparable. This set of experiments would allow for a direct comparison between prospective and retrospective motion correction.

5.4.3 *Evaluate SNAVs in a patient population*

In this thesis I demonstrated SNAV motion correction in healthy subjects and in phantoms. Future work should evaluate SNAV motion correction in a patient population. PET/MRI is a promising modality for imaging in epilepsy and brain cancer patients. These exams are lengthy and would significantly benefit from SNAV motion correction. To evaluate the effectiveness of the motion correction, the original and motion corrected images could be evaluated and scored by a radiologist.

5.4.4 *Cardiac fat SNAVs*

Fat selective SNAVs for respiratory motion correction in cardiac imaging would be an interesting and impactful avenue for future work. Successful beat-to-beat motion correction using SNAVs would eliminate the need for respiratory gating thereby improving scan efficiency. If cardiac gating is applied and the SNAV is acquired in diastole where the rigid-body assumption can be met, it could allow for motion tracking of the heart during respiration. In preliminary work to develop the cardiac SNAVs, it was found that field changes caused by respiration affected the frequency selection of the navigator and introduced phase shifts in the navigators that affected the motion estimates. Additionally, achieving consistent magnetization preparation between baseline navigators and navigators acquired during image acquisition was also challenging. If these issues can be addressed, spherical navigators could enable beat-to-beat motion correction, allowing for more efficient free breathing acquisitions.

5.5 *MoCo-cGAN: suggestions for future work*

5.5.1 *Fine-tune MoCo-cGAN for images with real motion.*

My pioneering work on the use of deep learning for motion correction opens up exciting new opportunities for research. Future work for deep learning motion correction should

focus on evaluating the MoCo-cGAN network on images with real motion and images with varying contrast, SNR, and resolution. I propose a study involving common brain imaging protocols, perhaps MP-RAGE, T2-FLAIR and TSE. For these protocols, clinical images that are reacquired due to head motion could be saved along with their respective rescans. A few image pairs with a high quality rescan would then be used to fine-tune the MoCo-cGAN network for each protocol. This set of experiments would allow for evaluation of the transfer learning potential of the network.

5.5.2 *Deep learning-based motion corrected MRI reconstruction*

In Chapter 4 an image-to-image translation approach to motion correction was described. MRI motion correction could also be approached as an image reconstruction problem. For example, AutoMap⁷ can be applied to reconstruct a motion-corrected image directly from motion-corrupted k-space data.⁸ However, our initial experience with this network for motion correction suggests that it is more prone to over fitting than MoCo-cGAN, and memory requirements are a concern.⁸ The fully connected layer at the beginning of the network has a very large number of learnable parameters that contributes to the high memory requirements and over-fitting. If the network can be redesigned such that the first layer is more sparsely connected but still retains sufficient model capacity, AutoMap could be a promising approach for motion correction.

5.5.3 *Deep learning motion correction with unpaired image to image translation.*

Unsupervised image-to image translation could be another potential solution to motion correction and would eliminate the need for image pairs. The cycle-GAN implementation is an example of image-to-image translation with unpaired images.⁹ The network simply requires a set of images belonging to the input and target domains.

Similar to MoCo-cGAN, cycle-GAN uses a generator (G) to transform an input image to an output image and a discriminator (D) to classify the generated image as real or fake, with the classification error contributing to the loss function. Unlike MoCo-cGAN the second loss term cannot be MAE between the output and target because the images are not paired. Instead, a cycle consistency loss term is used. The concept of cycle consistency loss, and the proposed cycle-GAN motion correction framework is illustrated in Figure 5-1. Cycle-GAN has two generators – one that transforms the input image to the output image, and one that performs the opposite transformation. In Figure 5-1 this is illustrated by a motion-corrupted image being transformed to a motion-corrected image by generator G and then being transformed back to a motion-corrupted image by generator F. The mean absolute error is calculated between the output of F and the input of G. This cycle-loss MAE term is used in the overall loss function for generator G:

$$-\log(D(x, G(x))) + \alpha C, \quad (5.1)$$

where x is the input to G, C is the cycle consistency loss and α is a tuneable hyperparameter that sets the relative weight between the two loss terms.

Applying cycle-GAN to motion correction would have to be slightly different than the original cycle-GAN network. The forward transformation (motion-corrupted \rightarrow motion corrected) has only one solution, while the opposite transformation is an ill-posed problem, as there is an infinite number of possible motion-corrupted images for any image without motion artefacts. For motion correction then, the cycle-consistency requirement would have to be relaxed (i.e. α would need to be lower than in most applications) which may lead to insufficient constraints on the optimization problem. However, data consistency can be enforced separately in image space and k space, which would add an additional constraint. The output of the reverse generator would be transformed to k space and a cycle consistency loss between this k space and the k

space of the input image could be calculated. Ultimately, the loss function would look like:

$$-\log(D(x, G(x))) + \alpha C_i + \beta C_k \quad (5.2)$$

where the $-\log(D(x, G(x)))$ term is the discriminator loss term as described in Chapter 4, and C_i and C_k are the cycle consistency loss in image space and k space respectively. α and β are again tunable hyper-parameters that set the relative weights between the loss terms. It may be useful to restrict the k-space consistency loss to voxels closer to the center of k space where distortions from rotations would be less severe.

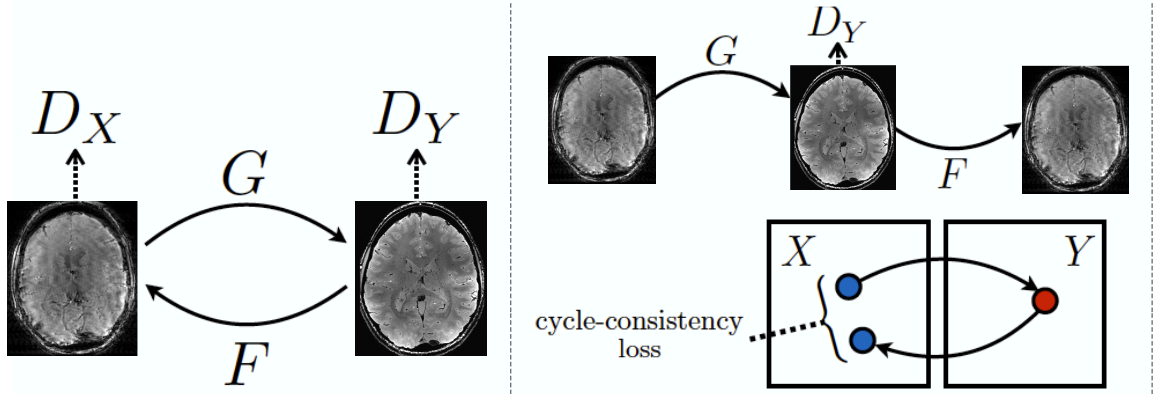


Figure 5-1 Illustration of cycle-GAN. A motion-corrupted image is transformed by generator G to an artefact free image. The output of G becomes the input to a discriminator which classifies the image as a real image or a generator image. An artefact free image is transformed by generator F to a motion-corrupted image and becomes the input to a second discriminator. Training generator G involves maximizing the discriminator error and minimizing the cycle-consistency loss.

5.6 References

- 1 Cohen, J., Luck, M. & Honari, S. Distribution Matching Losses Can Hallucinate Features in Medical Image Translation. *arXiv:1805.08841*,(2018).
- 2 Thurston, M. & Niknejad, M. *Radiopaedia: Fluid attenuation inversion recovery*, <<https://radiopaedia.org/articles/fluid-attenuation-inversion-recovery>> (
- 3 Chhabra, A. *et al.* MR Neurography: Past, Present, and Future. *American Journal of Roentgenology* **197**, 583-591,(2011).
- 4 Hodgson, R. J., O'Connor, P. J. & Grainger, A. J. Tendon and ligament imaging. *The British Journal of Radiology* **85**, 1157-1172,(2012).
- 5 Tehranzadeh, J., Ashikyan, O. & Dascalos, J. Magnetic resonance imaging in early detection of rheumatoid arthritis. *Seminars in musculoskeletal radiology* **7**, 79-94,(2003).
- 6 Naraghi, A. & White, L. M. Three-Dimensional MRI of the Musculoskeletal System. *American Journal of Roentgenology* **199**, W283-W293,(2012).
- 7 Zhu, B., Liu, J. Z., Cauley, S. F., Rosen, B. R. & Rosen, M. S. Image reconstruction by domain-transform manifold learning. *Nature* **555**, 487,(2018).
- 8 Johnson, P. M. & Drangova, M. Motion correction in MRI using deep learning *Proceedings of the annual meeting of the International Society of Magnetic Resonance in Medicine #4098* **4098**,(2018).
- 9 Zhu, J.-Y., Park, T., Isola, P. & Efros, A. Unpaired Image-to-Image Translation using Cycle-Consistent Adversarial Networks. *arXiv:1703.10593*,(2018).

APPENDIX

Appendix A

Permission for reproduction of scientific articles

Appendix A.1: Reprint Permission: Chapter 1, Figure 1-4

11/1/2018

RightsLink - Your Account

JOHN WILEY AND SONS LICENSE TERMS AND CONDITIONS

Nov 01, 2018

This Agreement between Patricia Johnson ("You") and John Wiley and Sons ("John Wiley and Sons") consists of your license details and the terms and conditions provided by John Wiley and Sons and Copyright Clearance Center.

License Number	4457730509920
License date	Oct 28, 2018
Licensed Content Publisher	John Wiley and Sons
Licensed Content Publication	Magnetic Resonance in Medicine
Licensed Content Title	Spherical navigator echoes for full 3D rigid body motion measurement in MRI
Licensed Content Author	Edward Brian Welch, Armando Manduca, Roger C. Grimm, et al
Licensed Content Date	Dec 20, 2001
Licensed Content Volume	47
Licensed Content Issue	1
Licensed Content Pages	10
Type of Use	Dissertation/Thesis
Requestor type	University/Academic
Format	Print and electronic
Portion	Figure/table
Number of figures/tables	1
Original Wiley figure/table number(s)	Figure 1
Will you be translating?	No
Title of your thesis / dissertation	Retrospective motion correction in magnetic resonance imaging of the brain
Expected completion date	Dec 2018
Expected size (number of pages)	140
Requestor Location	Patricia Johnson

11/1/2018

RightsLink - Your Account

- The materials you have requested permission to reproduce or reuse (the "Wiley Materials") are protected by copyright.
- You are hereby granted a personal, non-exclusive, non-sub licensable (on a stand-alone basis), non-transferable, worldwide, limited license to reproduce the Wiley Materials for the purpose specified in the licensing process. This license, **and any CONTENT (PDF or image file) purchased as part of your order**, is for a one-time use only and limited to any maximum distribution number specified in the license. The first instance of republication or reuse granted by this license must be completed within two years of the date of the grant of this license (although copies prepared before the end date may be distributed thereafter). The Wiley Materials shall not be used in any other manner or for any other purpose, beyond what is granted in the license. Permission is granted subject to an appropriate acknowledgement given to the author, title of the material/book/journal and the publisher. You shall also duplicate the copyright notice that appears in the Wiley publication in your use of the Wiley Material. Permission is also granted on the understanding that nowhere in the text is a previously published source acknowledged for all or part of this Wiley Material. Any third party content is expressly excluded from this permission.
- With respect to the Wiley Materials, all rights are reserved. Except as expressly granted by the terms of the license, no part of the Wiley Materials may be copied, modified, adapted (except for minor reformatting required by the new Publication), translated, reproduced, transferred or distributed, in any form or by any means, and no derivative works may be made based on the Wiley Materials without the prior permission of the respective copyright owner. **For STM Signatory Publishers clearing permission under the terms of the STM Permissions Guidelines only, the terms of the license are extended to include subsequent editions and for editions in other languages, provided such editions are for the work as a whole in situ and does not involve the separate exploitation of the permitted figures or extracts**, You may not alter, remove or suppress in any manner any copyright, trademark or other notices displayed by the Wiley Materials. You may not license, rent, sell, loan, lease, pledge, offer as security, transfer or assign the Wiley Materials on a stand-alone basis, or any of the rights granted to you hereunder to any other person.
- The Wiley Materials and all of the intellectual property rights therein shall at all times remain the exclusive property of John Wiley & Sons Inc, the Wiley Companies, or their respective licensors, and your interest therein is only that of having possession of and the right to reproduce the Wiley Materials pursuant to Section 2 herein during the continuance of this Agreement. You agree that you own no right, title or interest in or to the Wiley Materials or any of the intellectual property rights therein. You shall have no rights hereunder other than the license as provided for above in Section 2. No right, license or interest to any trademark, trade name, service mark or other branding ("Marks") of WILEY or its licensors is granted hereunder, and you agree that you shall not assert any such right, license or interest with respect thereto
- NEITHER WILEY NOR ITS LICENSORS MAKES ANY WARRANTY OR REPRESENTATION OF ANY KIND TO YOU OR ANY THIRD PARTY, EXPRESS, IMPLIED OR STATUTORY, WITH RESPECT TO THE MATERIALS OR THE ACCURACY OF ANY INFORMATION CONTAINED IN THE MATERIALS, INCLUDING, WITHOUT LIMITATION, ANY IMPLIED WARRANTY OF MERCHANTABILITY, ACCURACY, SATISFACTORY QUALITY, FITNESS FOR A PARTICULAR PURPOSE, USABILITY, INTEGRATION OR NON-INFRINGEMENT AND ALL SUCH WARRANTIES ARE HEREBY EXCLUDED BY WILEY AND ITS LICENSORS AND WAIVED BY YOU.
- WILEY shall have the right to terminate this Agreement immediately upon breach of this Agreement by you.
- You shall indemnify, defend and hold harmless WILEY, its Licensors and their respective directors, officers, agents and employees, from and against any actual or threatened claims, demands, causes of action or proceedings arising from any breach of this Agreement by you.
- IN NO EVENT SHALL WILEY OR ITS LICENSORS BE LIABLE TO YOU OR ANY OTHER PARTY OR ANY OTHER PERSON OR ENTITY FOR ANY SPECIAL, CONSEQUENTIAL, INCIDENTAL, INDIRECT, EXEMPLARY OR PUNITIVE DAMAGES, HOWEVER CAUSED, ARISING OUT OF OR IN CONNECTION WITH THE DOWNLOADING, PROVISIONING, VIEWING OR USE OF THE MATERIALS REGARDLESS OF THE FORM OF ACTION, WHETHER FOR BREACH OF CONTRACT, BREACH OF WARRANTY, TORT, NEGLIGENCE, INFRINGEMENT OR OTHERWISE (INCLUDING, WITHOUT LIMITATION, DAMAGES BASED ON LOSS OF PROFITS, DATA, FILES, USE, BUSINESS OPPORTUNITY OR CLAIMS OF THIRD PARTIES), AND WHETHER OR NOT THE PARTY HAS BEEN ADVISED OF THE POSSIBILITY OF SUCH DAMAGES. THIS LIMITATION SHALL APPLY NOTWITHSTANDING ANY FAILURE OF ESSENTIAL PURPOSE OF ANY LIMITED REMEDY PROVIDED HEREIN.
- Should any provision of this Agreement be held by a court of competent jurisdiction to be illegal, invalid, or unenforceable, that provision shall be deemed amended to achieve as nearly as possible the same economic effect as the original provision, and the legality, validity and enforceability of the remaining provisions of this Agreement shall not be affected or impaired thereby.

<https://s100.copyright.com/MyAccount/web/jsp/viewprintablelicensefrommyorders.jsp?ref=3b75577b-609e-455b-b708-bfcfd2df3563&email=>

2/4

Appendix A.2: Reprint Permission: Chapter 1, Figure 1-5

11/1/2018

RightsLink - Your Account

JOHN WILEY AND SONS LICENSE TERMS AND CONDITIONS

Nov 01, 2018

This Agreement between Patricia Johnson ("You") and John Wiley and Sons ("John Wiley and Sons") consists of your license details and the terms and conditions provided by John Wiley and Sons and Copyright Clearance Center.

License Number	4457730697952
License date	Oct 28, 2018
Licensed Content Publisher	John Wiley and Sons
Licensed Content Publication	Magnetic Resonance in Medicine
Licensed Content Title	Optimizing spherical navigator echoes for three-dimensional rigid-body motion detection
Licensed Content Author	Daniel W. Petrie, Andreu F. Costa, Atsushi Takahashi, et al
Licensed Content Date	Apr 20, 2005
Licensed Content Volume	53
Licensed Content Issue	5
Licensed Content Pages	8
Type of Use	Dissertation/Thesis
Requestor type	University/Academic
Format	Print and electronic
Portion	Figure/table
Number of figures/tables	1
Original Wiley figure/table number(s)	Figure 2
Will you be translating?	No
Title of your thesis / dissertation	Retrospective motion correction in magnetic resonance imaging of the brain
Expected completion date	Dec 2018
Expected size (number of pages)	140
Requestor Location	Patricia Johnson

11/1/2018

RightsLink - Your Account

- The materials you have requested permission to reproduce or reuse (the "Wiley Materials") are protected by copyright.
- You are hereby granted a personal, non-exclusive, non-sub licensable (on a stand-alone basis), non-transferable, worldwide, limited license to reproduce the Wiley Materials for the purpose specified in the licensing process. This license, **and any CONTENT (PDF or image file) purchased as part of your order**, is for a one-time use only and limited to any maximum distribution number specified in the license. The first instance of republication or reuse granted by this license must be completed within two years of the date of the grant of this license (although copies prepared before the end date may be distributed thereafter). The Wiley Materials shall not be used in any other manner or for any other purpose, beyond what is granted in the license. Permission is granted subject to an appropriate acknowledgement given to the author, title of the material/book/journal and the publisher. You shall also duplicate the copyright notice that appears in the Wiley publication in your use of the Wiley Material. Permission is also granted on the understanding that nowhere in the text is a previously published source acknowledged for all or part of this Wiley Material. Any third party content is expressly excluded from this permission.
- With respect to the Wiley Materials, all rights are reserved. Except as expressly granted by the terms of the license, no part of the Wiley Materials may be copied, modified, adapted (except for minor reformatting required by the new Publication), translated, reproduced, transferred or distributed, in any form or by any means, and no derivative works may be made based on the Wiley Materials without the prior permission of the respective copyright owner. **For STM Signatory Publishers clearing permission under the terms of the STM Permissions Guidelines only, the terms of the license are extended to include subsequent editions and for editions in other languages, provided such editions are for the work as a whole in situ and does not involve the separate exploitation of the permitted figures or extracts**, You may not alter, remove or suppress in any manner any copyright, trademark or other notices displayed by the Wiley Materials. You may not license, rent, sell, loan, lease, pledge, offer as security, transfer or assign the Wiley Materials on a stand-alone basis, or any of the rights granted to you hereunder to any other person.
- The Wiley Materials and all of the intellectual property rights therein shall at all times remain the exclusive property of John Wiley & Sons Inc, the Wiley Companies, or their respective licensors, and your interest therein is only that of having possession of and the right to reproduce the Wiley Materials pursuant to Section 2 herein during the continuance of this Agreement. You agree that you own no right, title or interest in or to the Wiley Materials or any of the intellectual property rights therein. You shall have no rights hereunder other than the license as provided for above in Section 2. No right, license or interest to any trademark, trade name, service mark or other branding ("Marks") of WILEY or its licensors is granted hereunder, and you agree that you shall not assert any such right, license or interest with respect thereto
- NEITHER WILEY NOR ITS LICENSORS MAKES ANY WARRANTY OR REPRESENTATION OF ANY KIND TO YOU OR ANY THIRD PARTY, EXPRESS, IMPLIED OR STATUTORY, WITH RESPECT TO THE MATERIALS OR THE ACCURACY OF ANY INFORMATION CONTAINED IN THE MATERIALS, INCLUDING, WITHOUT LIMITATION, ANY IMPLIED WARRANTY OF MERCHANTABILITY, ACCURACY, SATISFACTORY QUALITY, FITNESS FOR A PARTICULAR PURPOSE, USABILITY, INTEGRATION OR NON-INFRINGEMENT AND ALL SUCH WARRANTIES ARE HEREBY EXCLUDED BY WILEY AND ITS LICENSORS AND WAIVED BY YOU.
- WILEY shall have the right to terminate this Agreement immediately upon breach of this Agreement by you.
- You shall indemnify, defend and hold harmless WILEY, its Licensors and their respective directors, officers, agents and employees, from and against any actual or threatened claims, demands, causes of action or proceedings arising from any breach of this Agreement by you.
- IN NO EVENT SHALL WILEY OR ITS LICENSORS BE LIABLE TO YOU OR ANY OTHER PARTY OR ANY OTHER PERSON OR ENTITY FOR ANY SPECIAL, CONSEQUENTIAL, INCIDENTAL, INDIRECT, EXEMPLARY OR PUNITIVE DAMAGES, HOWEVER CAUSED, ARISING OUT OF OR IN CONNECTION WITH THE DOWNLOADING, PROVISIONING, VIEWING OR USE OF THE MATERIALS REGARDLESS OF THE FORM OF ACTION, WHETHER FOR BREACH OF CONTRACT, BREACH OF WARRANTY, TORT, NEGLIGENCE, INFRINGEMENT OR OTHERWISE (INCLUDING, WITHOUT LIMITATION, DAMAGES BASED ON LOSS OF PROFITS, DATA, FILES, USE, BUSINESS OPPORTUNITY OR CLAIMS OF THIRD PARTIES), AND WHETHER OR NOT THE PARTY HAS BEEN ADVISED OF THE POSSIBILITY OF SUCH DAMAGES. THIS LIMITATION SHALL APPLY NOTWITHSTANDING ANY FAILURE OF ESSENTIAL PURPOSE OF ANY LIMITED REMEDY PROVIDED HEREIN.
- Should any provision of this Agreement be held by a court of competent jurisdiction to be illegal, invalid, or unenforceable, that provision shall be deemed amended to achieve as nearly as possible the same economic effect as the original provision, and the legality, validity and enforceability of the remaining provisions of this Agreement shall not be affected or impaired thereby.

<https://s100.copyright.com/MyAccount/web/jsp/viewprintablelicensefrommyorders.jsp?ref=330d4c0c-4ef2-422b-a6ff-20c4237b514c&email=>

2/4

Appendix A.3: Reprint Permission: Chapter 1, Figure 1-9

11/1/2018

RightsLink - Your Account

SPRINGER NATURE LICENSE TERMS AND CONDITIONS

Nov 01, 2018

This Agreement between Patricia Johnson ("You") and Springer Nature ("Springer Nature") consists of your license details and the terms and conditions provided by Springer Nature and Copyright Clearance Center.

License Number	4457750776263
License date	Oct 28, 2018
Licensed Content Publisher	Springer Nature
Licensed Content Publication	Springer eBook
Licensed Content Title	Whole Image Synthesis Using a Deep Encoder-Decoder Network
Licensed Content Author	Vasileios Sevetlidis, Mario Valerio Giuffrida, Sotirios A. Tsaftaris
Licensed Content Date	Jan 1, 2016
Type of Use	Thesis/Dissertation
Requestor type	non-commercial (non-profit)
Format	print and electronic
Portion	figures/tables/illustrations
Number of figures/tables/illustrations	1
Will you be translating?	no
Circulation/distribution	<501
Author of this Springer Nature content	no
Title	Retrospective motion correction in magnetic resonance imaging of the brain
Institution name	n/a
Expected presentation date	Dec 2018
Portions	Figure 1
Requestor Location	Patricia Johnson

11/1/2018

RightsLink - Your Account

1. The Licensor warrants that it has, to the best of its knowledge, the rights to license reuse of this material. However, you should ensure that the material you are requesting is original to the Licensor and does not carry the copyright of another entity (as credited in the published version).

If the credit line on any part of the material you have requested indicates that it was reprinted or adapted with permission from another source, then you should also seek permission from that source to reuse the material.

2. Where **print only** permission has been granted for a fee, separate permission must be obtained for any additional electronic re-use.
3. Permission granted **free of charge** for material in print is also usually granted for any electronic version of that work, provided that the material is incidental to your work as a whole and that the electronic version is essentially equivalent to, or substitutes for, the print version.
4. A licence for 'post on a website' is valid for 12 months from the licence date. This licence does not cover use of full text articles on websites.
5. Where '**reuse in a dissertation/thesis**' has been selected the following terms apply: Print rights of the final author's accepted manuscript (for clarity, NOT the published version) for up to 100 copies, electronic rights for use only on a personal website or institutional repository as defined by the Sherpa guideline (www.sherpa.ac.uk/romeo/).
6. Permission granted for books and journals is granted for the lifetime of the first edition and does not apply to second and subsequent editions (except where the first edition permission was granted free of charge or for signatories to the STM Permissions Guidelines <http://www.stm-assoc.org/copyright-legal-affairs/permissions/permissions-guidelines/>), and does not apply for editions in other languages unless additional translation rights have been granted separately in the licence.
7. Rights for additional components such as custom editions and derivatives require additional permission and may be subject to an additional fee. Please apply to Journalpermissions@springernature.com/bookpermissions@springernature.com for these rights.
8. The Licensor's permission must be acknowledged next to the licensed material in print. In electronic form, this acknowledgement must be visible at the same time as the figures/tables/illustrations or abstract, and must be hyperlinked to the journal/book's homepage. Our required acknowledgement format is in the Appendix below.
9. Use of the material for incidental promotional use, minor editing privileges (this does not include cropping, adapting, omitting material or any other changes that affect the meaning, intention or moral rights of the author) and copies for the disabled are permitted under this licence.
10. Minor adaptations of single figures (changes of format, colour and style) do not require the Licensor's approval. However, the adaptation should be credited as shown in Appendix below.

Appendix — Acknowledgements:

For Journal Content:

Reprinted by permission from [the Licensor]: [Journal Publisher (e.g. Nature/Springer/Palgrave)] [JOURNAL NAME]
[REFERENCE CITATION (Article name, Author(s) Name), [COPYRIGHT] (year of publication)]

For Advance Online Publication papers:

Reprinted by permission from [the Licensor]: [Journal Publisher (e.g. Nature/Springer/Palgrave)] [JOURNAL NAME]
[REFERENCE CITATION (Article name, Author(s) Name), [COPYRIGHT] (year of publication), advance online publication,
day month year (doi: 10.1038/sj.[JOURNAL ACRONYM].)]

For Adaptations/Translations:

Adapted/Translated by permission from [the Licensor]: [Journal Publisher (e.g. Nature/Springer/Palgrave)] [JOURNAL NAME]
[REFERENCE CITATION (Article name, Author(s) Name), [COPYRIGHT] (year of publication)]

Note: For any republication from the British Journal of Cancer, the following credit line style applies:

Reprinted/adapted/translated by permission from [the Licensor]: on behalf of Cancer Research UK: : [Journal Publisher
(e.g. Nature/Springer/Palgrave)] [JOURNAL NAME] [REFERENCE CITATION (Article name, Author(s) Name),

<https://s100.copyright.com/MyAccount/web/jsp/viewprintablelicensefrommyorders.jsp?ref=728da2e9-1c2a-4353-969a-f9a066f5f0bd&email=>

2/3

Appendix A.4: Reprint Permission: Chapter 2

10/28/2018

Rightslink® by Copyright Clearance Center



RightsLink®

Home

Account
Info

Help



Title: Retrospective 3D motion correction using spherical navigator echoes

Author: Patricia M. Johnson, Junmin Liu, Trevor Wade, Mohammad Ali Tavallaei, Maria Drangova

Publication: Magnetic Resonance Imaging

Publisher: Elsevier

Date: November 2016

© 2016 Published by Elsevier Inc.

Logged in as:
Patricia Johnson

[LOGOUT](#)

Please note that, as the author of this Elsevier article, you retain the right to include it in a thesis or dissertation, provided it is not published commercially. Permission is not required, but please ensure that you reference the journal as the original source. For more information on this and on your other retained rights, please visit: <https://www.elsevier.com/about/our-business/policies/copyright#Author-rights>

[BACK](#)
[CLOSE WINDOW](#)

Copyright © 2018 [Copyright Clearance Center, Inc.](#) All Rights Reserved. [Privacy statement](#). [Terms and Conditions](#).
Comments? We would like to hear from you. E-mail us at customercare@copyright.com

Appendix B

Ethics approval notices



Date: 29 June 2018

To: Terry Thompson

Project ID: 6319

Study Title: Improving Magnetic Resonance Imaging Hardware and Software at 1.5 and 3 Tesla

Application Type: Continuing Ethics Review (CER) Form

Review Type: Delegated

REB Meeting Date: 17/Jul/2018

Date Approval Issued: 29/Jun/2018

REB Approval Expiry Date: 28/Jul/2019

Dear Terry Thompson,

The Western University Research Ethics Board has reviewed the application. This study, including all currently approved documents, has been re-approved until the expiry date noted above.

REB members involved in the research project do not participate in the review, discussion or decision.

Western University REB operates in compliance with, and is constituted in accordance with, the requirements of the TriCouncil Policy Statement: Ethical Conduct for Research Involving Humans (TCPS 2); the International Conference on Harmonisation Good Clinical Practice Consolidated Guideline (ICH GCP); Part C, Division 5 of the Food and Drug Regulations; Part 4 of the Natural Health Products Regulations; Part 3 of the Medical Devices Regulations and the provisions of the Ontario Personal Health Information Protection Act (PHIPA 2004) and its applicable regulations. The REB is registered with the U.S. Department of Health & Human Services under the IRB registration number IRB 00000940.

Please do not hesitate to contact us if you have any questions.

Sincerely,

Daniel Wyzynski, Research Ethics Coordinator, on behalf of Dr. Joseph Gilbert, HSREB Chair

Note: This correspondence includes an electronic signature (validation and approval via an online system that is compliant with all regulations).



**Western
Research**

Research Ethics

**Western University Health Science Research Ethics Board
HSREB Annual Continuing Ethics Approval Notice**

Date: February 02, 2017

Principal Investigator: Dr. Charlie McKenzie

Department & Institution: Unknown, Western University

Review Type: Delegated

HSREB File Number: 2137

Study Title: 3.0T MRI Software and RF Hardware Development 10854E

HSREB Renewal Due Date & HSREB Expiry Date:

Renewal Due -2018/01/31

Expiry Date -2018/02/18

The Western University Health Science Research Ethics Board (HSREB) has reviewed the Continuing Ethics Review (CER) Form and is re-issuing approval for the above noted study.

The Western University HSREB operates in compliance with the Tri-Council Policy Statement Ethical Conduct for Research Involving Humans (TCPS2), the International Conference on Harmonization of Technical Requirements for Registration of Pharmaceuticals for Human Use Guideline for Good Clinical Practice (ICH E6 R1), the Ontario Freedom of Information and Protection of Privacy Act (FIPPA, 1990), the Ontario Personal Health Information Protection Act (PHIPA, 2004), Part 4 of the Natural Health Product Regulations, Health Canada Medical Device Regulations and Part C, Division 5, of the Food and Drug Regulations of Health Canada.

Members of the HSREB who are named as Investigators in research studies do not participate in discussions related to, nor vote on such studies when they are presented to the REB.

The HSREB is registered with the U.S. Department of Health & Human Services under the IRB registration number IRB 00000940.

Appendix C- Curriculum Vitae

Patricia M. Johnson

Correspondence Language: English
Country of Citizenship: Canadian

Degrees

2013/9 – present	PhD., Department of Medical Biophysics University of Western Ontario Degree Status: In progress Supervisor: Dr. Maria Drangova
2008/9 – 2013-5	B.Sc. (Honors), Physics Co-op, Biophysics Specialization, University of Waterloo Degree Status: Completed

Awards

2018/07	SciNet – International HPC summer school (~ \$2000) High performance computing summer school –Czech Republic
2018/03	Oral presentation award: 2 nd place (\$300) Imaging Network of Ontario annual meeting
2016/5-2017/4	Ontario Graduate Scholarship (\$15,000) Department of Medical Biophysics, University of Western Ontario
2016/3	Magna cum Laude –top abstract award Imaging Network of Ontario annual meeting
2016/2	International Society of Magnetic Resonance in Medicine Trainee stipend. Travel award for ISMRM 2016 annual meeting (\$450)
2015/9-2018/8	Dean's MSc to PhD transfer scholarship (\$5000/year) Schulich Faculty of Medicine and Dentistry
2015/5-2018/4	Schulich graduate scholarship (\$2000/year) Schulich Faculty of Medicine and Dentistry
2015/9	A.C. Groom Seminar of the Year Award (\$1000) Department of Medical Biophysics, University of Western Ontario

2014/6	International Society of Magnetic Resonance in Medicine Trainee stipend. Travel award for Motion Correction in MRI workshop
2013/09-present	Western Graduate Research Scholarship (\$4,500/year) University of Western Ontario

Employment

2013/9 – present	Graduate Research Assistant Medical Biophysics, University of Western Ontario, Robarts Research Institute Full-time
2016/1 – 2018/4	Graduate Teaching Assistant University of Western Ontario Course Title: Selected Topics in Medical Sciences Course Level: 4 th year undergraduate
2013/1 – 2013/5	Undergraduate Research Assistant Nanoscale Biophysics Lab, University of Waterloo Part-time
2012/5 – 2012/9	Medical Physics Research Assistant University of Calgary, Tom Baker Cancer Centre. Full-time

Affiliations

2013/9 – present	Graduate Student, Robarts Research Institute, University of Western Ontario
------------------	--

Journal Articles

1. **P.M Johnson**, M Drangova, Three-dimensional rigid-body motion correction in MRI using a conditional generative adversarial network. Submitted to Magnetic Resonance in Medicine
2. **P.M Johnson** R Taylor T Whelan, J.D Thiessen, U Anazodo, M Drangova, Rigid-body motion correction in hybrid PET/MRI using spherical navigator echoes. Submitted to Physics in Medicine and Biology.
3. **P. M Johnson**, J. Liu, T. Wade, M.A Tavallaei, and M. Drangova, Retrospective 3D Motion Correction in MRI Using Spherical Navigator Echoes. Magn Reson Imaging. 34(9):1274-82 (2016)
4. M.A Tavallaei, **P.M Johnson**, J. Liu and M. Drangova, Design and Evaluation of an MRI-Compatible Linear Motion Stage. Med. Phys. 43, 62 (2016)

5. M. Balderson, D. Brown, **P. M Johnson**, C. Kirkby, Under conditions of large geometric miss, tumor control probability can be higher for static gantry IMRT compared to VMAT for prostate cancer. Med Dosim. 41(2):180-5. (2016)

Refereed abstracts and proceedings

1. (June 2018) **P.M Johnson**, M Drangova. Motion correction in MRI using a deep neural network. ISMRM 2018, Paris, France
2. (June 2018) **P.M Johnson**, R Taylor, T Whelan, M Drangova, Motion correction of PET images using Spherical Navigator echoes (SNAVs) on a hybrid PET-MR scanner. ISMRM 2018, Paris, France
3. (March 2018) **P.M Johnson**, R Taylor, T Whelan, U Anazodo, M Drangova, Spherical navigator echoes (SNAVs) correct for motion of PET and MR images on a hybrid PET/MR scanner. Imaging Network of Ontario, Toronto, Canada
4. (Mar 2018) **P.M Johnson**, M Drangova. Motion-corrected MRI reconstruction using deep learning. ISMRM workshop: Machine Learning in MRI, Pacific Grove, California
5. (Oct 2017) **P.M Johnson**, R Taylor, T Whelan, J Thiessen, M Drangova, Spherical navigator echoes (SNAVs) correct for motion of PET images on a hybrid PET-MR scanner. ISMRM Workshop: Simultaneous PET-MRI, Chicago, USA
6. (Sep 2017) **P.M Johnson**, LJ Gula, AC Skanes, R Acedillo, M Drangova, J Inoue, Big data analytics in a large AF patient cohort: correlates to hospitalizations and ED visits. Canadian Arrhythmia Network Annual Meeting.
7. (Apr 2017) **P.M Johnson**, J. Liu, M. Drangova. Simultaneous motion and B0 correction using FID-SNAVs. International Society of Magnetic Resonance in Medicine Annual Scientific Meeting
8. (Mar 2017) **P.M Johnson**, J. Liu, T. Wade and M. Drangova. Retrospective motion and B0 correction using FID-SNAVs. Imaging Network of Ontario Symposium, London, Ontario.
9. (May 2016) **P.M Johnson**, J. Liu, T. Wade and M. Drangova. Three-dimensional retrospective motion correction using spherical navigator echoes. International Society of Magnetic Resonance in Medicine Annual Scientific Meeting
10. (Mar 2016) **P.M Johnson**, J. Liu, T. Wade and M. Drangova. Retrospective motion correction of brain MRI using spherical navigator echoes. Imaging Network of Ontario Symposium, Toronto, Ontario.
11. (Jun 2015) **P.M Johnson**, J. Liu, T. Wade and M. Drangova. Six-degree of Freedom Retrospective Motion Correction using Spherical Navigator Echoes. International Society of Magnetic Resonance in Medicine Annual Scientific Meeting
12. (Oct 2014) M.A Tavallaei, J. Liu, **P.M Johnson**, and M. Drangova. MRI

Compatible Linear Motion Stage. Interventional MRI Symposium, Leipzig, Germany

13. (Jul 2014). **P.M Johnson**, J. Liu, M.A Tavallaei, and M. Drangova. Toward Practical Motion Correction in MRI Using Spherical Navigator Echoes. ISMRM Workshop: Motion Correction in MRI, Tromso, Norway
14. (Mar 2014.) **P.M Johnson**, J. Liu and M. Drangova. Toward Practical Spherical Navigator Echo Registration for 3D Motion Detection in MRI. Imaging Network of Ontario Symposium, Toronto, Ontario.